2014

Material Synthesis and Fabrication Method Development for Intermediate Temperature Solid Oxide Fuel Cells

Hanping Ding
University of South Carolina - Columbia

Recommended Citation

Ding, H.(2014). *Material Synthesis and Fabrication Method Development for Intermediate Temperature Solid Oxide Fuel Cells.* (Doctoral dissertation). Retrieved from http://scholarcommons.sc.edu/etd/2622

MATERIAL SYNTHESIS AND FABRICATION METHOD DEVELOPMENT FOR INTERMEDIATE TEMPERATURE SOLID OXIDE FUEL CELLS

by

Hanping Ding

Bachelor of Materials Science
Jilin University, 2006

Master of Materials Science
University of Science and Technology of China, 2009

Submitted in Partial Fulfillment of the Requirements

For the Degree of Doctor of Philosophy in

Mechanical Engineering

College of Engineering and Computing

University of South Carolina

2014

Accepted by:

Xingjian Xue, Major Professor

Ken Reifsnider, Committee Member

Chen Li, Committee Member

Xiaodong Zhou, Committee Member

Lacy Ford, Vice Provost and Dean of Graduate Studies

DEDICATION

To my loved wife Xiaofang and son Ivan.

ACKNOWLEDGEMENTS

I am truly grateful to many people who have helped me for my doctoral study at the University of South Carolina. First of all, I would like to thank my advisor Professor Xingjian (Chris) Xue for his guidance and support on my study. He has always been a passionate and inspiring scientist in mathematical modelling and materials science. I also thank Professor Ken Reifsnider, Professor Chen Li and Professor Xiao-Dong Zhou for reviewing my dissertation and working as defense committee members.

This dissertation would not be possible without financial supports from the U.S. National Science Foundation (CMMI-1100085), Department of Energy, Basic Energy Sciences (DE-SC0001061) and the University of South Carolina, Office of Research and Graduate Education.

I want to appreciate many colleagues at the University of South Carolina. Lee helped me to set up the original laboratory and solve any problems in experimental works. I also thank all staffs at the Electron Microscopy Center for supporting me with their facilities and expertise. It has been a great pleasure to spend last five years with friends at Department of Mechanical Engineering: Junxiang Shi, Yuanyuan Xie, Litao Yan, Junjie Ge, Xinfang Jin, Tingfang Tian, Shuming Fang, Rassel Raihan, Rabbi Fazle and other students and post doctors in Horizon Building. I should also appreciate the administrative staff Ravi Lalitha for helping me considerably.

My deepest gratitude goes to my wife Xiaofang and son Ivan for standing behind and loving me silently.

ABSTRACT

Solid oxide fuel cells (SOFCs) are operated in high temperature conditions (750-1000 ^{o}C). The high operating temperature in turn may lead to very complicated material degradation issues, significantly increasing the cost and reducing the durability of SOFC material systems. In order to widen material selections, reduce cost, and improve durability of SOFCs, there is an increasing interest to develop intermediate temperature SOFCs (500-750 ^{o}C). However, lowering operating temperature will cause substantial increases of ohmic resistance of electrolyte and polarization resistance of electrodes. This dissertation is aimed at developing high-performance intermediate-temperature SOFCs through materials synthesis and innovative fabrication method development. It has been recognized that the cathode electrode is a key component limiting the SOFC performance particularly at lower temperature conditions. A series of layered perovskite oxides are synthesized and characterized as intermediate temperature cathode materials. To obtain both high performance and chemical as well as mechanical stability, the substitution of Fe in B site of perovskite cathode materials is comprehensively investigated to explore the effects of Fe doping on the crystal structure, thermal and electrical properties, as well as electrochemical performance. The electrochemical performance of synthesized perovskite cathode materials is systematically evaluated using button cells, where both doped ceria and barium based oxides are employed as electrolyte materials.

The conductivity of cathode materials is usually on the order of 102 S/cm, which

is low in conducting electrons between the oxygen reduction reaction (ORR) sites and external circuit. To compensate for the low conductivities of cathode oxides, the current collector is typically employed in SOFCs. Consequently the electrons needed by ORR can be transported from the external circuit to the reaction sites with minimum ohmic loss. Despite of the significant importance, the designs of current collectors do not receive too much attention in open literatures. Usually the platinum ink or platinum paste is simply painted on the cathode surface. After sintering, the organic substance is burn out while the platinum is attached to the cathode surface. A novel platinum nanowire network is developed as a highly efficient current collector for SOFCs. Results indicate that the polarization resistance of $PrBaCo_2O_{5+\delta}$ (PBCO) cathode with nanowire current collector was reduced by 44% at 650 ^oC (from 0.18 Ω cm^2 to 0.1 Ω cm^2). The peak power density of the button cells was improved at different degrees of 31.8%– 59.6% under temperatures 650 ^oC–550 ^oC for typical cathode materials of PBCO, $La_{0.6}Sr_{0.4}Co_{0.2}Fe_{0.8}O_{3-\delta}$ (LSCF), and $Ba_{0.5}Sr_{0.5}Co_{0.8}Fe_{0.2}O_{3-\delta}$ (BSCF). The nanowire network did not show obvious changes after long term test (400 h).

The SOFCs with metal oxide as anodes are usually electrolyte-supported design. This design requires relatively thick electrolyte of 300~500 μm to support the entire cell, leading to significant ohmic resistance. Accordingly, high temperatures (800-900 ^oC) are needed to reduce the ohmic loss for high power outputs. Anode-supported designs may effectively reduce the ohmic loss with thin electrolyte membrane while lowering the operating temperatures. However, the anode-supported designs with metal oxides as anode materials are difficult to fabricate. In general, high sintering temperature is needed to co-fire the anode substrate/electrolyte assembly to densify the thin electrolyte, which in turn may induce the densification of the porous anode substrate, resulting in anode porosity loss. A novel fabrication method is developed to fabricate ceramic anode supported SOFC based on the perovksite anode oxide of $La_{0.75}Sr_{0.25}Cr_{0.5}Mn_{0.5}O_{3-\delta}$ (LSCM). The cell exhibits the power density of 596 mW cm^{-2} and 381 mW cm^{-2} at 700 ^{o}C with the humidified hydrogen and methane as the fuel respectively, the highest performance up to date for the cells with metal oxide anodes at this temperature.

Table of Contents

LIST OF TABLES

LIST OF FIGURES

LIST OF SYMBOLS

E	Equilibrium potential
E^0	Standard potential
P	Partial pressure of gas
T	Absolute temperature
F	Faraday’s constant
R	Universal gas constant
η_{ohm}	Ohmic polarization
η_{act}	Activation polarization
η_{conc}	Concentration polarization
t	Goldschmidt tolerance factor
σ	Conductivity
C	Pre-exponential factor
k	Boltzmann constant
E_a	Activation energy
a_p	Lattice parameter of the primitive cubic perovskite
D^*	Oxygen self-diffusion coefficient
k^*	Surface oxygen exchange coefficient
P_{max}	Peak power density
R_p	Interfacial polarization resistance
R_t	Total cell resistance

R_o	Ohmic resistance

LIST OF ABBREVIATIONS

MCFC	Molten Carbonate Fuel Cell
AFC	Alkaline Fuel Cell
PEMFC	Polymer Electrolyte Membrane Fuel Cell
SOFC	Solid Oxide Fuel Cell
IT	Intermediate Temperature
TPB	Three Phase Boundary
TEC	Thermal Expansion Coefficient
XRD	X-Ray Diffraction
TGA	Thermo-Gravimetric Analysis
DSC	Differential Scanning Calorimetry
ECR	Electrical Conductivity Relaxation
IEDP	Isotope Exchange and Depth Profiling
PLD	Pulsed Laser Deposition
GNP	Glycine-Nitrate Process
SEM	Scanning Electron Microscopy
EIS	Electrochemical Impedance Spectra
OCV	Open Circuit Voltage
PCMFC	Proton Conducting Membrane Fuel Cell
EDTA	Ethylene Diamine Tetraacetic Acid
MIEC	Mixed Ionic and Electronic Conductor

YSZ	$Y_{0.08}Zr_{0.92}O_{2-\delta}$
LSM	$La_{0.8}Sr_{0.2}MnO_{3-\delta}$
LSCF	$La_{x}Sr_{1-x}Co_{y}Fe_{1-y}O_{3-\delta}$
BSCF	$Ba_{0.5}Sr_{0.5}Co_{0.8}Fe_{0.2}O_{3-\delta}$
SSC	$Sm_{0.5}Sr_{0.5}CoO_{3-\delta}$
LSGM	$La_{0.8}Sr_{0.2}Ga_{0.83}Mg_{0.17}O_{3}$
GDC	$Gd_{0.1}Ce_{0.9}O_{1.95}$
PBCO	$PrBaCo_{2}O_{5+\delta}$
PBCF	$PrBa(Co_{1-x}Fe_{x})_{2}O_{5+\delta}$
GBCF	$GdBaCoFeO_{5+\delta}$
GBFO	$GdBaFe_{2}O_{5+\delta}$
BZCY7	$BaZr_{0.1}Ce_{0.7}Y_{0.2}O_{3-\delta}$
LSCM	$La_{0.75}Sr_{0.25}Cr_{0.5}Mn_{0.5}O_{3-\delta}$

CHAPTER 1

INTRODUCTION

Massive energy shortage and environmental issues are the two challenges facing the entire world. These challenges significantly drive the innovations and breakthroughs of energy technologies, such as hydroenergy, wind energy, solar energy, and geothermal energy, as well as fuel cells. In the past few decades, fuel cell technologies have achieved significant progress, including materials, fabrication methods, and system designs. Fuel cell is an energy conversion device that converts chemical energy of fuels into electricity directly with high efficiencies and minimal or zero emissions.[1] Theoretically the efficiency of fuel cells may reach 80%, much higher than that of Carnot cycle in conventional combustion engines.[2,3] According to electrolyte materials, the fuel cells can be categorized into: molten carbonate fuel cell (MCFC),[4] alkaline fuel cell (AFC),[5] phosphoric acid fuel cell (PAFC),[6] polymer electrolyte membrane fuel cell (PEMFC)[7] and solid oxide fuel cell (SOFC).[8,9] Among these five types of fuel cells, SOFCs have the advantages of: (1) high energy conversion efficiency and energy density;[10] (2) fuel flexibility including hydrogen, natural gas and other hydrocarbon fuels;[11] (3) high operating temperatures that do not need precious metal as catalyst for electrodes;[12] (4) all solid state structure effectively preventing the issues like corrosion of liquid electrolyte; (5) high heat energy byproduct; (6) wide applications in stationary power generations and small-scale portal power sources in computer, mobile cell or vehicle auxiliary power supply. Therefore, SOFCs have attracted much attention in renewable and clean energy community.

1 Review of SOFC Fundamental

1.1.1 Working Principal of SOFC

The working principal of an SOFC is schematically illustrated in Figure 1.1.[13]

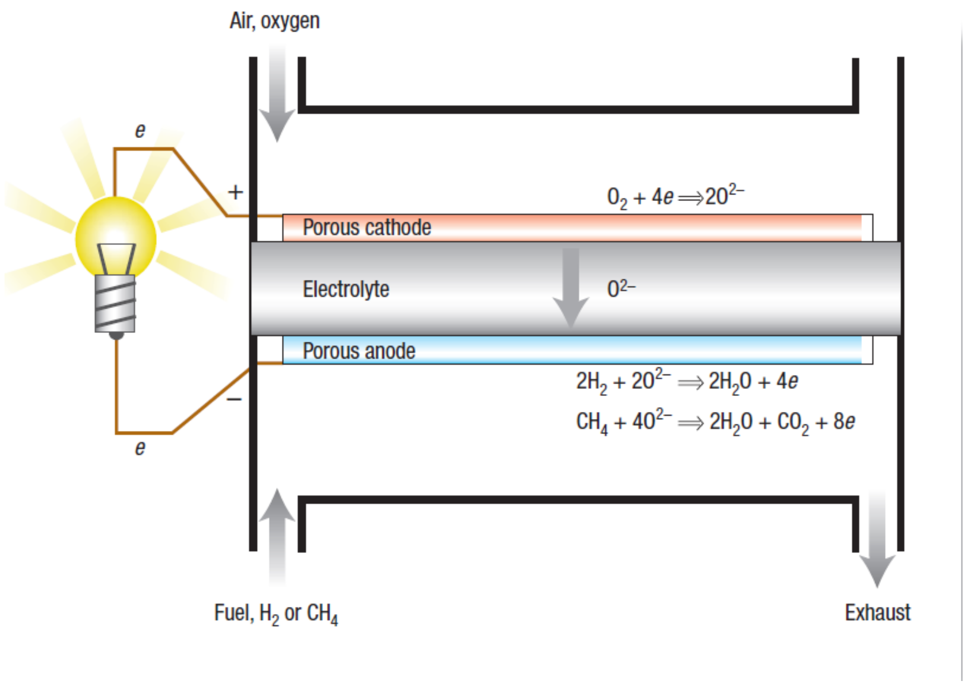

Figure 1. 1 Working principle of a SOFC. (reprinted from Boukamp *et al. Nature Mater.* **2003**, *2*, 294-296)[13]

A dense solid oxide electrolyte is sandwiched by porous electrode on either side, forming positive-electrode-electrolyte-negative-electrode (PEN) structure assembly.[14] The oxygen flows into the cathode channel and further diffuses into porous cathode, where oxygen molecules combines with electrons from external circuit, forming oxygen ions. The generated oxygen ions then transport to the anode side through the electrolyte. At the anode side, the fuels (e.g., hydrogen) flow into the anode channel and further diffuse into porous anode, where the hydrogen molecules combine with oxygen ions from cathode side, generating water molecules and electrons. The electrons then transport to the external circuit, producing useful electricity. The corresponding electrochemical reactions can be described as following:

$$\text{Cathode: } \frac{1}{2}O_2 + 2e^- \rightarrow O^{2-} \quad (1)$$

$$\text{Anode: } H_2 + O^{2-} \rightarrow H_2O + 2e^- \quad (2)$$

$$\text{Overall reaction: } H_2 + \frac{1}{2}O_2 \rightarrow H_2O\ (g) \quad (3)$$

1.1.2 POLARIZATION OF SOFC

The open-circuit voltage and power density are typical electrochemical parameters used to evaluate the performance of an SOFC. The equilibrium potential of an ideal fuel cell can be expressed using Nernst equation, relating the change in the voltage of electrons to the change in the Gibbs free energy of the reaction.[15,16]

$$E = E^0 + \frac{RT}{2F}\ln\left(\frac{P_{H_2}P_{O_2}^{1/2}}{P_{H_2O}}\right) \quad (4)$$

where E^0 is the standard potential, E is the equilibrium potential, P the partial pressure of reactant gases, T the temperature, F the Faraday's constant, R the universal gas constant.

Practically the operating voltage of fuel cells is always lower than the ideal Nernst equilibrium potential due to the internal losses induced by imperfections in component materials, microstructure and also the design of the fuel cell configuration. These internal losses include ohmic resistances from electrolyte and electrodes, activation polarization resistance due to the kinetics of electrochemical reactions at gas/electrode interface in porous electrodes, and the concentration polarization resistance due to the fuel/gas diffusion in porous electrodes. The cell voltage can be determined by [17]:

$$V = E_0 - \eta_{ohm} - \eta_{act} - \eta_{conc} \tag{5}$$

where E_0 is the ideal Nernst potential calculated from thermodynamic principles. η_{ohm} represents overall ohmic resistance. η_{act} and η_{conc} account for the activation and concentration polarization resistance respectively. These three internal losses are all highly dependent on the current density of fuel cells.

A typical current-voltage polarization curve of an SOFC is shown in Figure 1.2. The curve can be divided into three zones: the activation polarization region, ohmic region, and concentration polarization region. The activation polarization region is in low current conditions and reflects the catalytic activity of electrodes. The activation polarization can be expressed using the Butler-Volmer equation[17]:

$$i = i_0 \left\{ exp\left(\beta \frac{2F\eta_{act}}{RT}\right) - exp\left(-(1-\beta)\frac{2F\eta_{act}}{RT}\right) \right\} \tag{6}$$

The ohmic polarization region dominates intermediate current zone. The voltage-current behavior shows nearly a linear relationship and the slope represents the overall internal resistance of fuel cell.

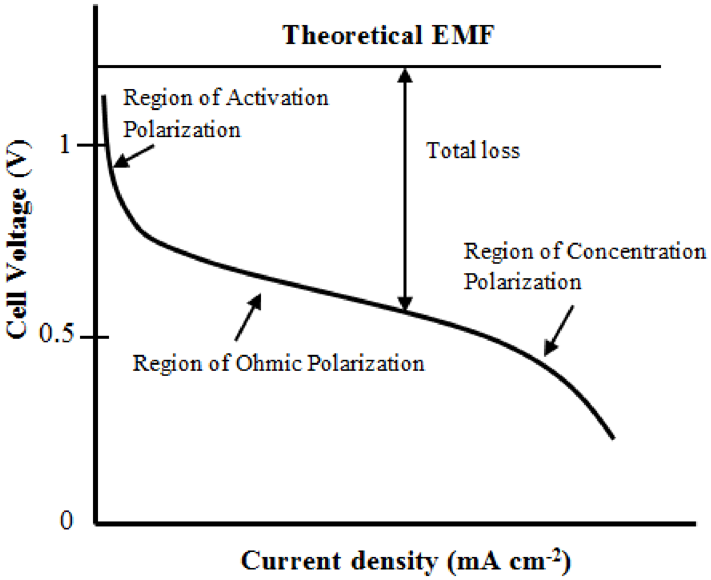

Figure 1. 2 A typical current-voltage polarization curve of an operating SOFC.

Usually the ionic conductivity of the electrolyte is much smaller than electronic conductivity of cathode and anode electrodes, the ohmic resistance is mainly attributed to the electrolyte. For example, the ionic resistivity of $Y_{0.08}Zr_{0.92}O_{2-\delta}$ (YSZ) at 700 ^{o}C is 100 $\Omega\cdot$cm;[18] however, the electronic resistivity of $La_{0.8}Sr_{0.2}MnO_{3-\delta}$ (LSM) and Ni-YSZ are 10^{-2} and 10^{-4} order of magnitude, respectively.[19,20] Therefore, the employment of thin film electrolyte facilitates to decrease ohmic resistance.[21,22]

In the region of concentration polarization, the cell current is relatively high. Accordingly the fuel/gas consumed by electrochemical reactions is high. When the fuel/gas transports from channel/electrode interface to the reaction sites in the porous electrodes, diffusion resistance in porous electrodes leads to concentration gradient of products and reactants across the electrode. As a result, concentration polarization resistance occurs in the electrodes.[23] Therefore, the microstructure of electrode such as porosity, pore size and distribution can be optimized to minimize the concentration polarization resistance.[24]

1.1.3 LOWERING OPERATING TEMPERATURE

Traditional SOFCs are operated at high temperatures between 800 and 1000 ^{o}C. The high operating temperature could potentially lead to complex material degradation problems, significantly hindering the commercialization of SOFC technology.[25,26] Therefore, there is an increasing interest in developing intermediate temperature (500-800 ^{o}C) solid oxide fuel cells (IT-SOFCs).[27,28] However, lowering the operating temperature may cause substantial increases of ohmic resistance and polarization losses, particularly for electrolyte and cathode components.[29,30] To obtain comparable or better performance of SOFCs at reduced temperatures, innovations of materials and cell designs are needed. For electrolyte component, we have two ways to reduce the ohmic resistance at reduced temperatures, e.g., developing new electrolyte materials with high ionic conductivity or reducing the thickness of electrolyte.[31] For cathode component, we may either develop materials with high conductivity and catalytic activity for electrochemical reactions or optimize microstructures of porous electrode. The cathode materials may include mixed ionic electronic conductors that have high conductivity and catalytic activity.[32] The optimization of electrode microstructure can be obtained by developing functionally graded electrodes or modifying cathode surface through infiltration techniques.[33]

In the past decade, significant efforts have been put into the development of high performance cathode materials.[34,35] This includes a class of simple perovskite-type MIECs such as doped $La_xSr_{1-x}Co_yFe_{1-y}O_{3-\delta}$ (LSCF),[36] $Ba_{0.5}Sr_{0.5}Co_{0.8}Fe_{0.2}O_{3-\delta}$ (BSCF)[27,37] and $Sm_{0.5}Sr_{0.5}CoO_{3-\delta}$ (SSC)[38,39] for SOFCs. Recently layered perovskites have received much attention. Kim and Tarancón et al.[40,41] investigated a series of $LnBaCo_2O_{5+\delta}$ (Ln=Pr, Nd, Sm, Gd, Eu, and Y) oxides as potential cathode materials. High oxygen surface exchange rate and self-diffusion coefficient are observed from experimental.[42,43] These compounds can be theoretically described with the stacking sequence of …|BaO|CoO_2|LnO_x|CoO_2…. When $x < 1$, the ordered A-cations localizing oxygen vacancies appear within the rare earth layers.[44,45] This characteristic has a great potential to improve cathode performance. When a simple cubic perovskite with randomly occupied A-sites transfers into a layered crystal structure with ordered lanthanide and alkali-earth layers, it reduces the strength of oxygen binding and provides disorder-free channels for ionic migration.

1.2 CATHODE MATERIAL FOR SOFC

1.2.1 BASIC REQUIREMENTS AS A CATHODE

The three key components of SOFCs are anode, electrolyte and cathode. Due to the larger contribution of activation polarization losses from cathode materials particularly at lower operation temperatures, much attention has been focused on the development of cathode electrode, including new material development and optimization of cathode microstructure and surface. In the cathode electrode, oxygen reduction reactions take place, where the electrons from external circuit are combined with oxygen atoms, generating oxygen ions. The specific reaction process occurring on the cathode surface is very complicated and may include oxygen diffusion, adsorption and desorption, electrochemical reaction. The basic requirements for cathode materials are as follows:[46]

(1) Stability: In oxidizing atmosphere, the cathodes should have adequate chemical stability;

(2) Conductivity: Cathode should possess high electrical conductivity to lower the ohmic resistance and high oxygen ionic conductivity in the cathode bulk and interface.

(3) Catalytic activity: the cathode material should have high catalytic activity for surface electrochemical reactions;

(4) Chemical and thermal compatibilities: Cathodes should have good chemical compatibility with electrolyte, interconnect and seal materials without reaction and element diffusion. The cathode should have good thermal compatibility with other

components to prevent mechanical failure.

1.2.2 TRIPLE-PHASE BOUNDARIES AT CATHODES

On the surface of the cathode, oxygen reduction reaction can be described as followings:

$$\frac{1}{2}O_2(gas) + 2e^-(cathode) \rightarrow O^{2-}(electrolyte) \qquad (7)$$

Electron-conducting perovskite-type materials such as doped $LaMnO_3$, $LaCoO_3$, $SmCoO_3$, or $LaFeO_3$ are extensively investigated as SOFC cathodes.[47] For these materials three possible paths have been suggested for the cathodic reaction as shown in Fig.1.3.

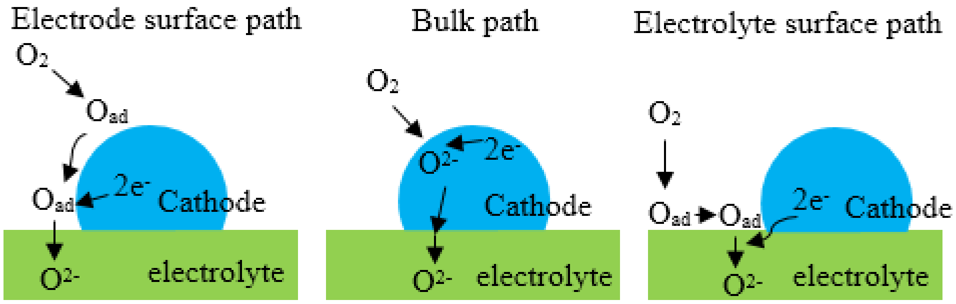

Figure 1. 3 Sketches of the three reaction paths of the oxygen reduction and incorporation reaction and some possible rate-determining steps. Modifications of the paths (e.g., adsorption of a molecular rather than an atomic species or diffusion along the cathode/electrolyte interface) and a combination of electrode and electrolyte surface paths (adsorption on cathode and surface diffusion onto the electrolyte surface) are also possible. (Reprinted from J. Fleig, *Annu. Rev. Mater. Res.* **2003**, *33*, 361)[34]

(1) In the case of cathode surface path, the process includes gas oxygen diffusion through porous cathode layer, adsorption of oxygen molecules on the cathode surface and diffusion of oxygen species after ionized by electrons along the surface toward the TPB where electrolyte, cathode and gas phase meet together, followed by complete ionization and the oxygen ions transferring into conducting electrolyte.[48,49] The incorporation of

oxygen ions into the electrolyte can be also extended to other area by diffusion along the cathode surface or interface.

(2) In the case of cathode bulk path, the process consists of gaseous oxygen diffusion in porous electrode, adsorption on the cathode surface, dissociation and ionization. The oxygen ions are incorporated into the cathode bulk, which generally occurs in MIECs,[50] and subsequent transport into the electrolyte. Perovksite materials usually possess this feature due to the flexibility of crystal structure, leading to the broad stoichiometric or nonstoichiometric change of chemical composition.[51-55]

(3) In the case of electrolyte surface path, the oxygen adsorption and ionization occur on the electrolyte surface. Due to the fact that most electrolytes have very low electronic conductivity particularly for YSZ and $La_{0.8}Sr_{0.2}Ga_{0.83}Mg_{0.17}O_3$ (LSGM), this reaction would be restricted to the nearby of the TPBs.

From above discussions of possible paths for oxygen diffusion and reaction, one can see that the cathode material play a critical role on determining the ORR rate. Fast adsorption and desorption are favorable for ORR process. The electronic and ionic conductivities are essentially required to enable the ionization and diffusion of oxygen species. All these are closely related to the crystal structure of cathode materials.

1.2.3 SIMPLE PEROVSKITE (ABO_3) OXIDE AS CATHODE

Perovskite oxides have the general formula of ABO_3 and have been widely studied as cathode materials for SOFCs. Both A-site and B-site doping strategies have been employed to tailor electrical and mechanical properties.[56] This tunability of perovskite structure offers wide flexibility to improve the properties of materials,[4] such as catalytic activity, electronic and ionic conductivity, chemical stability and thermal property. Many properties of the perovskites are mainly determined by the B-site cations while being tuned by A-site cations. The ideal perovskite is a cubic structure (Fig.1.4) with the larger A-site cations located at the corners of the cube, the B-site cations at the body center, and the oxygen ions at the centers of the cubic faces. The lower valence A cations (such as, La, Sr, Ca, Sm and Ba, etc.) at the interstitial site surrounded by four octahedron are larger and coordinated to twelve oxygen anions while the B cations (such as, Ti, Cr, Ni, Fe, Co, V, Zn, Ce, Y and Zr, etc.) at the center of octahedron occupy the much smaller space and are coordinated to six oxygen anions.[57]

According to the condition of charge neutrality, electron/hole defects or oxygen vacancies at the oxygen lattice sites would be introduced when A or B cations are partially or fully substituted with other cations. As a result, the defect concentration and electrical properties are changed.

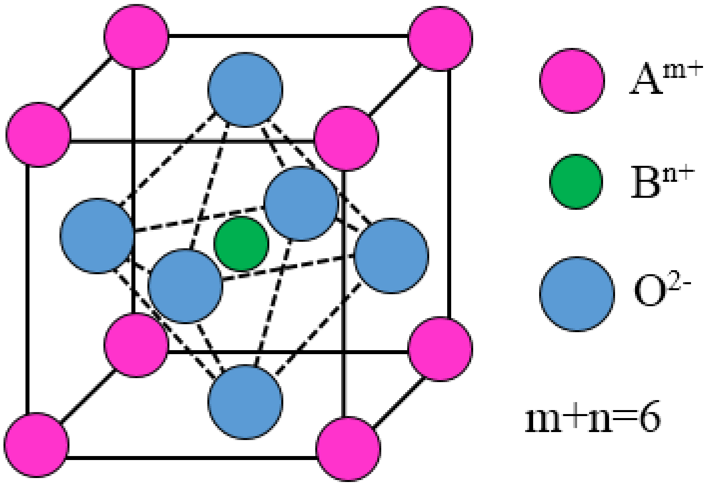

Figure 1. 4 Unit cell of the ABO_3 perovskite structure. The A cations occupy the larger spaces in the 12-fold oxygen coordinated holes while the B cations occupy the much smaller octahedral holes (sixfold coordination).

Perovskite generally involves structural distortion such as the tilting of the octahedron and displacement of cations. While the distortion may achieve certain electrical property, it also leads to the issue of structural stability. The degree of structural distortion can be determined using the Goldschmidt tolerance factor (t) calculated with the equation as follows:[58]

$$t = \frac{r_A + r_O}{\sqrt{2}(r_B + r_O)} \tag{8}$$

Stable perovskite structures are predicted in the range of $0.77 \leq t \leq 1$.[59] Designating t close to unity can obtain higher symmetry and smaller volume of unit cell. On the contrary, the substitution of smaller A or bigger B cations results in a decrease in the tolerance factor, in the meantime, it also leads to a cation displacement and the tilting of corner sharing BO_6 octahedron to lower structure symmetry with reduced B-O-B bond angles. For most of the perovskite oxides used as cathodes for SOFCs, the A-site cation is a mixture of rare and alkaline earths such as La and Sr, Ca or Ba, while the B-site cation is a reducible transition metal such as Mn, Fe, Co, or Ni. Accordingly, the catalytic mechanism for ORR is usually provided by B-site redox cations and the electrical properties are tailored by element replacement at A-site. The radius of the A-site cation and particularly its variance are important factors controlling perovskite properties.[60] Based on the Shannon's ionic radii of the different coordinate numbers, a two-dimensional structural field map can be constructed to predict the ranges of the existence of perovskite oxides for a new elemental combination.[61] For well-known perovskite oxides such as $La_{1-x}Sr_xCo_{0.5}Fe_{0.5}O_{3-\delta}$ and $Ba_{1-x}Sr_xCo_{0.5}Fe_{0.5}O_{3-\delta}$, the replacement of smaller La^{3+} by Sr^{2+} ions increases the tolerance, indicating the increase of material stability while improving the conductivity. As a comparison, when the larger Ba^{2+} is replaced by Sr^{2+}, the decrease of tolerance factor would limit this substitution.

Nevertheless, due to the large A-site cations, the tolerance factors of $Ba_{1-x}Sr_xCo_{0.5}Fe_{0.5}O_{3-\delta}$ are very high.

1.2.4 ORIGIN AND MECHANISMS OF ELECTRICAL PROPERTIES

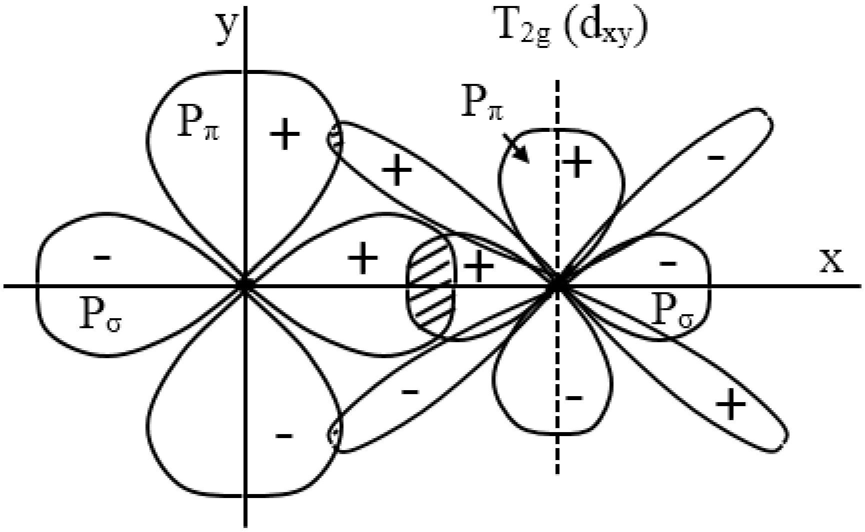

Figure 1. 5 Covalent bonds between the p_π-orbitals of oxygen ion and t_{2g} (*d*) orbitals of B-cation. (Reprinted from J. Richter *et al. Monatsh Chem.* ***2009****, 140,* 985)[56]

Due to electro-neutrality condition, divalent acceptor substitution for the trivalent A-site cation can introduce effective negative charge compensated either by the formation of oxygen vacancies (ionic compensation) or an increase in valence of the B-site cations (electronic compensation).[62] In order to achieve electronic conductivity, it is required that the heterovalent cations at the B-site show at least two stable oxidation states compatible with the octahedral geometry, such as $Mn^{3+/4+}$, $Fe^{3+/4+}$, $Co^{2+/3+/4+}$, $Ni^{2+/3+}$, etc. According to the crystal field theory, the overlap between B_{3d} and O_{2p} atomic orbitals (Fig.1.5) can provide a path for electron hopping between neighboring B cations while the valence of transition metals is changed along BO_6 octahedron network. Meanwhile, B-O bond distance and B-O-B bond angle determine the degree of overlap of successive B_{3d} orbitals with the same O_{2p} orbital, or the degree of orbital overlap of each B_{3d}-O_{2p}-B_{3d} triplet. Theoretically, the width of conduction band and conductivity are proportional to the bond order and B_{3d}-O_{2p}-B_{3d} bond angle.[56,63]

The Arrhenius plot ln(σT) versus 1/T is usually used to analyze the nature of electronic conduction by this equation:[64,65]

$$\sigma = \left({}^{C}\!/_{T^{s}} \right) exp(-E_a/kT) \tag{9}$$

where σ is the electrical conductivity, C the pre-exponential factor, T the absolute temperature, k the Boltzmann constant, and E_a the activation energy or energy barrier for polaron migration. Activation energy can be obtained through linear curve fitting of experimental data. The exponent s equals either 1 or 3/2 for adiabatic limes or non-adiabatic small polaron, respectively.[66] The linear behavior indicates the electronic conductivity is due to the small polaron-hopping mechanism.[67]

To improve the catalytic rate for ORR, a significant amount of ionic conductivity (O^{2-}) is needed. The conduction of oxygen ions occurs via the vacancy/ion exchange mechanism, in which the oxygen ions exchange their positions with adjacent vacancies through diffusive jump process. The ionic conductivity is dependent on the concentration of available vacancies generated by temperature-dependent intrinsic defects and extrinsic defects related to impurities and substitution level.[68,69] Further ionic conductivity is also dependent on structural factors. Higher structural symmetry in perovskites with tolerance factors close to 1 is favorable for better ionic conductivity.[70] Theoretically, the movement of oxygen ions is achieved by jumping from one vacancy site to the adjacent one along the octahedron edge, in which the ions have to pass through a “saddle point” built by two A-site cations and one B-site cation as shown in Fig.1.6.

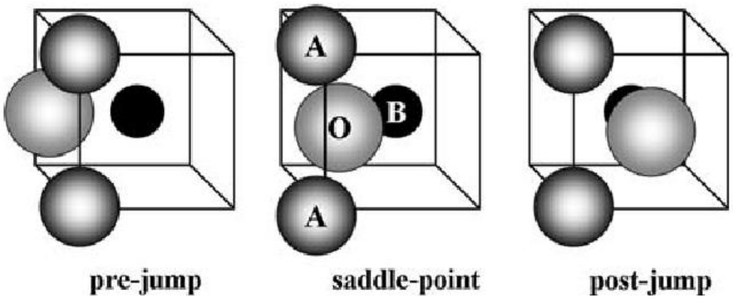

Figure 1. 6 Saddle point: two A-site cations and one B-site cation build a gap which is described by the critical radius; the cations show significant outward relaxation to permit the migration of the oxygen ion. (Reprinted from M. S. Islam *et al. J Solid State Chem.* **1996**, *124*, 230)[70]

A term of critical radius (r_{cr}) is used to describe the maximum size of interstitial space for mobile ions to pass through, and can be calculated by Eq. 10:

$$r_{cr} = \frac{a_0\left(\frac{3}{4}a_0 - \sqrt{2}r_B\right) + r_B^2 - r_A^2}{2(r_A - r_B) + \sqrt{2}a_0} \tag{10}$$

$$a_0 \approx V_{cell}^{\frac{1}{3}} = 2.37r_B + 2.47 - 2(t^{-1} - 1) \tag{11}$$

where r_A and r_B are the radius of the A and B ions, respectively, and a_0 corresponds to the pseudo cubic lattice parameter ($V^{1/3}$) derived from Eq. 11.[71,72] In principal, larger critical radii can be achieved by increasing r_B and/or reducing r_A. However, the radius of the oxygen ion is 1.4 Å in the sixfold coordination.[70] When oxygen ions proceed diffusive jump, the temporarily adopted threefold coordination might decrease the radius of oxygen ions; however, it would still be too large (1.36 Å) to pass through the saddle-point. In order to promote the migration of oxygen ions, thermal vibration of cations is supposed to increase the critical radius and thus the possibility to jump through. On the other hand, the deficiency of A site cations might enhance the amplitude of their thermal vibrations due to the presence of more available vacancies.[73]

1.2.5 Previous Studies on Perovskites as Cathode Materials

Here the state-of-the-art perovskite cathode materials are simply reviewed.

(1) Lanthanum strontium manganite ($La_{1-x}Sr_xMnO_{3-\delta}$, LSM)

Currently, LSM perovskite is the most important cathode material for SOFCs operated in the temperature range of 700-900 °C due to its high electrical conductivity, catalytic activity and compatibility with commonly used electrolyte of doped zirconia (YSZ) at operating conditions.[74,75] Mechanically, LSM has very similar thermal expansion coefficient to YSZ and thus can potentially prevent delamination failure at the cathode/electrolyte interface. LSM possesses only electronic conductivity, the ORR occurs only in the vicinity of the TPB, where the LSM, electrolyte material, and gas oxygen meet together. In order to enhance the electrical conductivity and catalytic activity of LSM, the oxygen non-stoichiometry is altered by partially substitution of strontium. This is generally formulated by $La_{1-x}Sr_xMnO_{3\pm\delta}$ ("+" denotes oxygen excess and "−" denotes oxygen deficiency). The ideal perovskite (Fig.1.7) crystalizes in a cubic close-packed lattice structure with larger La^{3+} and Sr^{2+} occupying the 12 coordinated A-sties and the transition metal ions of Mn^{3+} occupying octahedral B-sites.[76]

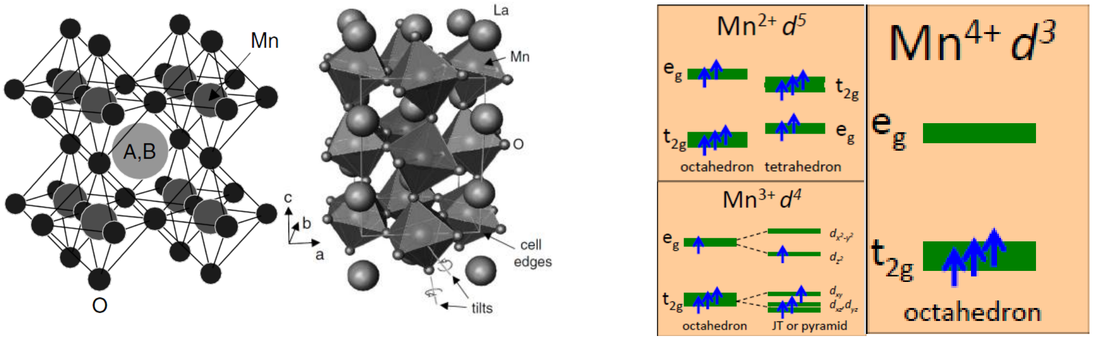

Figure 1. 7 Left: ideal cubic perovskite structure. Middle: lattice structure in the orthorhombic phase of $LaMnO_3$, where a pronounced tilting of the MnO_6 octahedra occurs. Right: the electron configuration in d orbitals at different crystal fields. (Reprinted from J. Geck *et al. New J. Phys.* **2001**, *143*, 379-389).[76]

The defect equation of Sr-doped LSM can be described as following:[77,78]

$$Mn_{Mn}^{\times} + SrO \xrightarrow{LaMnO_3} Sr_{La}' + Mn_{Mn}^{\cdot} + O_O^{\times} \qquad (12)$$

This reaction effectively increases the electron-hole concentration and improves the electrical conductivity for this n-type conductor while the lattice structure might experience the phase transition with long range John-Teller ordering.[79-81] The electronic conduction in LSM is p-type in the entire P_{O2} region with stable solid solution. The electronic conductivity of LSM increases approximately linearly with increasing Sr concentration of up to around 50 mol%.[82] It is assumed that a large disproportion of Mn^{3+} $(t_{2g}\uparrow)^3(e_g\uparrow)^1$ into Mn^{2+} (intermediate spin state $(t_{2g}\uparrow)^3(e_g\uparrow)^2$) and Mn^{4+} $(t_{2g}\uparrow)^3$ accounts for the high conductivity.

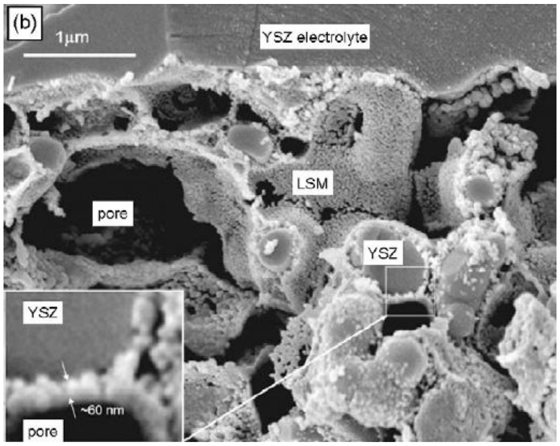

Figure 1. 8 Microstructure of LSM infiltrated cathodes prepared from mixed nitrate solution. (Reprinted from T. Z. Sholklapper *et al. Electrochemical and Solid State Letters* **2006**, *9*, A376)[37]

When LSM is infiltrated into YSZ backbone, a composite cathode is formed (as shown in Fig.1.8) and the corresponding single fuel cell may produce a maximum power density of 0.27 W cm^{-2} at 650 ^{o}C.[83] However, the development of LSM-based cathode for intermediate or low temperature SOFCs still has many challenges due to the high activation energy barrier for ORRs. Therefore, the further reduction of operating temperature requires better cathode materials with high electrical conductivity and catalytic activity as well as the stability and compatibility.

(2) $La_{1-x}Sr_xCo_{1-y}Fe_y$ (LSCF)

When an MIEC is used for cathode material, the ORR sites are extended from TPBs to the entire surface of porous cathode. LSCF is a widely used MIEC cathode material and exhibits very good electrical conductivity at intermediate temperatures.[84] Dusastre and Kilner optimized the LSCF/$Gd_{0.2}Ce_{0.8}O_{1.9}$ (GDC) composite cathodes and the electrode polarization resistance of 0.6 Ω cm^2 was obtained at 590 ℃ on the GDC electrolyte.[85] It was also demonstrated that the Sr doping may improve the conductivity of LSFC while the Fe doping can mitigate the thermal expansion coefficient (TEC). Most recently, the LSCF cathode decorated with $La_{0.4875}Ca_{0.0125}Ce_{0.5}O_{2-\delta}$ reached the polarization resistance of 0.076 Ω cm^2 at 750 ^{o}C; the peak power density of the corresponding Ni-YSZ based anode-supported cell was as high as ~1.25 W cm^{-2}.[86]

(3) $Ba_{0.5}Sr_{0.5}Co_{0.8}Fe_{0.2}O_{3-\delta}$ (BSCF)

The BSCF perovskite oxide with alkaline-earth metal of barium at A-site has been studied for oxygen permeation membrane. Haile and Shao originally developed BSCF as a cathode material for SOFCs, the corresponding peak power densities reached 1,010 and 402 mW cm^{-2} at 600 ℃ and 500 ℃, respectively.[27] The area-specific resistances were 0.055-0.071 and 0.51-0.61 Ω cm^2 at 600 and 500 ℃, respectively, considerably lower than those of other perovskite-type cathode materials. Nevertheless, BSCF material has relatively high TEC of 20×10^{-6} K^{-1} between 50 ℃ and 1000 ℃,[87] and shows certain chemical instability. The TEC mismatch with electrolyte could cause the cathode/electrolyte delamination failure. To mitigate the TEC mismatch, composite cathode can be employed, which is composed of mixture of BSCF cathode material and electrolyte material.

1.2.6 Double Perovskite

In recent years, several groups have been focused extensively on the crystal chemistry and magnetic properties of $LnBaCo_2O_{5+\delta}$ (Ln=Pr, Nd, Sm, Eu, Gd, Tb, Dy, Ho, and Y) layered perovskite oxides as shown in Fig.1.9. [42, 88-91] The anisotropy resulting from the presence of cation ordered crystal structure has been reported to be able to improve the oxygen transport compared to non-ordered oxides. This class of materials is a very suitable as cathode candidates for IT-SOFCs due to the rapid oxygen surface exchange and lower activation energy for oxygen diffusion.

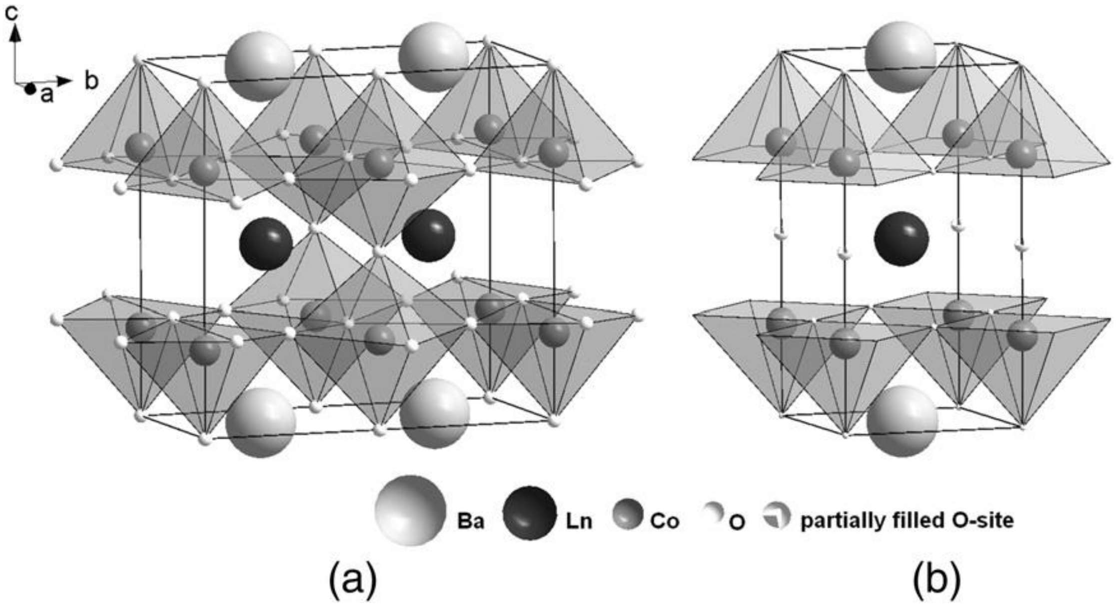

Figure 1. 9 Crystal structures of layered perovskites $LnBaCo_2O_{5+\delta}$ (Ln=lantanide). a) Orthorhombic and b) tetragonal phase. (Reprinted from L. Mogni *et al. Solid State Ionics* **2013**, *240*, 19)[52]

These compounds are related to the "112" type structure first reported for $YBaFeCuO_5$ and consist of double layers of square pyramidally coordinated cobalt cations.[92] The unit cell of $LnBaCo_2O_{5+\delta}$ has been reported to be orthorhombic structure with dimensions $a_p \times 2a_p \times 2a_p$ or $a_p \times a_p \times 2a_p$ (space group P_{mmm}), or tetragonal structure with dimensions $a_p \times a_p \times 2a_p$ ($P_{4/mmm}$),[93] where a_p refers to the lattice parameter of the primitive cubic perovskite. The symmetry and unit cell size highly depend on the oxygen content, the ionic size of Ln and temperature.

The first structural feature of layered perovskite is the ordering of lanthanide and Ba ions in alternating (001) layers.[94] The doubling of a_p along the c-axis is due to the location of Ln and Ba cations in alternative layers perpendicular to the c-axis; while the doubling of a_p along the b-axis results from the periodic locations of the oxygen vacancies along the a-direction.[42,95,96]

Another feature of layered perovskite is the ordered distribution of oxygen vacancies in the Ln layers. In order to tailor the transport properties, the oxygen non-stoichiometry can be changed by means of heat treatment. When the oxygen content is $5+\delta \approx 5.5$, the orthorhombic symmetry appears. In this case, a perfectly ordered sample would present 100% of the oxygen occupancy at Wyckoff position 1g, located at (0, 1/2, 1/2), and 0% at the 1c position of (0, 0, 1/2). The results with neutron diffraction technique reported by Frontera et al. found that the real oxygen occupancies are 91% and 12%, respectively, as shown in Table 1.1.[94] On the other hand, when the oxygen content is very different from 5.5, the crystal structure becomes tetragonal with the LnO layers partially empty.

Table 1. 1 Structural details of the prepared $PrBaCo_2O_{5+\delta}$ obtained by means of high resolution neutron powder diffraction. (Reprinted from C. Frontera, *Chem. Mater.* **2005**, *17*, 5439)[94]

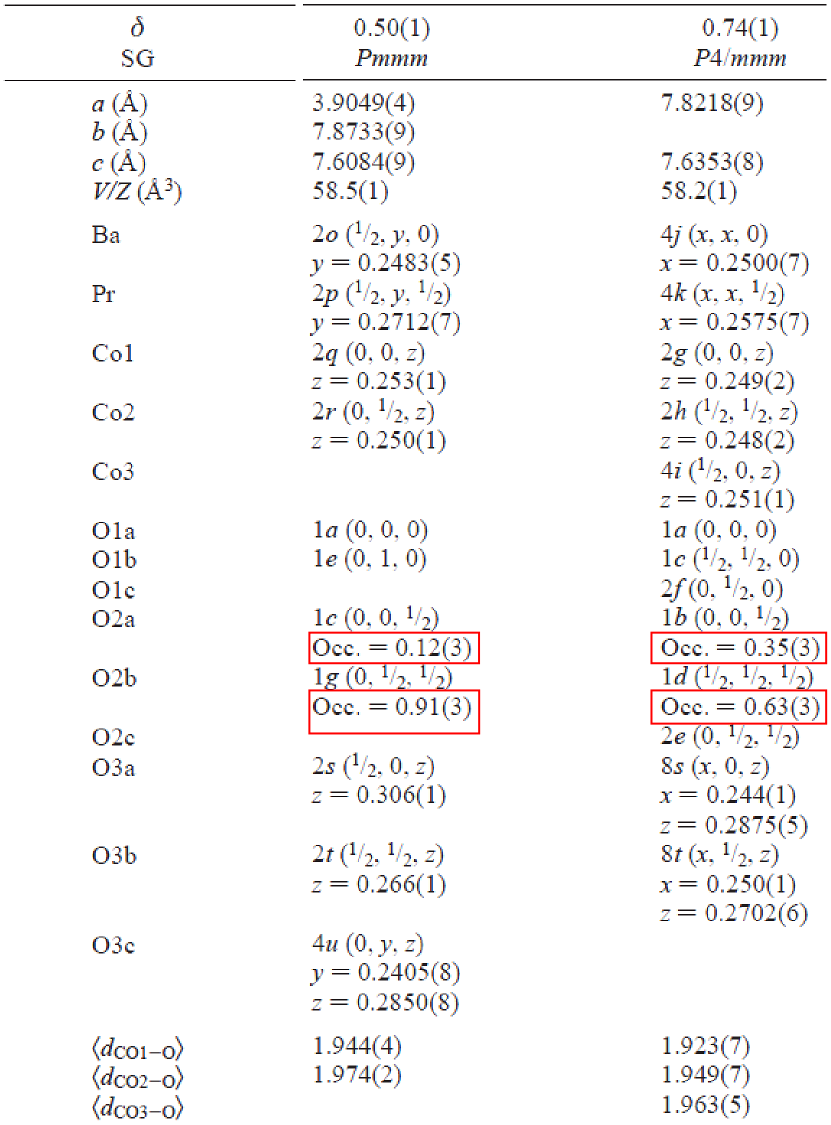

δ SG	0.50(1) *Pmmm*	0.74(1) *P4/mmm*
a (Å)	3.9049(4)	7.8218(9)
b (Å)	7.8733(9)	
c (Å)	7.6084(9)	7.6353(8)
V/Z (Å^3)	58.5(1)	58.2(1)
Ba	$2o$ ($^1/_2$, y, 0) $y = 0.2483(5)$	$4j$ (x, x, 0) $x = 0.2500(7)$
Pr	$2p$ ($^1/_2$, y, $^1/_2$) $y = 0.2712(7)$	$4k$ (x, x, $^1/_2$) $x = 0.2575(7)$
Co1	$2q$ (0, 0, z) $z = 0.253(1)$	$2g$ (0, 0, z) $z = 0.249(2)$
Co2	$2r$ (0, $^1/_2$, z) $z = 0.250(1)$	$2h$ ($^1/_2$, $^1/_2$, z) $z = 0.248(2)$
Co3		$4i$ ($^1/_2$, 0, z) $z = 0.251(1)$
O1a	$1a$ (0, 0, 0)	$1a$ (0, 0, 0)
O1b	$1e$ (0, 1, 0)	$1c$ ($^1/_2$, $^1/_2$, 0)
O1c		$2f$ (0, $^1/_2$, 0)
O2a	$1c$ (0, 0, $^1/_2$) Occ. = 0.12(3)	$1b$ (0, 0, $^1/_2$) Occ. = 0.35(3)
O2b	$1g$ (0, $^1/_2$, $^1/_2$) Occ. = 0.91(3)	$1d$ ($^1/_2$, $^1/_2$, $^1/_2$) Occ. = 0.63(3)
O2c		$2e$ (0, $^1/_2$, $^1/_2$)
O3a	$2s$ ($^1/_2$, 0, z) $z = 0.306(1)$	$8s$ (x, 0, z) $x = 0.244(1)$ $z = 0.2875(5)$
O3b	$2t$ ($^1/_2$, $^1/_2$, z) $z = 0.266(1)$	$8t$ (x, $^1/_2$, z) $x = 0.250(1)$ $z = 0.2702(6)$
O3c	$4u$ (0, y, z) $y = 0.2405(8)$ $z = 0.2850(8)$	
$\langle d_{Co1-O} \rangle$	1.944(4)	1.923(7)
$\langle d_{Co2-O} \rangle$	1.974(2)	1.949(7)
$\langle d_{Co3-O} \rangle$		1.963(5)

The structural feature of cationic ordering is found to facilitate the oxygen self-diffusion (D*) and also surface exchange, the two critical processes for oxygen reduction reaction of cathode materials. The cationic ordering reduces the oxygen bond strength and leads to disorder-free pathways for fast oxygen ion diffusion, which is responsible for the higher surface oxygen exchange rate (k*) observed in the ordered $GdBaMn_2O_{5+\delta}$, compared to the disordered $Gd_{0.5}Ba_{0.5}MnO_{3-x}$ with single perovskite phase.[93] The electronic conduction in $LnBaCo_2O_{5+\delta}$ occurs via hopping mechanism along the Co-O-Co bonds through a double exchange process similar to other simple perovskite ABO_3-type cathodes.[53]

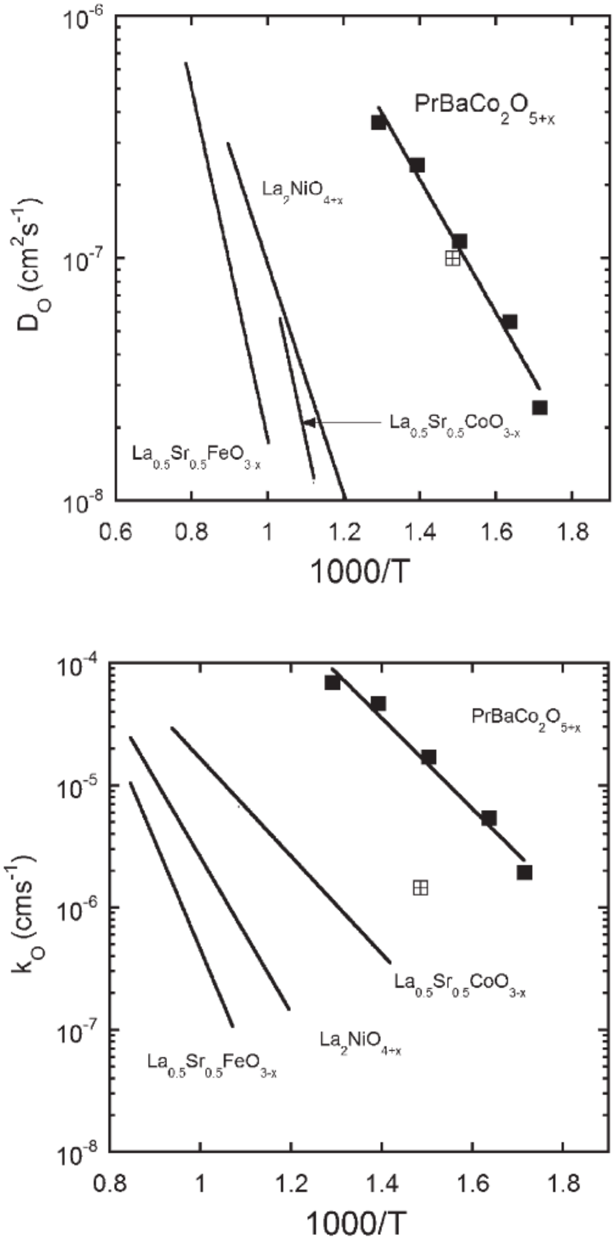

Figure 1. 10 Comparison of the values of (a) D_o and (b) k_o measured by ECR for ceramic samples. The filled squares are the ECR measurements and the crossed square is the IEDP result. (Reprinted from G. Kim *et al. J. Mater. Chem.* **2007**, *17*, 2500)[41]

Table 1. 2 Summary of oxygen self-diffusion and oxygen surface exchange data and overall conductivity for different SOFC cathode materials. (Reprinted from A. Tarancón *et al. J. Mater. Chem.* **2010**, *20*, 3799)[100]

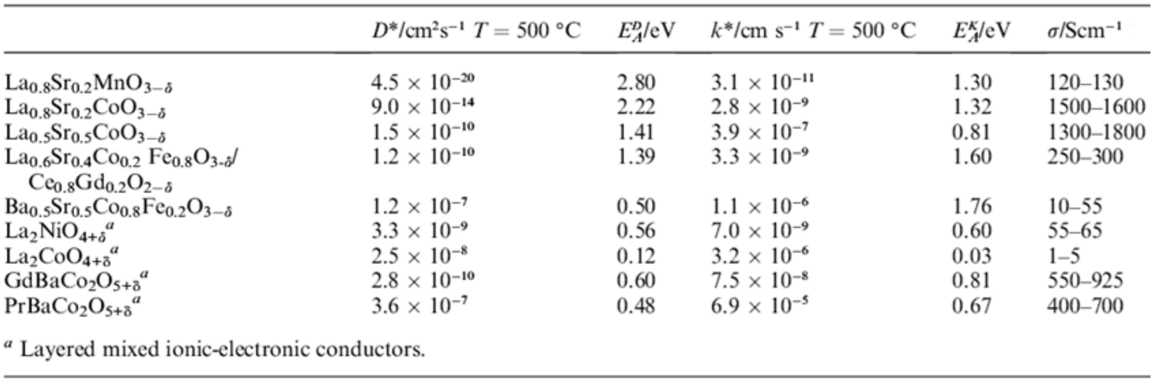

	D^*/cm²s⁻¹ $T = 500$ °C	E_A^D/eV	k^*/cm s⁻¹ $T = 500$ °C	E_A^K/eV	σ/Scm⁻¹
$La_{0.8}Sr_{0.2}MnO_{3-\delta}$	4.5×10^{-20}	2.80	3.1×10^{-11}	1.30	120–130
$La_{0.8}Sr_{0.2}CoO_{3-\delta}$	9.0×10^{-14}	2.22	2.8×10^{-9}	1.32	1500–1600
$La_{0.5}Sr_{0.5}CoO_{3-\delta}$	1.5×10^{-10}	1.41	3.9×10^{-7}	0.81	1300–1800
$La_{0.6}Sr_{0.4}Co_{0.2}Fe_{0.8}O_{3-\delta}$/ $Ce_{0.8}Gd_{0.2}O_{2-\delta}$	1.2×10^{-10}	1.39	3.3×10^{-9}	1.60	250–300
$Ba_{0.5}Sr_{0.5}Co_{0.8}Fe_{0.2}O_{3-\delta}$	1.2×10^{-7}	0.50	1.1×10^{-6}	1.76	10–55
$La_2NiO_{4+\delta}$[a]	3.3×10^{-9}	0.56	7.0×10^{-9}	0.60	55–65
$La_2CoO_{4+\delta}$[a]	2.5×10^{-8}	0.12	3.2×10^{-6}	0.03	1–5
$GdBaCo_2O_{5+\delta}$[a]	2.8×10^{-10}	0.60	7.5×10^{-8}	0.81	550–925
$PrBaCo_2O_{5+\delta}$[a]	3.6×10^{-7}	0.48	6.9×10^{-5}	0.67	400–700

[a] Layered mixed ionic-electronic conductors.

Kilner et al. have investigated $GdBaCo_2O_{5+x}$ for application as a cathode material for SOFCs.[97] An anode-supported fuel cell consisting of a 15 μm thick electrolyte of YSZ and a Ni-YSZ cermet as anode showed a maximum power density of 300 mW cm^{-2} at 700 °C in H_2. The cell performance has been further improved by using doped ceria as the electrolyte and composite cathode.[98] Later on, Kim et al. found (Fig.1.10) that $PrBaCo_2O_{5+\delta}$ (PBCO) has unusually rapid oxygen transport kinetics at low temperatures (300-500 °C) using electrical conductivity relaxation (ECR) and isotope exchange as well as depth profiling (IEDP) on both bulk ceramic materials and highly epitaxial PBCO thin films by pulsed laser deposition (PLD).[42,99]

According to above literature survey, it is clear that these double perovskite materials exhibit very high activity for oxygen activation and mobility. Table 1.2 summarizes the oxygen self-diffusion coefficient D* and oxygen surface exchange rate k* as well as the overall conductivity for different SOFC cathode materials. To obtain low polarization resistance, it requires from Table 1.2 that the value of k*D* is greater than 10^{-14} cm^{3}s^{-2} and k*/D*<100 cm^{-1}.

In the studies of Tarancón et al.[100] (GBCO) and Kim et al.[41] (PBCO), the above requirements for k* and D* can be satisfied even below 700 °C, indicating the suitability of layered perovskite as cathode materials at reduced temperatures. Both symmetrical cells[53,101] and single cells[43,97,102] have been used to evaluate the electrode performance of different layered perovskite oxides. An area specific resistance (ASR) value of 0.25 Ω cm^2 was obtained at 625 °C for GBCO/GDC. Zhang et al. ranking the cathode performance of different Ln^{3+} cations in $LnBaCo_2O_{5+\delta}$ oxides as follows: $Pr^{3+} > Gd^{3+} > Nd^{3+} > Sm^{3+} > La^{3+} > Y^{3+}$.[53] With a single cell configuration of PBCO/SDC/Ni-SDC, Zhu et al.[102] have recently reported remarkable cell performance of an ASR value close to the target value of 0.5 Ω cm^2 at 600 °C and a peak power density higher than 850 mW cm^{-2} at 650 °C.

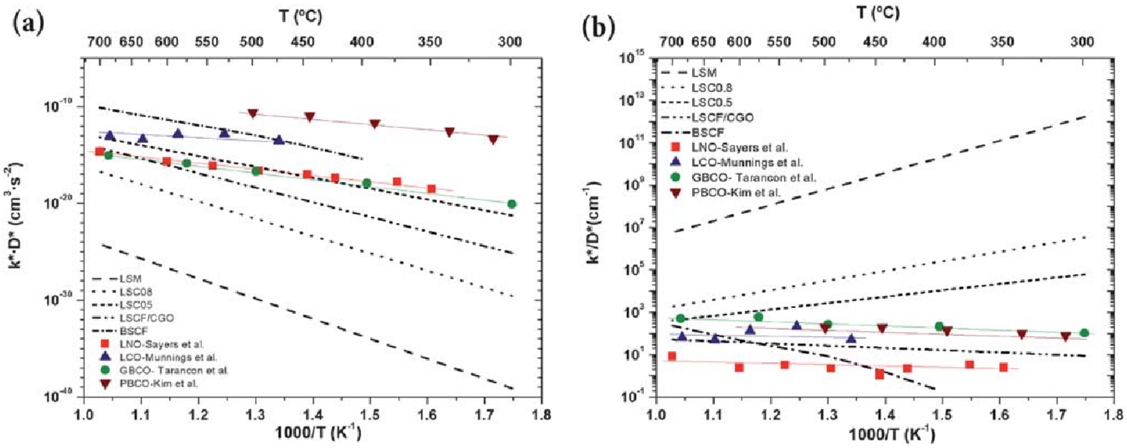

Figure 1. 11 Oxygen tracer diffusion and oxygen surface exchange for different layered oxide cathodes as a function of the temperature, (a) k*D*; (b) k*/D*. The materials used for comparison have been labeled as follows: LSM, $La_{0.8}Sr_{0.2}CoO_{3-\delta}$ (LSC08), $La_{0.5}Sr_{0.5}CoO_{3-\delta}$ (LSC05), $La_{0.6}Sr_{0.4}Co_{0.2}Fe_{0.8}O_{3-\delta}$ (LSCF)/GDC and BSCF. (Reprinted from A. Tarancón *et al. J. Mater. Chem.* **2010**, *20*, 3799)[100]

CHAPTER 2

CHARACTERIZATIONS OF LAYERED PEROVSKITE OXIDES AS CATHODE MATERIALS

To improve the cathode performance at intermediate temperatures, two approaches have been employed to either optimize porous microstructures of cathode electrodes or develop new cathode materials. The optimization of porous electrodes is generally implemented using infiltrating process, through which the nanosized particles are attached to the internal surface of porous electrode backbone.[103-105] As a consequence, the effective surface area for oxygen reduction reactions is dramatically increased. The ORR is strongly dependent on the cathode materials. The widely studied cathode material $La_{1-x}Sr_xMnO_3$ (LSM) demonstrates very good stability and can obtain sufficient electronic conductivity at relatively high temperatures.[78,106] However the conductivity of LSM would severely deteriorate at reduced temperatures. Further the LSM is electronic conductor; accordingly the ORR only occurs at triple phase boundary, where the LSM, the electrolyte material, and oxygen gas meet together. To increase the ORR sites while enhancing the conductivity of cathode materials at intermediate temperatures, MIECs have been extensively studied in recent years. Typical MIECs are ABO_3 type perovskite materials and have demonstrated very good performance as cathode materials at intermediate temperatures.[29,52,107,108]

Recently, a class of layered perovskite oxides, i.e., $LnBaCo_2O_{5+x}$ (Ln=Y, La, Pr Sm, Nd, Gd), has attracted the attention of SOFC community. Such perovskite oxides have ordered lanthanide and alkali-earth layers, which provide disorder-free channels for oxygen ion migration while reducing oxygen bonding strength. Therefore they have great potentials to improve the cathode performance at intermediate temperatures. Compared to a simple cubic perovskite, Taskin *et al*. showed that the oxygen-ion diffusivity in $GdBaB_2O_{5+x}$ (B = Mn, Co) increased by orders of magnitude.[109] Kim *et al.* reported that the oxygen ion diffusivity and surface exchange coefficient of PBCO may reach 10^{-5} cm^2 s^{-1} and 10^{-3} cm s^{-1} respectively.[110] The high performance of PBCO as cathode material in SOFCs has also been demonstrated.[111,112] Cobalt-containing cathode materials usually have excellent catalytic activity due to the varying multi-valence.[113] However, these cathode materials suffer from the problems of poor chemical stability in CO_2-containing atmosphere, high TECs and easy element evaporation.[29,114] The TEC difference between the cathode and electrolyte may lead to cathode/electrolyte interfacial stress, signifcantly affecting the reliability of SOFCs. If the cobalt element in these materials is partially substituted, it may potentially mitigate these issues while achieving sufficient catalytic activity for cathode materials.

In this research, we present a comprehensive characterization of Fe-substituted cobaltite $PrBa(Co_{1-x}Fe_x)_2O_{5+\delta}$ (PBCF) material system (x=0, 0.2, 0.4, 0.6 and 1.0). The effects of Fe doping on the crystal structure, chemical compatibility with the typical electrolyte material of samarium doped ceria, thermal expansion, sintering ability, and electrochemical performance as cathode materials, as well as reliability of cathode/electrolyte interface were systematically studied.

2.1 EXPERIMENTAL

$PrBa(Co_{1-x}Fe_x)_2O_{5+\delta}$ (x=0, 0.2, 0.4, 0.6 and 1.0) oxides were synthesized using a modified Pechini method. The precursor was prepared using analytical grade of Pr_6O_{11}, $Ba(CH_3COO)_2$, $Co(NO_3)_2{\bullet}6H_2O$ and $Fe(NO_3)_3{\bullet}9H_2O$. First Pr_6O_{11} was dissolved into nitric acid in a ceramic bowl. Stoichiometric amounts of nitrates $Co(NO_3)_2{\bullet}6H_2O$, $Fe(NO_3)_3{\bullet}9H_2O$, and $Ba(CH_3COO)_2$, were mixed into the ethylene diamine tetraacetic acid (EDTA)-NH_3 aqueous solution under heating and stirring conditions. The citric acid was then added into the solution. The molar ratio of total metal ions to EDTA and to citrate was controlled at 1:1.5:1. After a period of heating and stirring, the solution in the ceramic bowl was converted to a viscous gel, which was self -ignited and changed to ash. The resulting black ash-like material was calcined in air at 1000 ^{o}C for 3 h to form PBCF oxides. The structural phases of PBCF powders were examined using the powder X-ray diffraction (XRD) technique with Cu Kα radiation (D/Max-gA, Japan).

The powders of PBCF and samarium doped ceria (SDC) were thoroughly mixed with weight ratio of 50%:50%. The powder mixtures were calcined at 900, 950, 1000 and 1050 ^{o}C for 3 h in air, respectively. The phases of calcined mixtures were examined using XRD.

The green rectangular bars were obtained by uniaxial pressing the powders at 250 MPa. The resulting dimensions of the bars were 62mm×5mm×1.5mm (length, width and height). The green bars were sintered at 1100 ^{o}C for 5 h in air to obtain dense sintered bodies of PBCF oxides. The microstructures of the sintered bars were observed using scanning electron microscopy (SEM). The electrical conductivities of the sintered rectangle bars were measured using a standard DC four-probe technique with an Agilent multi-meter (34401A). The measurements were performed in air. The temperatures were controlled from 800 to 200 ^{o}C with change interval of 50 ^{o}C. The temperature was maintained at every point for 30 minutes to obtain conductivities at steady state conditions.

The volumetric expansion behaviors of PBCF oxides were measured using a dilatometer (NETZSCH, DIL 402 PC/4). The sintered rectangular bars were put in the dilatometer and heated up from the room temperature to 1000 ^{o}C with a heating rate of 10 ^{o}C min^{-1}. The bars were protected using air gas and nitrogen gas respectively. The volumetric expansions of the bars were recorded under different temperatures and gas environment. The SDC powders were dry-pressed at 250 MPa using a die to form pellets with diameter of 15 mm. The pellets were sintered at 1500 ^{o}C in air for 5 h to obtain dense electrolyte pellets. The cathode slurries of PBCO, PBCF0.2, PBCF0.4, PBCF0.6 and PBFO were painted on either side of the electrolyte pellets respectively with active area of 1.15 cm^2 to form symmetrical cells. The cells were sintered at 1000 ^{o}C in air for 3 h to bind the cathode onto the electrolyte. The platinum slurry was painted onto the either of the electrodes as the current collector. The electrochemical impedance spectra (EIS) of the symmetrical cells were measured using a Solatron 1260 frequency response analyzer in combination with a Solartron 1287 potentiostat. The sweeping frequency range of EIS measurement was from 0.1 to 10^5 Hz. The ASR was then obtained from EIS measurements. The powder mixture (NiO:SDC:starch = 60%:40%:20% in weight) was pre-pressed at 200 MPa in a die to form green anode substrate with a diameter of 15 mm. The loose SDC powder was then uniformly distributed onto the anode substrate and co-pressed at 250 MPa to form the green anode/electrolyte assembly. The green assembly was then sintered at 1400 °C for 5 h in air to densify the SDC membrane and form anode substrate/SDC electrolyte assembly. The cathode slurry was painted on SDC electrolyte, which was then sintered at 1000 °C for 3 h in air to form single cells of NiO-SDC/SDC/PBCF with different Fe doping levels. The fuel cells were tested from 550 to 700 °C with humidified hydrogen (~3% H_2O) as the fuel and the static air as the oxidant. The flow rate of the fuel was controlled at 40 ml min^{-1} using a mass flow meter (APEX). The current-voltage curves of the fuel cells were recorded using a Scribner 890ZV at a scanning rate of 30 mV s^{-1}. The EIS curves were measured over the frequency range of 0.1 to 10^5 Hz. The microstructural view of sintered PBCF rectangular bars was observed by SEM. The microstructure of post-test cells was examined using both the SEM and 3D X-ray tomography technique.

2.2 RESULTS AND DISCUSSION

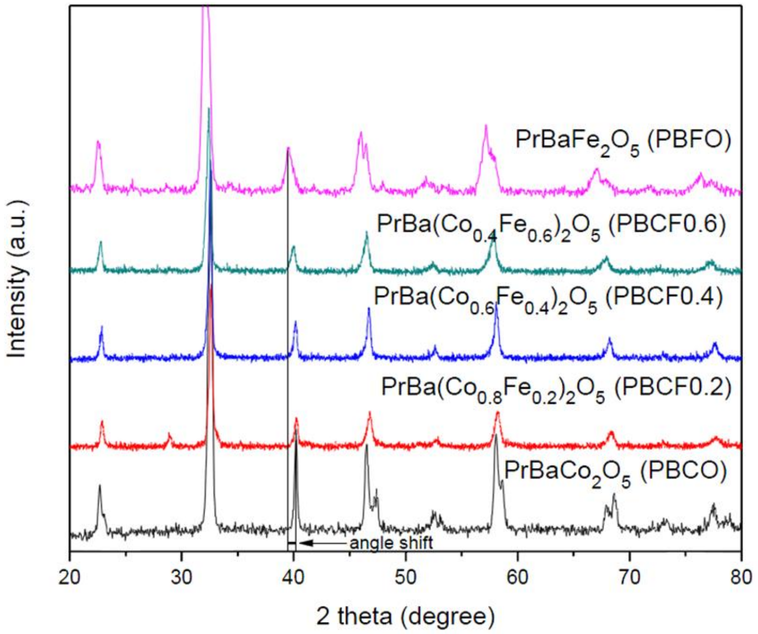

Figure 2. 1 XRD patterns of $PrBa(Co_{1-x}Fe_x)_2O_{5+\delta}$ oxides at room temperature in air.

Table 2. 1 The crystal lattice parameters of $PrBaCo_2Fe_{2-2x}O_{5+\delta}$ (x=0, 0.2, 0.4, 0.6 and 1.0) oxides calcined at 1000 °C for 3 h.

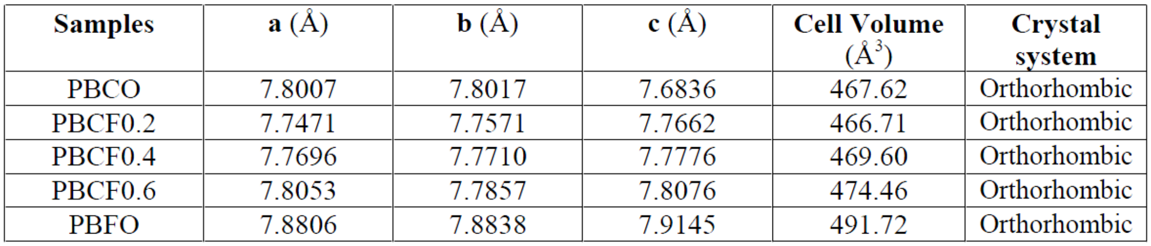

Samples	**a** (Å)	**b** (Å)	**c** (Å)	**Cell Volume** (Å^3)	**Crystal system**
PBCO	7.8007	7.8017	7.6836	467.62	Orthorhombic
PBCF0.2	7.7471	7.7571	7.7662	466.71	Orthorhombic
PBCF0.4	7.7696	7.7710	7.7776	469.60	Orthorhombic
PBCF0.6	7.8053	7.7857	7.8076	474.46	Orthorhombic
PBFO	7.8806	7.8838	7.9145	491.72	Orthorhombic

Shown in Figure 2.1 are the XRD patterns of the synthesized $PrBa(Co_{1-x}Fe_x)_2O_{5+\delta}$ oxides with different doping levels of Fe element. The oxide powders were calcined 1000 °C in air for 3 h and the XRD was measured in air at room temperature. The peaks of XRD correspond to the single orthorhombic phase. Since no peaks corresponding to other phases can be found, it is reasonable to believe that the Fe ions were incorporated into Co sub-lattice in all PBCF samples. The results also show that the characteristic peaks shifted toward the lower reflection angles when the Fe content increased (from x=0 to x=1). Such peak shifting implies that the lattice parameters of the oxides increase. The Fe doping effects on crystal lattice parameters were further obtained through the calculation analysis of the primitive patterns.

As shown in Table 2.1, the lattice parameter slightly increases with increasing the content of Fe dopant, e.g., a=7.7471 Å for PBCF0.2 and a=7.8806 Å for PBFO. The volume of the crystal unit cell also showed a little bit expansion from 466.71 Å^3 of PBCF0.2 to 491.72 Å^3 of PBFO. Since the ionic radii of Fe^{3+} (78.5 pm) is larger than that of Co^{3+} (75 pm), it is speculated that the incorporation of Fe^{3+} into the Co sub-lattice leads to the fact that the overlap of the electronic orbital of Fe and lattice oxygen is less than that of Co and lattice oxygen. Therefore the volume of crystal unit cell increased with increasing the Fe content.

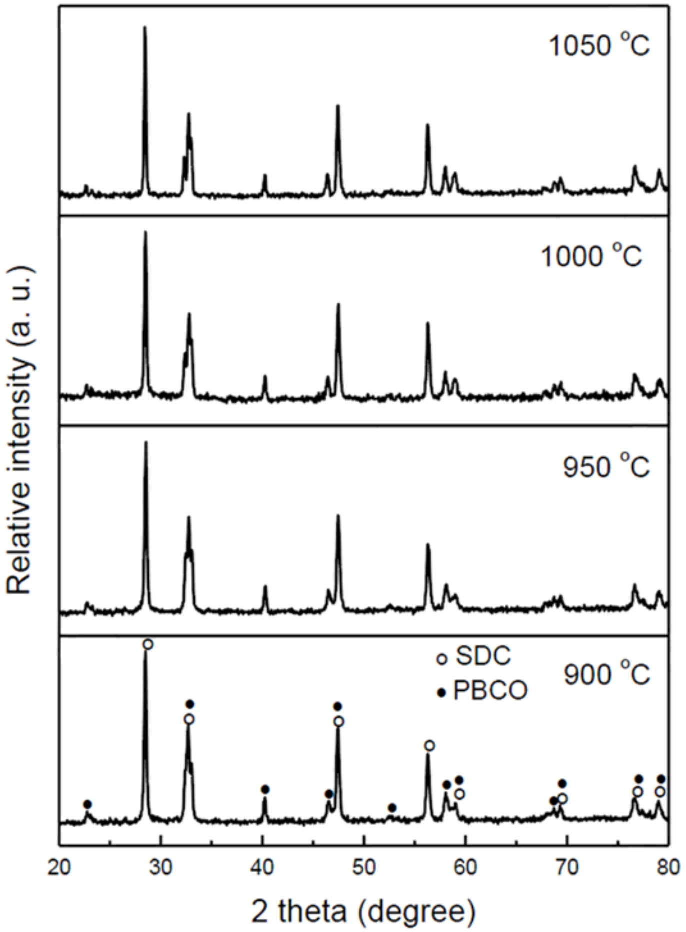

Figure 2. 2 The XRD patterns of SDC and PBCO mixing powders after calcined at different temperatures.

To examine the chemical compatibility of electrolyte and cathode materials, the mixture of SDC and PBCO powders (50:50 wt%) was calcined at 900, 950, 1000 and 1050 ^{o}C in air for 5 h respectively. The phases of calcined mixed powders were measured using XRD. As shown in Figure 2.2, the peaks correspond to the typical phase structures of fluorite SDC and layered perovskite of PBCO. No other phases can be found in the XRD patterns, indicating that no chemical reactions occurred between SDC and PBCO at the elevated temperature of 900-1050 ^{o}C. Usually, the operating temperature of the

SOFCs with SDC electrolyte and PBCO cathode is lower than 800 °C; further the sintering temperature of 1000 °C is employed to bond the cathode of layered perovskite PBCO to the SDC electrolyte during the cell fabrication process. Therefore, the XRD result from mixed powders calcined at 1050 °C can confirm that the SDC electrolyte and PBCO cathode are chemically compatible during sintering fabrication and electrochemical testing process.

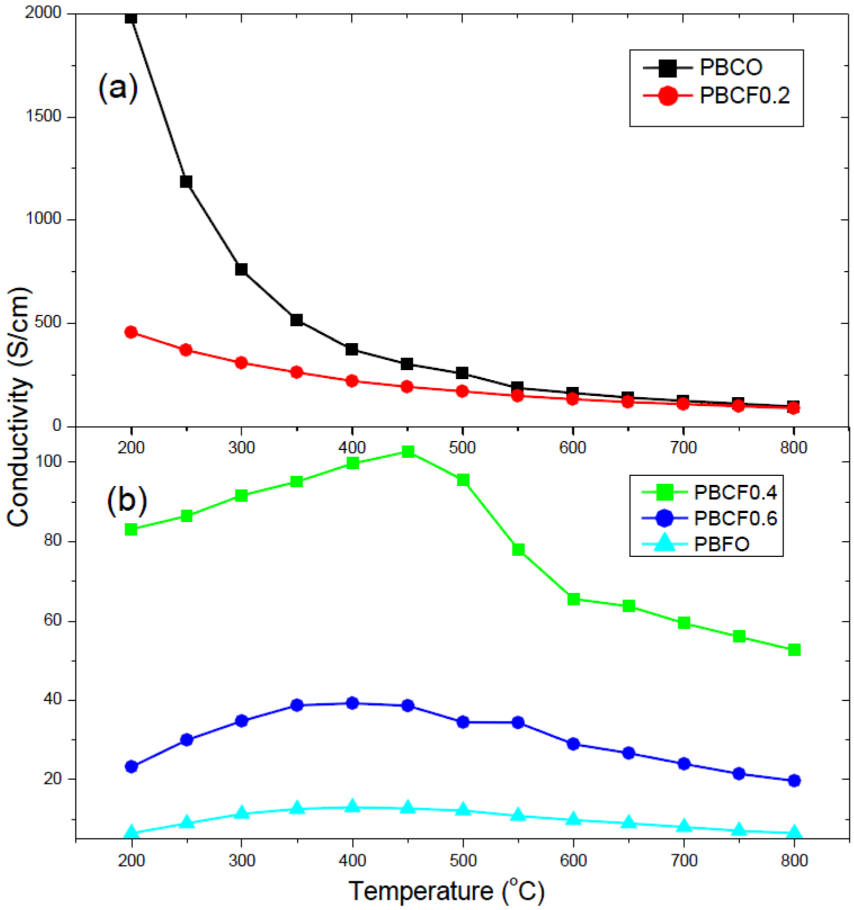

Figure 2. 3 The electrical conductivities of PBCF oxides: (a) PBCO and PBCF0.2; (b) PBCF0.4, PBCF0.6 and PBFO.

The electrical conductivities of the sample bars were measured in air under the temperature of 200-800 °C using DC four-probe technique. The results are shown in Figure 2.3. When the Fe doping level is relatively low (x=0, 0.2), the conductivity of the samples (PBCO, PBCF0.2) showed a metal conduction behavior (Figure 2.3a), increasing with decreasing temperatures. At the low temperature of 200 ^{o}C, the conductivity reached a maximum value of 2000 S cm^{-1} and 500 S cm^{-1} for PBCO and PBCF0.2 respectively. Obviously, the Fe dopant significantly reduced the conductivity of PBCO at 200 ^{o}C.

As mentioned before, the overlap of the electronic orbital of Fe and lattice oxygen is less than that of Co and lattice oxygen after incorporating Fe^{3+} into the Co sub-lattice. The decrease of electronic orbital overlap can potentially increase the width of band gap for electron conduction. Therefore, the corresponding conductivity was reduced. The conductivities of PBCO and PBCF0.2 at 800 ^{o}C reached 97 and 89 S cm^{-1} respectively.

Although the conductivities of PBCO and PBCF0.2 at 800 ^{o}C are lower than those at 200 ^{o}C, they can satisfy the minimum requirement of cathode materials for intermediate temperature SOFCs (600 – 800 ^{o}C). When the Fe doping level increased (x=0.4, 0.6, and 1.0), the conductivities of PBCF were further decreased (Figure 2.3b). For all samples, it can also be seen that the dependence of conductivity variation on increasing temperatures showed a typical metal-insulator transition behavior. Depending on the Fe doping level, the maximum conductivity was obtained at a little bit different temperature, i.e., 103 S cm^{-1} at 450 ^{o}C for PBCF0.4, 40 S cm^{-1} at 400 ^{o}C for PBCF0.6 and 13 S cm^{-1} at 400 ^{o}C for PBFO respectively.

The sintering ability of PBCF oxides with different Fe doping level was studied. The green PBCF bars were sintered at 1100 ^{o}C for 5h. Here the sintering temperature of 1100 ^{o}C is a little bit higher than that for cathode fabrication of SOFCs. The sintering quality was examined using SEM.

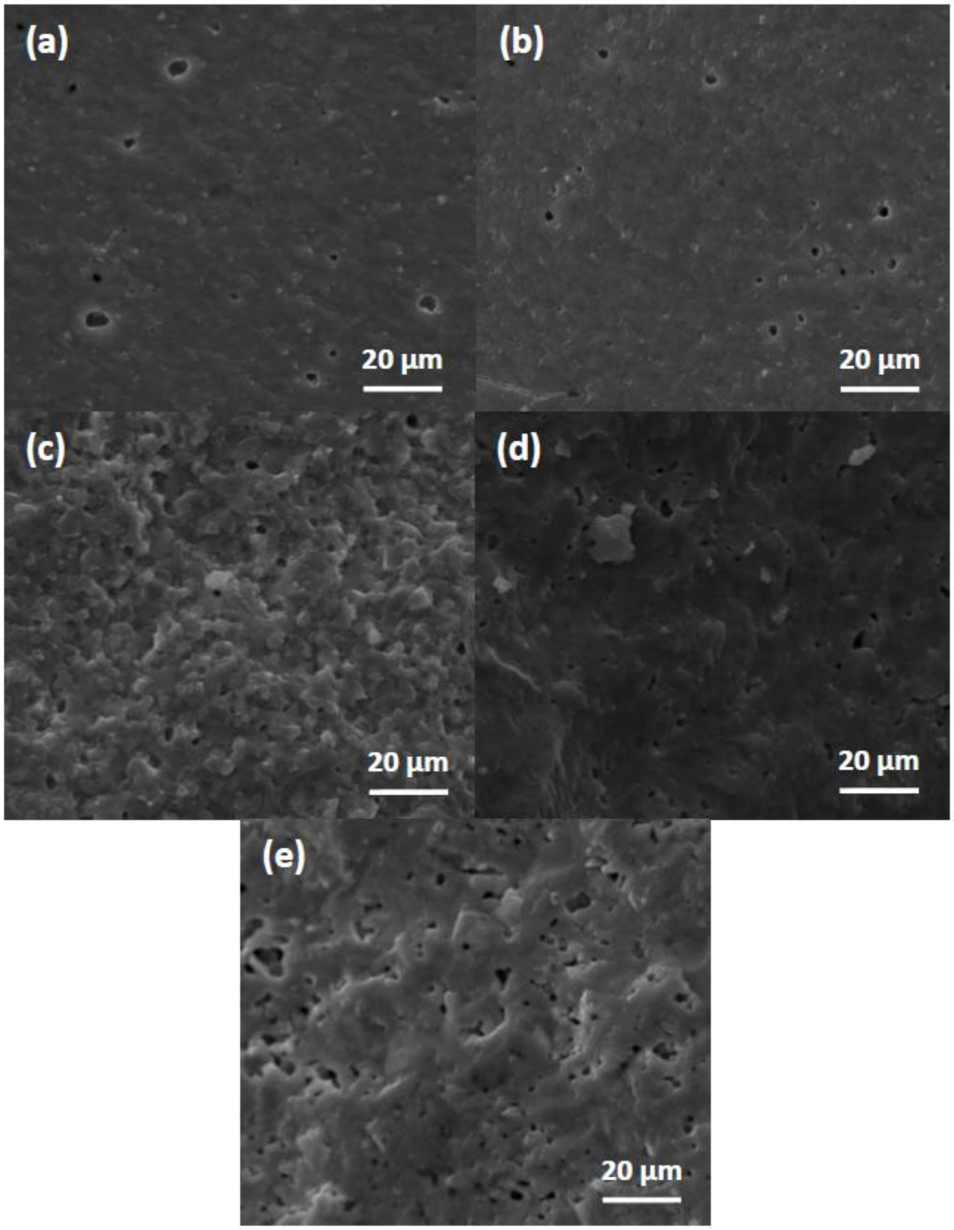

Figure 2. 4 SEM images of cross-section view for PBCF oxides sintered 1100 ^{o}C for 5 h: (a) PBCO; (b) PBCF0.2; (c) PBCF0.4; (d) PBCF0.6; (e) PBFO.

As shown in Figure 2.4(a) and (b), the sintered PBCO and PBCF0.2 bars have relatively dense cross sections with observable little tiny close pores. When the Fe dopant content increased to 0.4, the little open pores with diameter of 2~3 µm can be observed in PBCF0.4 sample and the grain boundaries became clear (Figure 2.4c). With further increasing the Fe content, both the number and size of the open pores in the sample bars of PBCF0.6 and PBFO gradually increased and formed porous structures (Figure 2.4d and e). The results clearly showed that high content of Co element in PBCF oxides facilitated the sintering of such oxides.

The expansion behavior of PBCF sample bars was measured using a dilatometer from room temperature to 1000 °C in air. Figure 2.5 shows the measurement results, in which the horizontal axis is the temperature while the vertical axis represents the expansion rate of the sample bars. The TEC of PBCO bar is 28.19×10^{-6} 1/K. With increasing the Fe element content, the TEC value of sample bar reached 26.76×10^{-6} 1/K, 25.9×10^{-6} 1/K, and 23.94×10^{-6} 1/K for PBCF0.2, PBCF0.4, and PBCF0.6, respectively, indicating that high Fe doping level is favorable for reducing the TEC value of PBCF. Meanwhile, it is also indicated that the replacement of Fe in B-site of layered perovskite might introduce a new cobalt-free cathode for SOFC with low TEC.

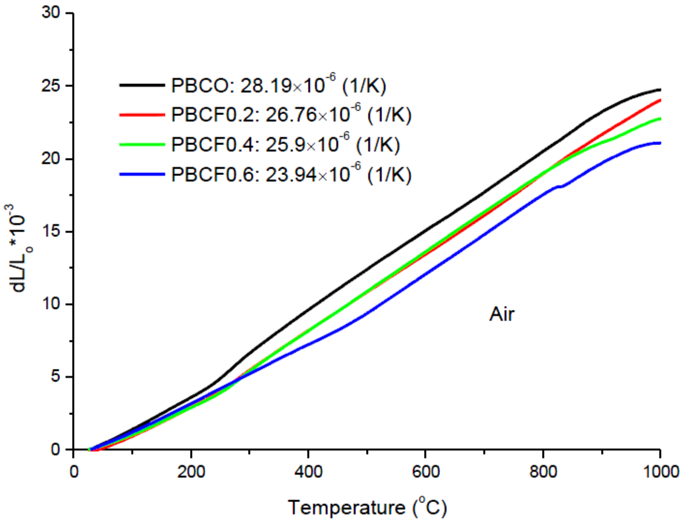

Figure 2. 5 The crystal expansion behaviors at test temperature range of 25-1000 °C in air (P_{O2}= 0.21 atm).

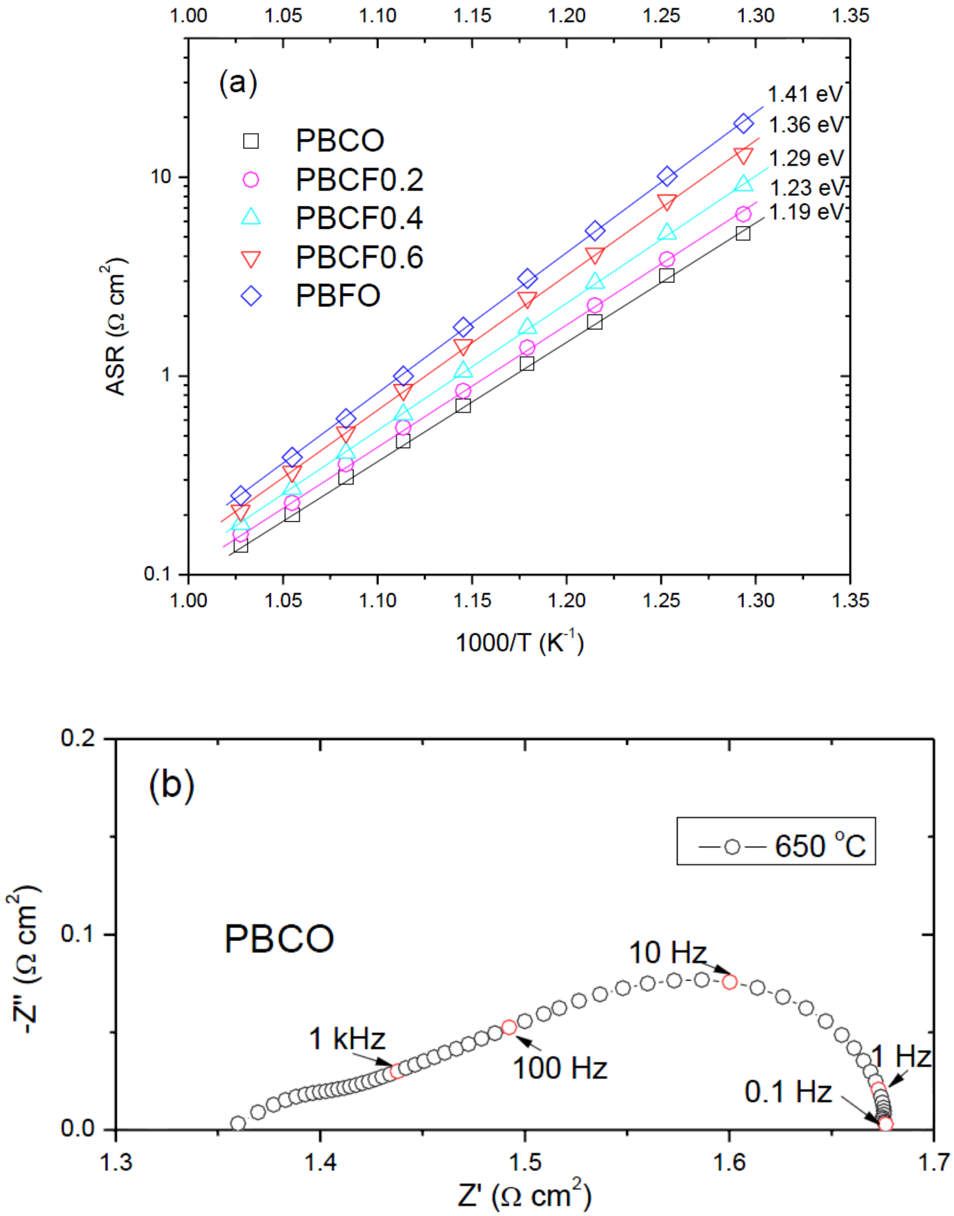

Figure 2. 6 (a) The ASR of PBCF oxides in symmetric cells of PBCF/SDC/PBCF at different temperatures; (b) a typical raw impedance plot of PBCO at 650 ^{o}C.

Fig. 2.6(b) shows a typical EIS of the symmetrical cell PBCO/SDC/PBCO at 650^{o}C. The intercept with the horizontal axis at the low frequency represents the overall resistance of the cell while the intercept at the high frequency indicates the ohmic resistance induced mainly by the electrolyte. The difference between the low frequency intercept and the high frequency intercept is the polarization resistance of the cell, contributed by the electrodes on both sides. The half of the difference represents the electrode polarization resistance. Fig. 2.6(a) shows the ASR of the symmetrical cell PBCF/SDC/PBCF at different temperatures. The ASR of PBCO electrode at 650 ^{o}C was 0.31 Ωcm^2. With increasing the Fe content from y=0 to y=1, the ASR increases from 5.21 Ω cm^2 to 18.6 Ω cm^2 respectively at 500 ^{o}C. The corresponding activation energy increases from 1.19 eV for PBCO to 1.41 eV for PBFO respectively.

The results indicate that Co-rich PBCF oxide may reduce the corresponding electrode polarization resistance and improve the catalytic activity. In fact, high Co content would lead to relatively high oxygen vacancy concentration in the oxides. The results are also consistent with the conductivity of PBCF oxides in Fig. 2.3. On the other hand, the high Co content may cause relatively high TEC values. Therefore the tradeoff might be needed between the catalytic activity and the structural reliability when PBCF is utilized as the cathode materials for SOFCs.

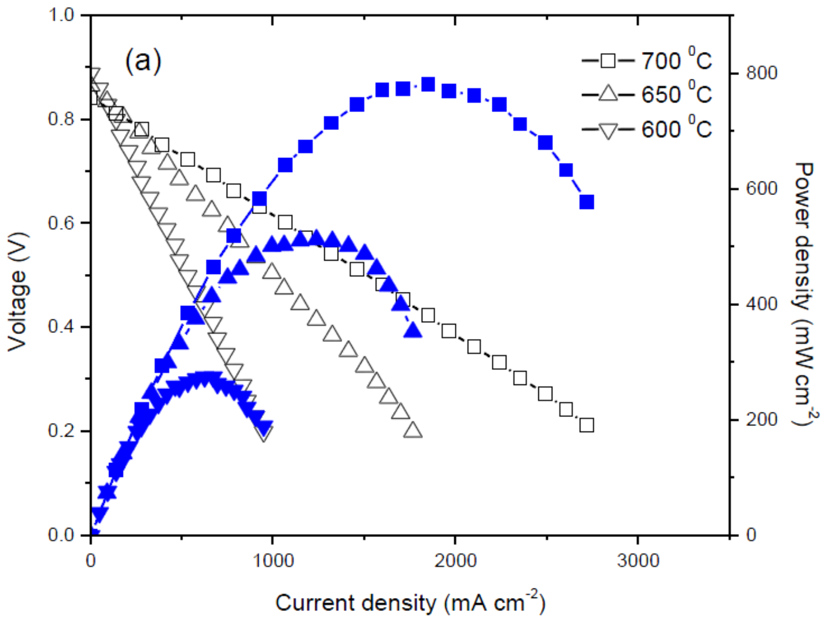

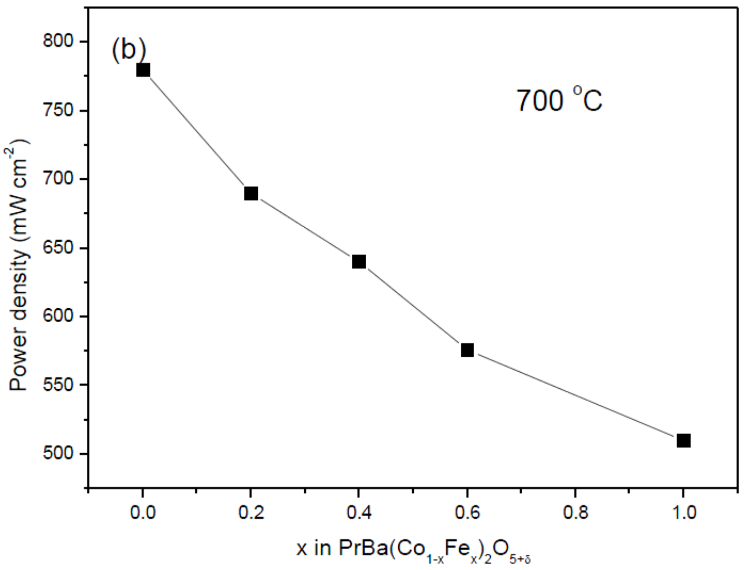

Figure 2. 7 (a) The *I-V* and *I-P* curves of Ni-SDC/SDC/PBCO cell at different operation temperatures; (b) Peak power densities of PBCF cathodes at 700 ^{o}C.

The electrochemical performance of the anode supported cell Ni-SDC/SDC/PBCO was evaluated under the temperature range of 600-700 ^{o}C, in which the humidified H_2 (~3% H_2O) is utilized as a fuel and the static ambient air as the oxidant. As shown in Fig. 2.7, the open circuit voltage (OCV) is about 0.9V and shows a slightly decrease with increasing the temperatures. Since the doped ceria is not a perfect oxide ionic conductor, the reduction of Ce from Ce^{4+} to Ce^{3+} in a reducing condition (mainly anode side) causes an internal current or current leakage in the electrolyte. As a consequence, the OCV was reduced from the theoretical value (~1.1V). The peak power densities of the cell are 780, 520 and 275 mW cm^{-2} at 700, 650 and 600 ^{o}C, respectively.

The EIS of the cell under the OCV condition are presented in Fig. 2.8. The difference between the low frequency intercept and high frequency intercept with the horizontal axis represents the overall polarization resistance contributed from both the anode and cathode electrode.

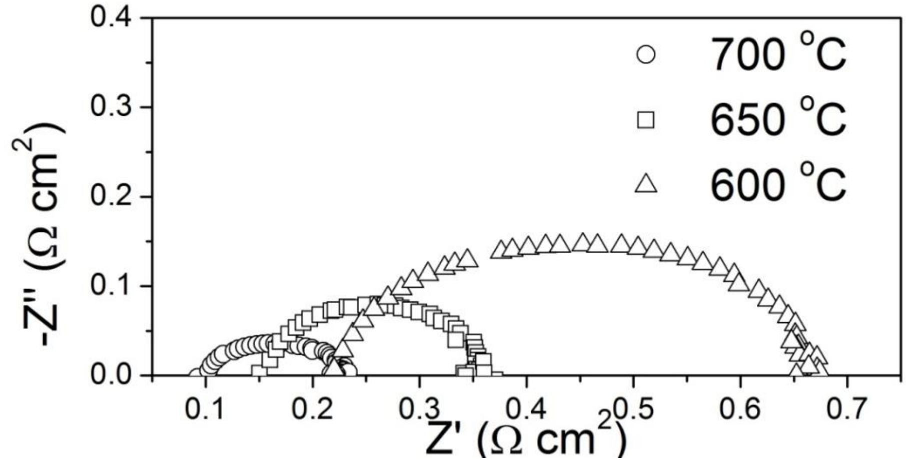

Figure 2. 8 Impedance spectra of Ni-SDC/SDC/PBCO cell.

When the temperature was increased from 600 °C to 700 °C, the polarization resistance was decreased from 0.44 Ωcm^2 to 0.13 Ωcm^2. With different Fe dopant levels in the PBCF cathode, the peak powder densities of the corresponding cells are shown in Fig. 3.3.8b. Obviously, the peak power density decreases with increasing the Fe content, e.g., 690 mW cm^{-2} for PBCF0.2, 640 mW cm^{-2} for PBCF0.4, 576 mW cm^{-2} for PBCF0.6 and 510 mW cm^{-2} for PBFO at 700°C respectively. The results are consistent with the conductivity (Fig. 2.3) and activation energy (Fig. 2.6) obtained above, where high Fe content in PBCF leads to decreased conductivity and increased activation energy.

2.3 SUMMARY

The layered perovskite $PrBa(Co_{1-x}Fe_x)_2O_5$ (x=0, 0.2, 0.4, 0.6, and 1.0) system has been comprehensively studied, including the synthesis, chemical and physical properties, compatibility with typical electrolyte of SDC. XRD analysis showed that the Fe substitution in the oxides leads to the increase of both lattice parameters and the volume of crystal unit cell. Four-probe measurement indicated that increasing the Fe content in the oxides leads to the variation from the metal conduction behavior to the metal-insulator conduction behavior. The high Fe content decreases the overall conductivity of the oxides. The EIS measurement with symmetrical cells further confirmed that high Fe content in the oxides increases the ASR and activation energy. The conductivity and activation energy of PBCF were cross-verified by electrochemical performance of the corresponding button cells, where the peak power density of the cell decreases with increasing the Fe content in PBCF cathode. Results also showed that PBCO is chemically compatible with SDC in the temperature range of 900-1050 ^{o}C.

CHAPTER 3

EVALUATIONS OF LAYERED PEROVSKITE OXIDES AS CATHODES FOR OXIDE-ION CONDUCTING SOFC

Layered pervoksite oxides can be described with general formula of $AA'B_2O_{5+\delta}$ with the A ´site being Ba element. It has been found that when A ´site is partially substituted by Sr, it could potentially improve the conductivity of layered pervoskite oxides. This hypothesis has been confirmed by recent study from Irvine *et al.*,[115] where Sr-doped oxide $PrBa_{0.5}Sr_{0.5}Co_2O_{5+\delta}$ (PBSC) demonstrated excellent ASR values based on gadolinia-doped ceria (GDC) electrolyte, and could be potentially employed as cathode material for IT-SOFCs. Nevertheless, these cobalt-based cathodes often suffer from problems like poor chemical stability in CO_2, high TECs, ease of evaporation, as well as high cost of cobalt element. Partial or full substitution of cobalt element with other elements such as Fe or Nd etc. in these materials could potentially mitigate these disadvantages while keeping adequate electrochemical activity of cobalt-containing oxides for ORR. In this work, the feasibility of PBSC as a cathode material for IT-SOFCs is examined based on oxide-ion conducting SDC electrolyte by investigating the symmetric half cells and fuel cells. Furthermore, layered perovskite $GdBaCoFeO_{5+\delta}$ (GBCF) with partial Fe doping and cobalt-free $GdBaFe_2O_{5+\delta}$ (GBFO) with full Fe doping are also investigated to explore the effect of Fe doping in layered perovskites on cell performance.

3.1 PRBASRCOO$_{5+\Delta}$ (PBSC) AS CATHODE CANDIDATE

3.1.1 EXPERIMENTAL

PBSC powders were synthesized using modified Pechini process, where citrate and EDTA were employed as parallel complexing agents. Pr_6O_{11} was first dissolved in nitric acid; the calculated amount of $Ba(NO_3)_2$ 9H_2O, $Sr(NO_3)_2$ and $Co(NO_3)_2 \cdot 6H_2O$ was dissolved in EDTA-NH_3 aqueous mixed solution under heating and stirring conditions. An appropriate amount of citric acid was then added in the solution. After gradually converted into viscous gel under heating and stirring conditions, the solution was ignited to flame and result in ash. The resulting ash-like material was afterwards calcined in air at 1000 ^{o}C for 10 h. The fine PBSC powders were then mixed thoroughly with a 6 wt% ethylcellulose-terpineol binder (V006, Heraeus) to obtain the cathode slurry. Powders of SDC electrolyte were synthesized by glycine-nitrate process (GNP) and calcined at 800 ^{o}C for 2 h for obtaining the pure fluorite phase. The phase identification of prepared cathode powders was studied with X-ray powder diffraction by Cu-Kα radiation (D/Max-gA, Japan). A scan rate of 5° min^{-1} was used in the range of $20^{\circ}<2\theta<80^{\circ}$.

The SDC powder was dry-pressed into pellets at 250 MPa and sintered in air at 1400 ℃ for 5 h to obtain dense pellets. The as-prepared cathode slurry was painted on either side of electrolyte pellet with active area of 1.15 cm^2 to form symmetrical cell (PBSC/SDC/PBSC). The cell was sintered at 1000 ^{o}C in air for 3 h. Platinum (Pt) was used as the current collector on either of the electrodes. The polarization resistance of electrode materials was measured using AC impedance spectroscopy with as-prepared symmetrical cells. The EIS were obtained using a Solatron 1260 frequency response analyzer in combination with a Solartron 1287 potentiostat. The sweeping frequency range of EIS measurement was from 0.1 Hz to 5 MHz. The ASR was employed to describe all of resistances resulting from gas-electrode interface, bulk electrode, as well as electrode-electrolyte interface.

The anode-supported SDC bi-layer (Φ=15 mm) was prepared using a dry-pressing method. NiO + SDC + starch mixture (60%: 40%: 20% in weight) was pre-pressed at 200 MPa as an anode substrate. Then loose SDC powder synthesized above was uniformly distributed onto the anode substrate, co-pressed at 250 MPa and sintered subsequently at 1400 °C for 5 h to densitify the SDC membrane. The cathode slurry was then painted on SDC electrolyte film, and sintered at 1000 ℃ for 3 h in air to form single cells of NiO-SDC/SDC/PBSC. The cells were tested from 550 to 700 °C with humidified hydrogen (~3% H_2O) as fuel and the static air as oxidant. The flow rate of fuel was about 40 ml/min controlled by mass flow meter. The voltage-current curves were recorded by Scribner 890ZV at a 30 mVs^{-1} scan rate. Impedance spectra were measured over the frequency range from 0.01 Hz to 10^5 Hz under open-circuit conditions. A scanning electron microscope (SEM) was used to observe the microstructure of the post-test cells.

3.1.2 RESULTS AND DISCUSSION

As shown in Fig. 3.1, the as-prepared powder of PBSC exhibits a pure layered perovskite phase with orthorhombic lattice geometry of space group (*Pmmm*) without any peaks attributable to impurities.[115] Fig. 3.2 shows the SEM image of tri-layer cell Ni-SDC/SDC/PBSC after electrochemical test. It can be seen that the SDC membrane is completely dense and the thickness is about 20 μm. The electrolyte layer adheres to both porous anode substrate and cathode layer fairly well, no cracks or pores can be observed from the cross-section view. The PBSC layer is porous with thickness about 10 µm. The top layer of silver paste has good contact with PBSC cathode for current collection.

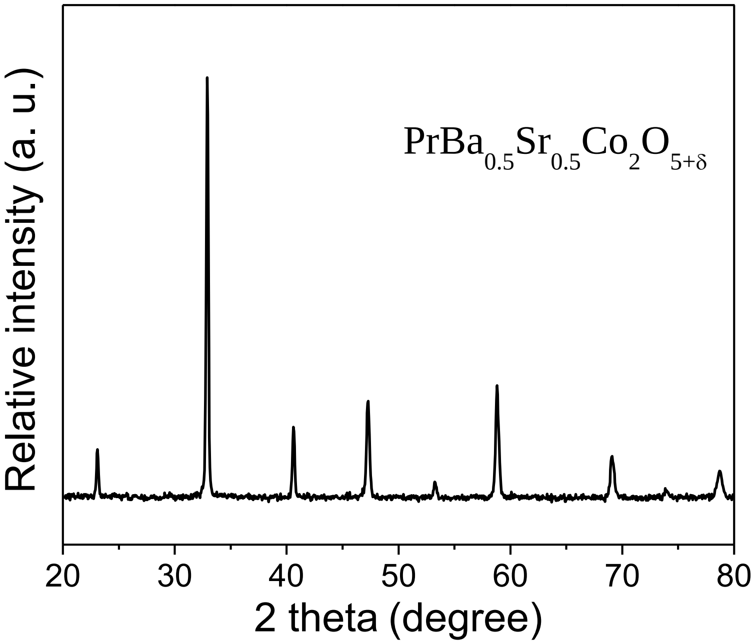

Figure 3. 1 XRD pattern for the layered $PrBa_{0.5}Sr_{0.5}Co_2O_{5+\delta}$ (PBSC) perovskite powders.

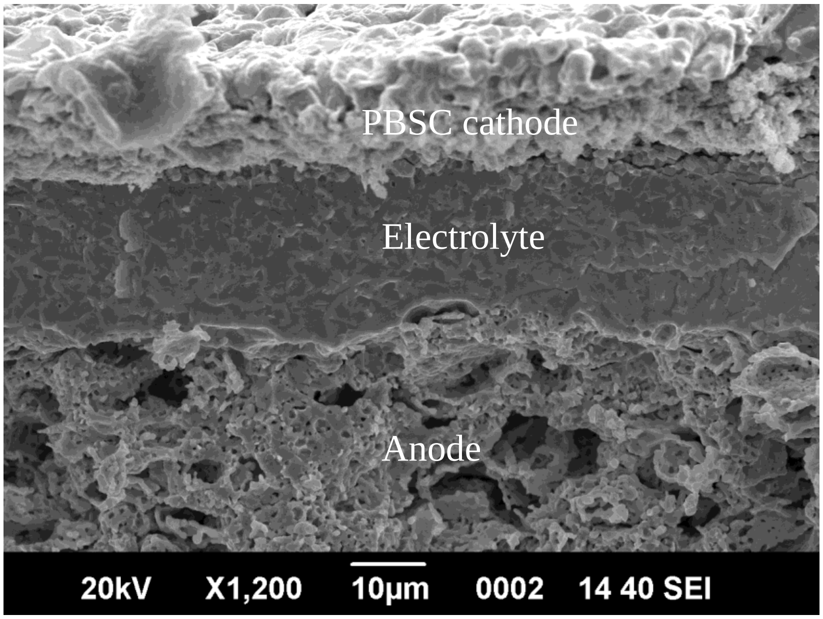

Figure 3. 2 The cross-section view of tri-layer cell after electrochemical testing.

To evaluate properties of PBSC as cathode material, ASR values in a symmetric cell of PBSC/SDC/PBSC were measured using impedance spectroscopy in operating temperature range between 500 and 700 ^{o}C in air. The corresponding cathode ASR (Fig. 3.3a) was determined from raw impedance plots as shown in Fig. 3.3b, where the high-frequency offset is generally thought to be induced by electrolyte resistance since the SDC pellet was thick and the radius of the arc is attributed to the cathode resistance.[27] The ASR at 650 ^{o}C was ~0.23 Ω cm^2, a value similar to that reported by Irvine *et al.* based on $Ce_{0.9}Gd_{0.1}O_{1.9}$ electrolyte. The nearly linear dependence of natural logarithm of (σT) on T^{-1} was used to calculate the activation energy (E_a). The value of E_a is 124 kJ mol^{-1} less than other E_a values reported in literature, e.g. E_a= 164 kJ/mol for $La_{0.8}Sr_{0.2}CoO_{3-\delta}$, E_a = 183 kJ/mol for $La_{0.8}Sr_{0.2}FeO_{3-\delta}$ or E_a = 202 kJ/mol for $La_{0.8}Sr_{0.2}Co_{0.8}Fe_{0.2}O_{3-\delta}$.[116] It is obvious that PBSC exhibits unusually high activity for oxygen activation and mobility. This observation is consistent with that reported by Taskin, in which the oxygen diffusion in layered perovskites becomes very fast at relatively low temperature conditions, *e.g.* exceeding 10^{-5} cm^2/s at 600 ^{o}C for $GdBaCo_2O_{5+\delta}$.[109]

In order to identify the activation energy of individual electrode steps on PBSC cathode in symmetrical cell, the equivalent circuit shown in Fig. 3.3b is obtained for impedance spectra through curve-fitting technique using software Zview. In the equivalent circuit, L is an inductance induced by the cables, R_1 is ohmic resistance, R_2 and R_3 parallel with C_1 and C_2, representing the high frequency arc and low frequency arc respectively, are attributed to oxygen reduction in electrode. Similar to Figure 4a, Arrhenius-like behavior of R_2 and R_3 was found and the activation energy of 148 KJ/mol and 96 KJ/mol, corresponding to R_2 and R_3 respectively, was obtained.

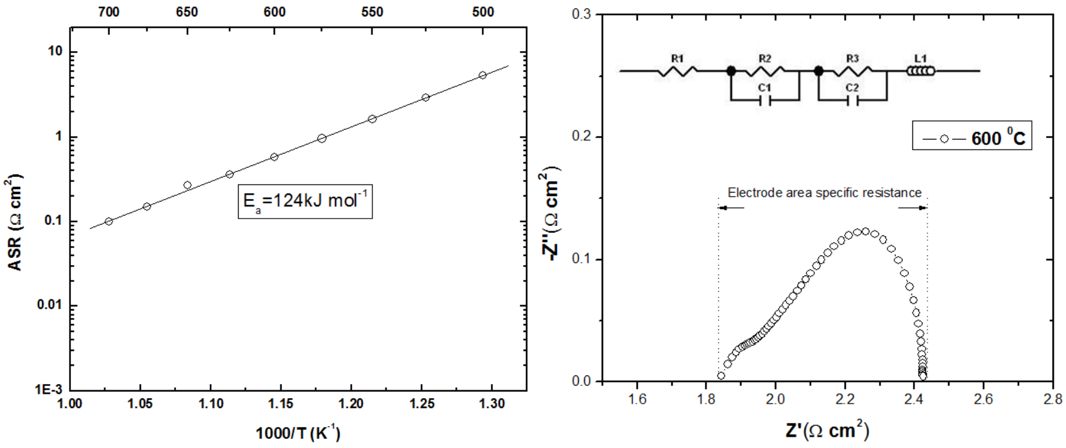

Figure 3. 3 (a) The area-specific-resistance as a function of temperature for a symmetric PBSC/SDC/PBSC cell; (b) a typical impedance spectra obtained at 600 ^{o}C.

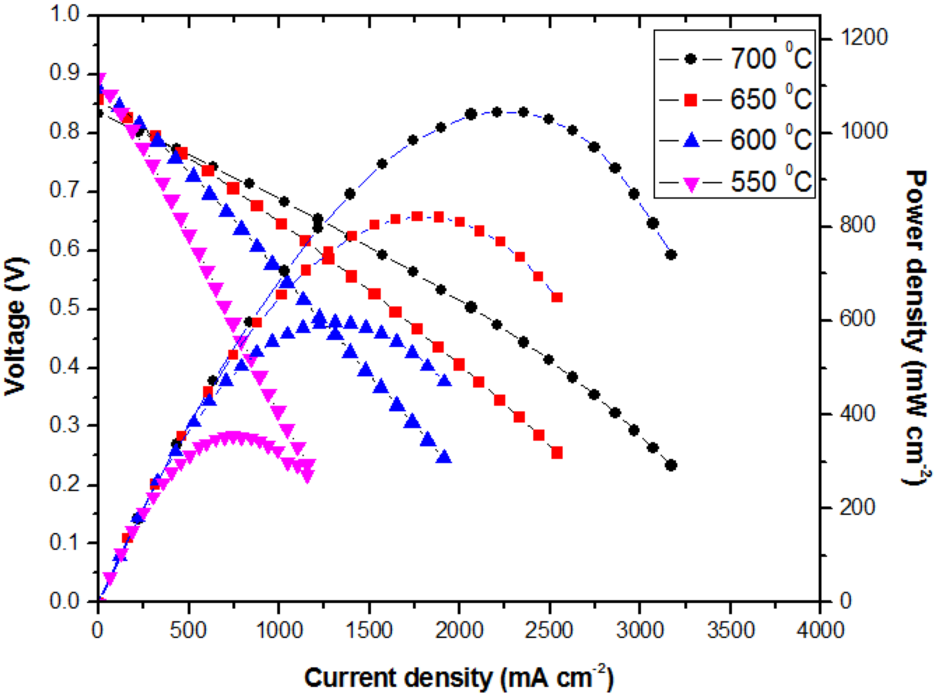

Figure 3. 4 Performance of the as-prepared cell with hydrogen at different temperatures.

The *I-V* curve and *I-P* curve of the as-prepared cell with PBSC as cathode, as shown in Fig.3.4, were obtained in operating temperature range of 550-700 ^{o}C, in which humidified H_2 (3% H_2O) is utilized as a fuel and static ambient air as the oxidant. The

OCV is lower than 1.0V, and increases with the decrease of the operating temperature. The decrease of the cell OCV is induced by the fact that the doped ceria is not a pure oxide ion conductor; the reduction of Ce^{4+} to Ce^{3+} in SDC film causes an internal current.[117] Peak power densities of the cell were 1045, 822, 598 and 355 mW cm^{-2} at 700, 650, 600 and 550 ^{o}C, respectively. The cell performance is very encouraging and suggests that PBSC is a very promising cathode material for IT-SOFCs.

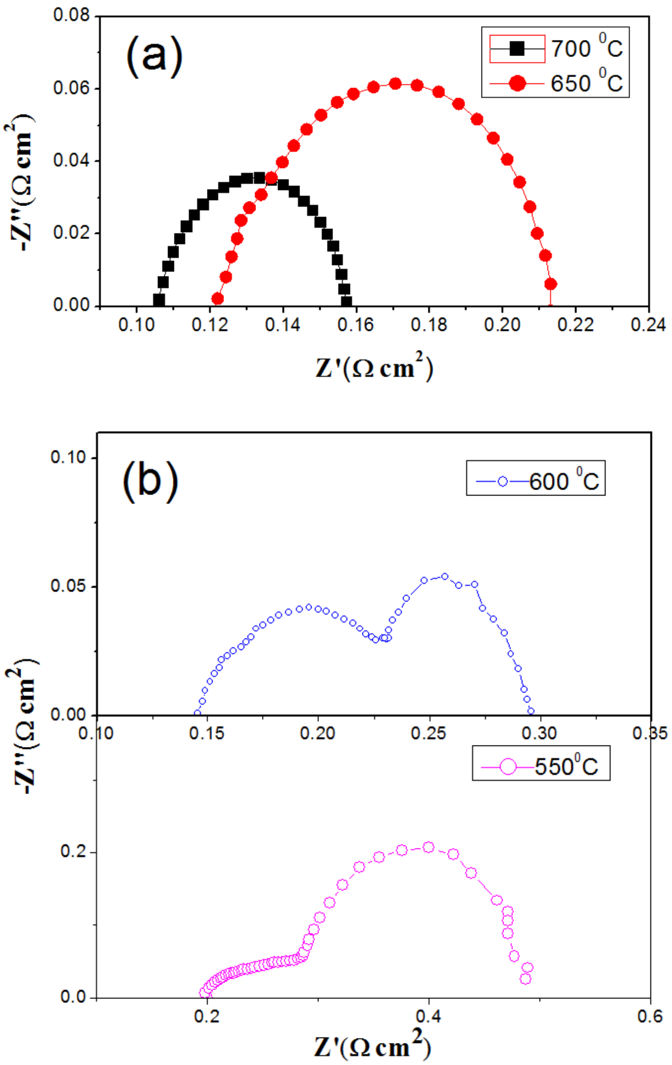

Figure 3. 5 Impedance spectra of the cell Ni-SDC/SDC/PBSC under open circuit conditions from 550 ^{o}C to 700 ^{o}C.

The electrochemical impedance spectra of cells under OCV are presented in Fig.

3.5. There are two flattening arcs in each of impedance spectra, indicating that at least two electrode processes are involved in oxygen molecule reduction. The high frequency arc could be attributed to polarization during charge transfer process. The low frequency arc might be attributed to the oxygen adsorption and desorption on the cathode surface and the diffusion of the oxygen ions.[118] Increase operating temperatures lead to significant reduction of interfacial polarization resistance (R_p), typically from 0.285 Ω cm^2 at 550 °C to 0.05 Ω cm^2 at 700 °C, respectively. It is worth noting that the R_p values of PBSC cathode are lower than those of the cell with a BSCF-SDC composite cathode when operating temperature is at or below 600 °C. The latter obtained the R_p values of 0.16 Ω cm^2 at 600 °C and 0.42 Ω cm^2 at 550 °C, respectively.[119]

The high performance observed from experimental results of cell Ni-SDC/SDC/PBSC can be understood using the microstructure characteristic of layered perovskite cathode PBSC. It is well known that the ionic conductivity is dependent on both the chemical diffusion coefficient D and the surface exchange coefficient K. Due to the ordering A-sites in layered perovskite oxides, the rate of the oxygen up-taking is much faster than that in simple ABO_3-type perovskite. Similarly it is also much easier to release oxygen from layered oxides. Taskin et al. has established that the ordering of the A-site sub-lattice in layered structure significantly enhances the oxygen relaxation rate since oxygen atoms can be partially or even completely removed from the Pr^{3+} planes, generating numerous oxygen vacancies in the crystal lattice.[109]

The short-term stability of Ni-SDC/SDC/PBSC cell was also investigated. The cell was running for a few days with a constant voltage loading of 0.5V and a constant operating temperature condition of 600 °C, the corresponding cell current response was recorded. As one can see from Fig. 3.6 that the cell current response is fairly stable, no detectable degradation is observed, implying stable electrochemical properties of cathode material PBSC and reliable bonding between electrode and electrolyte, the latter is shown in Fig.3.2.

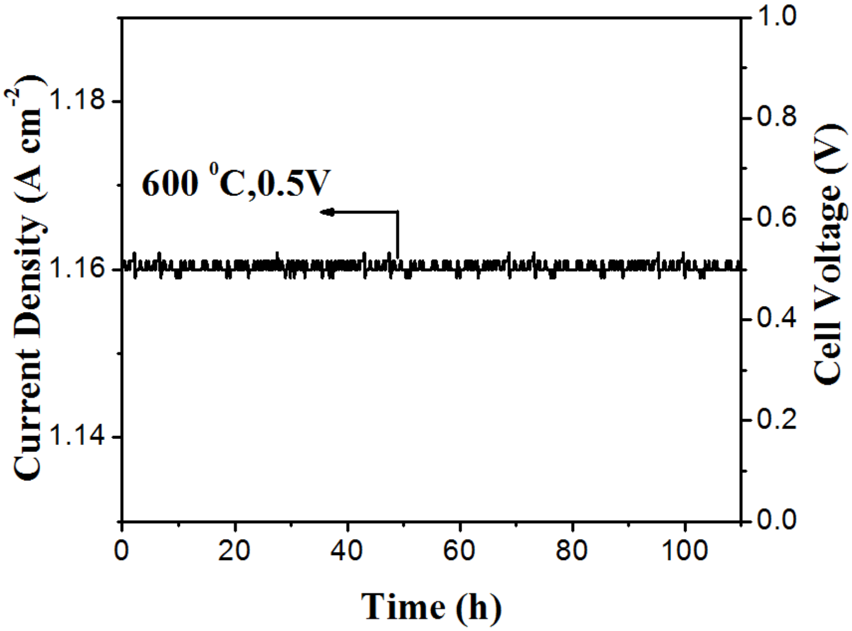

Figure 3. 6 Short-term stability of the cells tested at a constant cell voltage of 0.5 V at 600 °C.

3.1.3 SUMMARY

The A-site-ordered layered perovskite PBSC exhibited unusually high activity for oxygen activation and mobility. In the symmetrical cell system, the ASR of 0.23 Ω cm^2 was achieved at 650 °C for cathode polarization. The low activation energy (E_a) demonstrated the excellent catalytic activity for oxygen reduction. Anode-supported single cells based on SDC electrolyte and PBSC cathode were fabricated and evaluated. The maximum output density reached 1045 mW cm^{-2} at 700 °C. The low interfacial polarization resistance is as low as 0.285, 0.145, 0.09 and 0.05 Ω cm^2 at 550, 600, 650 and 700 °C, respectively. The short-term durability test result indicated the practical viability of this promising layered perovskite cathode.

3.2 GDBACO$_{0.5}$FE$_{0.5}$O$_{3-\Delta}$ (GBCF) AND GDBAFEO$_{3-\Delta}$ (GBFO) AS CATHODE CANDIDATES

3.2.1 RESULTS AND DISCUSSION

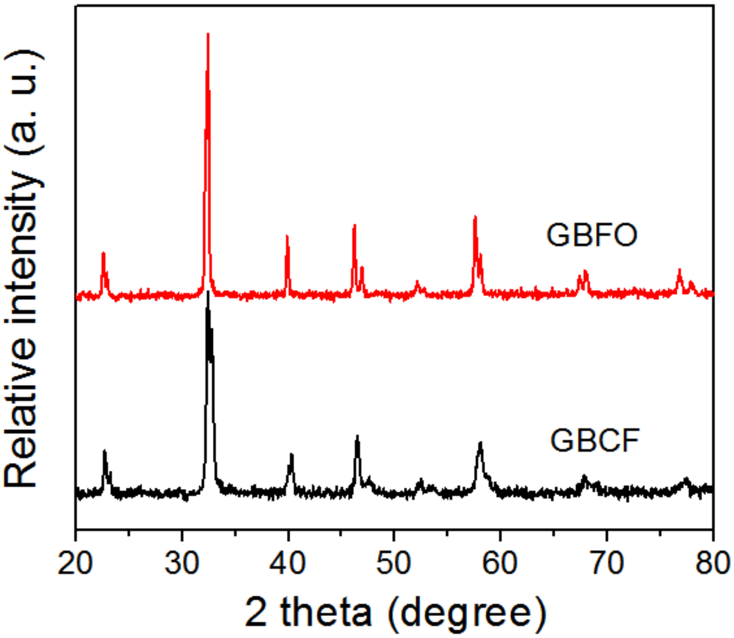

Figure 3. 7 XRD pattern for the layered GBCF and GBFO perovskite powders.

For GBCF and GBFO, the as-prepared powders exhibit the pure layered perovskite phase structure without any peaks attributable to impurities in Figure 3.7.[53,115] The diffraction peaks are identical with $GdBaCo_2O_{5+\delta}$ reported in the literature by A. Tarancón *et al.*.[40] The partial substitution of Fe at B site didn't affect the formation of layered perovskite phase.

Fig. 3.8 shows the SEM image of tri-layer cells Ni-SDC/SDC/GBCF and Ni-SDC/SDC/GBFO after electrochemical testing. It can be seen that the SDC membrane is completely dense and the thickness is about 20 μm. The uniform holes in porous anode layer after completely reduced at H_2 atmosphere is due to well mixed of NiO, SDC and starch. No cracks can be found in SEM image of tri-layer cell. The cathode adheres to the electrolyte fairly well, which is probably due to the replacement of cobalt element with Fe element. The reduction of cobalt element from high valence state to low valence state and the loss of lattice oxygen lead to the high TEC of cobalt containing cathode material, as a result, the replacement of cobalt element with Fe element can potentially mitigate such a high thermal expansion.[120]

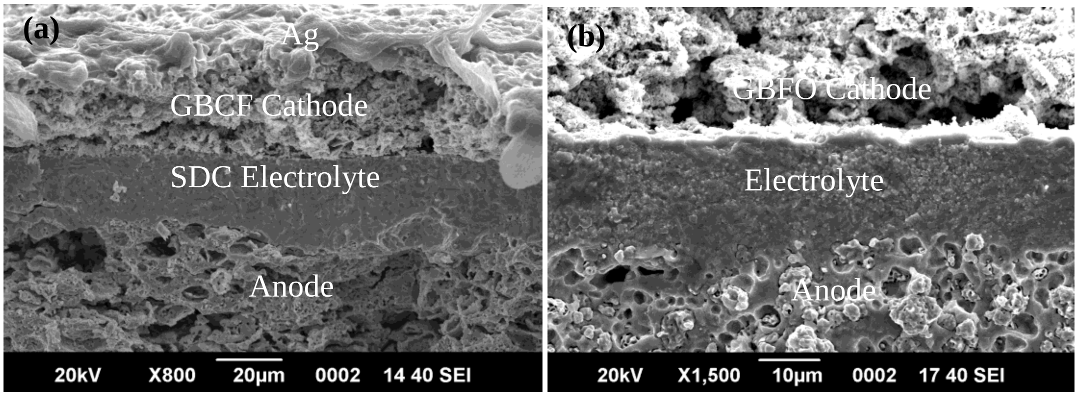

Figure 3. 8 The cross-section view of tri-layer cells after electrochemical testing.

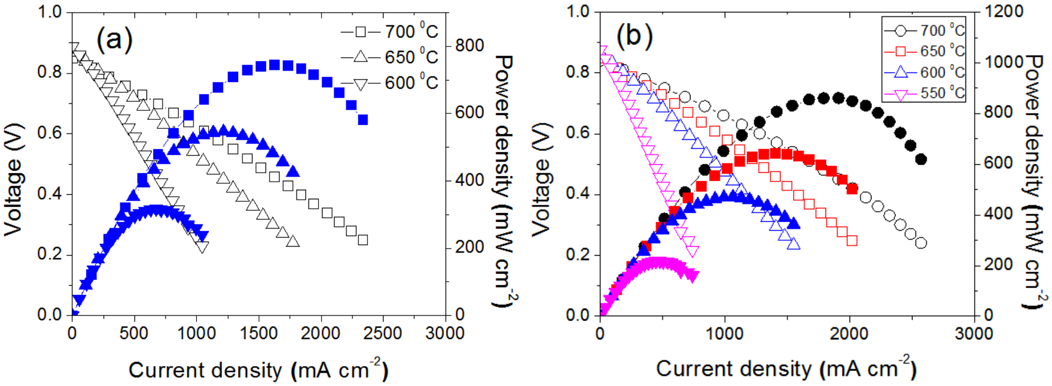

Figure 3. 9 Performance of the as-prepared cells with GBCF and PBFO cathodes with hydrogen at different temperatures.

The *I-V* curve and *I-P* curve of the as-prepared cells with GBCF and GBFO as cathode, respectively, as shown in Fig. 3.9, were obtained in operating temperature range of 550-650 °C, in which humidified H_2 (~3% H_2O) is utilized as a fuel and static ambient air as the oxidant. For GBCF cathode, the P_{max} of the cell were 746, 547 and 315 mW cm^{-2} at 650, 600 and 550 °C, respectively. For GBFO cathode, the P_{max} reached 861, 644, 471 and 218 mW cm^{-2} at 700, 650, 600 and 550 °C, respectively. The cell performances are encouraging and suggest that GBCF and GBFO with partial or full doping of Fe are promising cathode materials for IT-SOFCs.

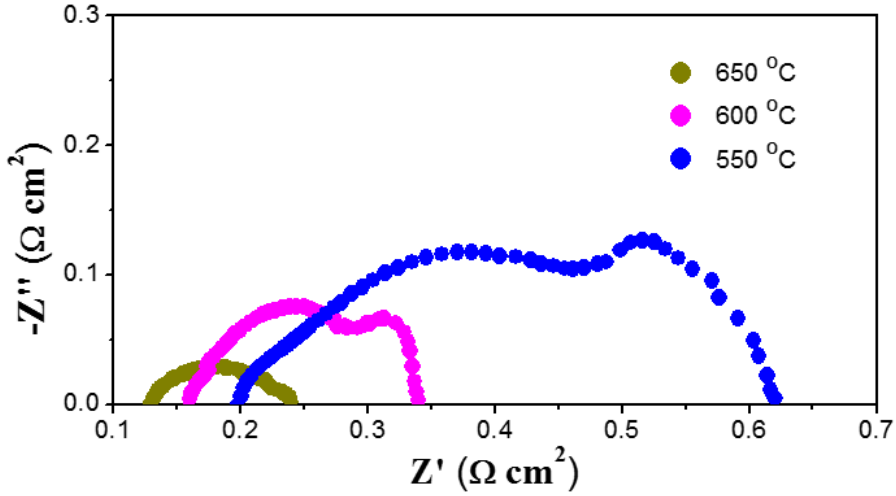

Figure 3. 10 Impedance spectra of the cell Ni-SDC/SDC/GBCF under open circuit conditions from 550 °C to 650 °C.

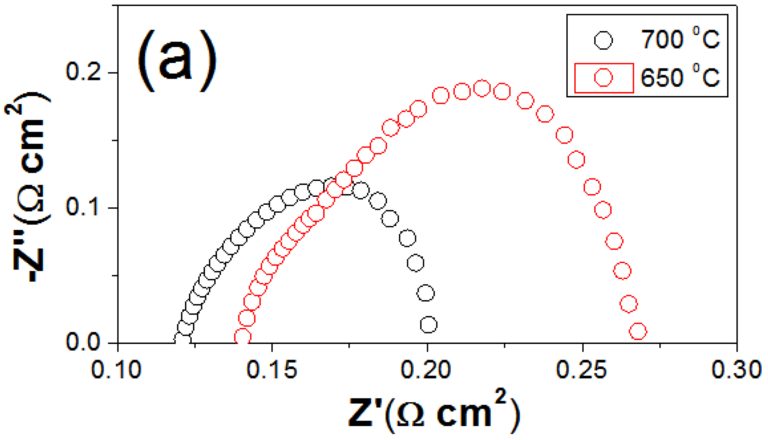

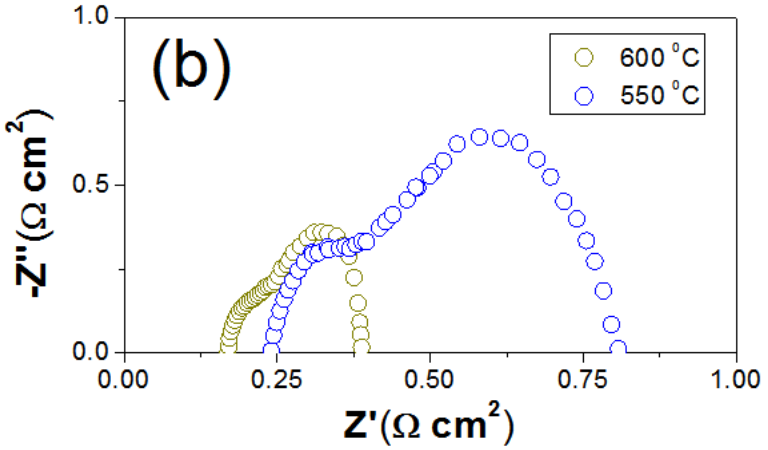

Figure 3. 11 Impedance spectra of the cell Ni-SDC/SDC/GBFO under open circuit conditions from 550 °C to 700 °C.

The electrochemical impedance spectra of single cells with GBCF and GBFO cathodes under open-circuit condition are presented in Fig. 3.10 and Fig. 3.11, respectively. There are two flattening arcs in each of impedance spectra, indicating that at least two electrode processes are involved. The high frequency arc could be attributed to polarization during charge transfer process. The low frequency arc might be attributed to mass transport losses.[118] For GBCF cathode, the increase operating temperature leads to significant reduction of electrode polarization resistance (R_p), typically from 0.42 Ω cm^2 at 550 °C to 0.11 Ω cm^2 at 650 °C, respectively. It is generally recognized that the overall cell polarization loss is dominated by cathode polarization loss.[121] The low R_p values indicated that GBCF cathode exhibited high electrochemical activity for the reduction of molecular oxygen in practical fuel cell system.

The performance observed from experimental results can be understood using the microstructure characteristic of layered perovskite cathodes. It is well known that the ionic conductivity is dependent on both the chemical diffusion coefficient *D* and the surface exchange coefficient *K*. Due to the ordering A-sites in layered perovskite oxide, the rate of the oxygen up-taking is much faster than that in simple ABO_3-type perovskite. Similarly it is also much easier to release oxygen from layered oxides. Taskin has established that the ordering of the A-site sub-lattice in layered structure significantly enhances the oxygen relaxation rate since oxygen atoms can be partially or even completely removed from the Gd^{3+} planes, generating numerous oxygen vacancies in the crystal lattice.[109]

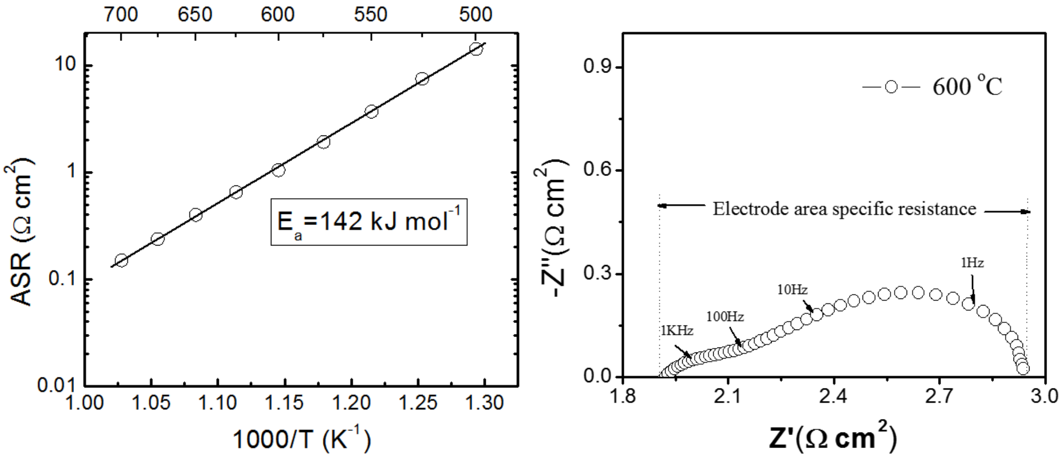

Figure 3. 12 (a) Area-specific-resistance as a function of temperature for a symmetric GBF/SDC/GBFO cell; (b) a typical impedance spectra obtained at 600 °C.

These can be also demonstrated by the ASR values of GBFO to verify the feasibility as a cathode (Fig. 4.12). The ASR was about 0.15 Ωcm^2 at 700 °C and 0.39 Ωcm^2 at 650 °C, respectively. Compared with reported cobalt-free cathodes, *e.g.* $LaBaCuFeO_{5+\delta}$ (0.21 Ωcm^2 at 700 °C)[122] and $Ba_{0.5}Sr_{0.5}Zn_{0.2}Fe_{0.8}O_{3-\delta}$ (0.22 Ωcm^2 at 700 °C),[114] the ASR of GBFO is much lower. This comparison implies that the layered perovskite GBFO cathode has higher activity for oxygen reduction. Furthermore, the ASR of GBFO is also comparable to other cobalt-containing cathodes. For example, $La_{0.6}Sr_{0.4}Co_{0.2}Fe_{0.8}O_{3-\delta}$, a widely used cathode, the ASR was about 0.44 Ωcm^2 at 690 °C on $Ce_{0.9}Gd_{0.1}O_{2-\delta}$ (GDC) electrolyte.[123] The E_a value of GBFO is 142 kJ mol^{-1}, comparable to other E_a values reported in literature,[116] e.g. E_a= 164 kJ/mol for $La_{0.8}Sr_{0.2}CoO_{3-\delta}$, E_a = 183 kJ/mol for $La_{0.8}Sr_{0.2}FeO_{3-\delta}$, and E_a = 202 kJ/mol for $La_{0.8}Sr_{0.2}Co_{0.8}Fe_{0.2}O_{3-\delta}$, respectively. It is obvious that GBFO exhibits promising high activity for oxygen reduction and mobility. This observation is consistent with that reported by Taskin, in which the oxygen diffusion in layered perovskites becomes very fast at relatively low temperature conditions, *e.g.* exceeding 10^{-5} cm^2/s at 600 ^oC for $GdBaCo_2O_{5+\delta}$.[109] In fuel cell, the electrode polarization resistance was 0.57 Ωcm^2 at 550 ^oC, 0.22 Ωcm^2 at 600 ^oC,

3.2.2 SUMMARY

The layered perovskite oxides GBCF and GBFO were investigated as novel cathode for IT-SOFCs. The partial or full substitution of Fe at B site didn't affect the formation of layered perovskite phase. Anode-supported single cells with SDC electrolyte and GBCF and GBFO cathodes were fabricated and evaluated. The maximum output density reached 746 mW cm^{-2} at 650 ^oC. The low interfacial polarization resistance is as low as 0.42, 0.18 and 0.11 Ωcm^2 at 550, 600 and 650 ^oC, respectively. The experimental results indicated that layered perovskite GBCF is a promising layered cathode material for IT-SOFCs. For cobalt-free cathode GBFO, the reasonable electrochemical activity as cathode material is verified from the ASR measurements.

CHAPTER 4

LAYERED PEROVSKITE OXIDES AS CATHODE MATERIALS FOR PROTON CONDUCTING SOFC

Intermediate temperature SOFC (IT-SOFC) could potentially circumvent problems induced by high temperature operating conditions, such as long term stability and durability of material systems.[21] Two technical barriers have to be overcome in order for IT-SOFC performance to be comparable to its high temperature counterpart, e.g., high ohmic resistance of electrolyte and low catalytic activity of electrodes under intermediate temperature conditions (550-750 °C).

Recently, proton conducting membrane fuel cell (PCMFC) has attracted much attention and show great advantages compared with oxide-ion conducting SOFCs, such as low activation energy and high energy efficiency.[124,125] The state-of-the-art proton conducting materials are barium-based perovskite-type ceramics, e.g., $BaCeO_3$ and $BaZrO_3$. By suitable doping, these materials may obtain both adequate proton conductivity as well as sufficient chemical and thermal stability over a wide range of SOFC operating conditions, e.g., $BaZr_{0.1}Ce_{0.7}Y_{0.2}O_{3-\delta}$ (BZCY7).[18] This material can be used as an electrolyte for proton conducting SOFC development.

In a typical proton conducting SOFCs, hydrogen molecules release electrons and are dissociated into protons at anode active layer. The protons then migrate into cathode side through proton conducting electrolyte. At cathode side, oxygen molecules are changed into ions with a supply of external electrons; water molecules are then formed through the combination of protons and ions. Essentially three charge species are involved in cathode electrode, i.e., protons, ions, and electrons. Consequently, cathode electrode development is very critical for high performance proton conducting SOFCs. Furthermore, intermediate temperature operating condition imposes additional challenges on cathode material selections.[34] One of the essential requirements for IT-SOFC cathode material is a high oxygen reduction rate. The reduction reaction is strictly confined to TPB sites. The MIEC may potentially extend TPB active region over the entire cathode.

To the best of our knowledge, the performance of layered perovskite cathodes on BZCY7 electrolyte has not been reported up to date. In this work, PBSC with excellent cell performance in SDC based SOFC has also been investigated in proton conducting SOFC material system under intermediate temperature operating conditions. Furthermore, GBCF and GBFO cathodes formed with partial or full Fe doping at B site of $GdBaCo_2O_{5+\delta}$ layered perovskite were also studied. The lower TEC might potentially decrease the mismatch between cathode and electrolyte in thermal expansion, and thus mitigate the possible interlayer crack or delamination. The button cells were fabricated to evaluate the electrochemical performance with complex impedance technique.

4.1 EXPERIMENTAL

The BZCY7 powders were synthesized using modified Pechini method, where citrate and ethylenediamine tetraacetic acid (EDTA) were employed as parallel complexing agents. Y_2O_3 was first dissolved in nitric acid; the calculated amount of $Ba(NO_3)_2 \cdot 9H_2O$, $Ce(NO_3)_3 \cdot 6H_2O$, and $Zr(NO_3)_4 \cdot 4H_2O$ was dissolved in EDTA-NH_3 aqueous solution. After agitation for a certain time, a proper amount of citric acid was introduced, the molar ratio of EDTA:citric acid:total of metal cations was controlled around 1:1.5:1. After converted into viscous gel under heating and stirring conditions, the solution was ignited to flame and result in ash. The resulting ash-like material was afterwards calcined in air at 1100 ^{o}C for 5 h to form a pure perovskite oxide, and the synthesized BZCY7 powders were then obtained.

The anode-supported BZCY7 bi-layer (Φ=15 mm) was prepared by a dry-pressing method. The mixture of NiO + BZCY7 + starch (60%:40%:20% in weight) was pre-pressed at 200MPa and formed into an anode substrate. A thin anode functional layer (mixture of NiO and BZCY7, 60%:40% in weight) was then pressed onto the substrate at 50 MPa. Then loose BZCY7 powder synthesized above was uniformly distributed onto the anode functional layer, co-pressed at 250 MPa, and subsequently co-sintered at 1400 ^{o}C for 5 h to obtain anode electrode/electrolyte assembly. The thickness of BZCY electrolyte film can be controlled by the weight of used powders. Generally, more loose synthesized powders facilitate the preparation of electrolyte as thin as possible.

Layered PBSC, GBCF and GBFO cathode powders were synthesized using Pechini process with relevant metal nitrates as precursors, followed by calcinations at 1000 ^{o}C for 10 h. The fine powders were then mixed thoroughly with a 6 wt% ethylcellulose-terpineol binder to prepare the cathode slurries which were painted onto BZCY7 electrolyte, respectively, to form single button cells after sintered at 1000 ^{o}C for 3 h in air. The phase identification of the sintered anode–electrolyte bilayer and prepared cathode powders were studied with the powder X-ray diffraction by Cu-Kα radiation (D/Max-gA, Japan).

The single cell was tested from 600 to 700 ^{o}C with humidified hydrogen (~3%

H_2O) as fuel and the static air as oxidant. The flow rate of fuel was about 30 ml/min. The voltage-current curves were recorded by Scribner 890ZV at a 30 mV s^{-1} scan rate. The EIS were obtained using a Solatron 1260 frequency response analyzer in combination with a Solartron 1287 potentiostat over the frequency range from 0.01 Hz to 10^5 Hz under open-circuit conditions. A scanning electron microscope (SEM) was used to observe the microstructure of the post-test cells.

4.2 RESULTS AND DISCUSSION

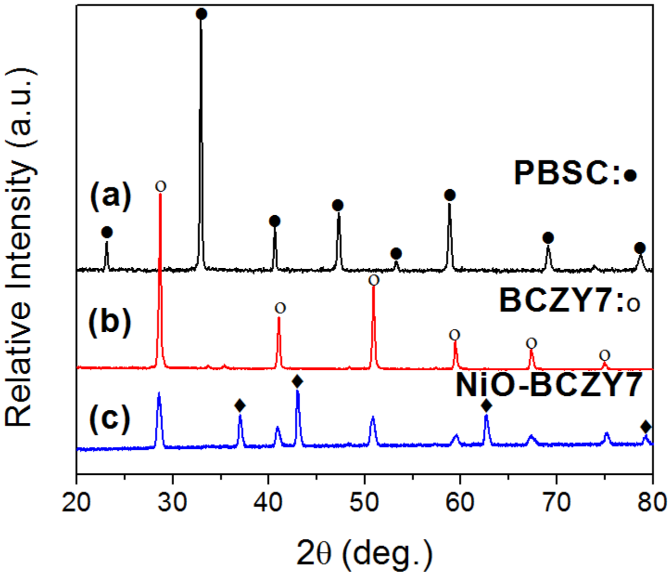

Figure 4. 1 XRD patterns for (a) the layered PBSC perovskite powders, (b) BZCY7 membrane and (c) NiO–BZCY7 anode. Diamond (♦): NiO.

As shown in Fig. 4.1(a), the as-prepared powder of PBSC exhibits a pure layered perovskite phase structure without any peaks attributable to impurities. Fig. 4.1 also presents the XRD spectra of anode/electrolyte bi-layer sintered at 1400 °C for 5 h. It can be clearly seen that there are only peaks corresponding to BZCY7 in electrolyte membrane (Fig. 4.1(b)) and to NiO and BZCY7 in anode substrate (Fig. 4.1(c)). There is no evidence pointing to the formation of any impurities.

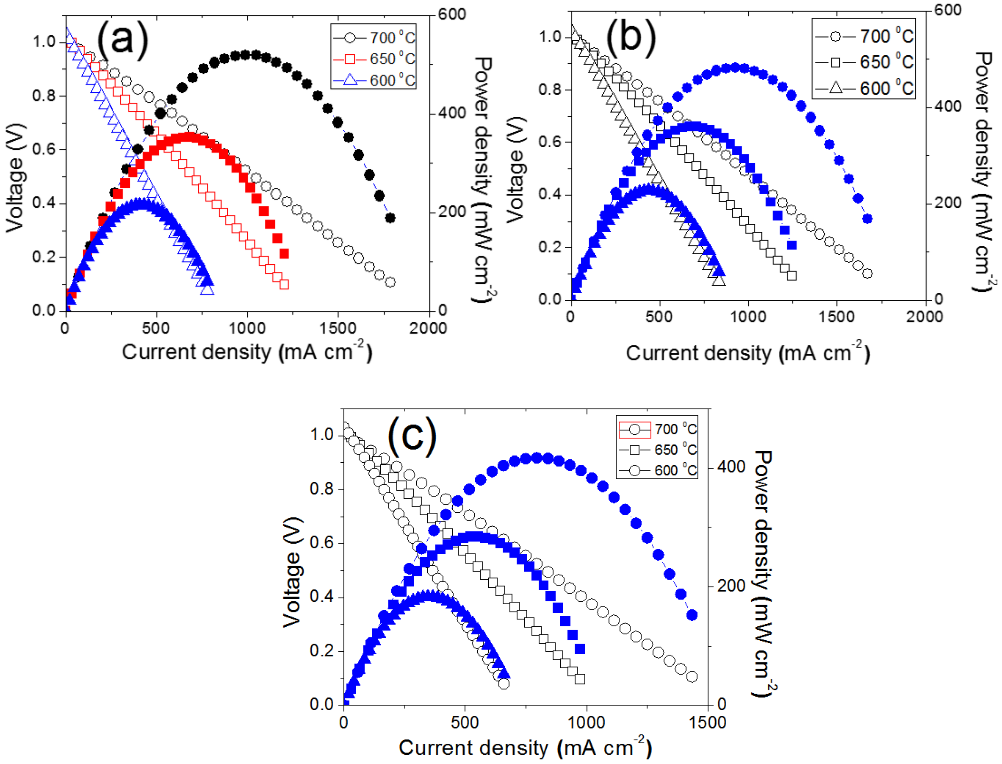

Figure 4. 2 Performance of the as-prepared cell in hydrogen with different cathode materials: (a) PBSC; (B) GBCF; and (c) GBFO.

The electrochemical performance of the as-prepared cells are experimentally obtained and shown in Fig. 4.2 for different cathode materials, including *I*-*V* curve and *I*-*P* curves. In general, the OCV of the cell should be close to its theoretic value of 1.1 V, and is slightly influenced by operating conditions. Since BZCY7 electrolyte is a mix conductor membrane, a slight electron cross flow (current leakage) might exist through the membrane, consequently it leads to that the practical OCV is lower than its theoretical value. The higher the current leakage exists, the lower the cell OCV will be. On the other hand, if the electrolyte membrane is not dense, fuel/gas cross flow might take place, causing lower OCV value as well. For the button cell with PBSC cathode, one can see from Fig. 4.2(a) that peak power densities are 520, 353 and 216 mW cm^{-2} at 700, 650 and

600 ^{o}C, respectively; whereas the high OCV of 1.005 V at 700 ^{o}C, 1.018 V at 650 ^{o}C, 1.03 V at 600 ^{o}C indicate that the electrolyte membrane is sufficiently dense, and the current leakage is negligible. It is worth noting that *I-V* curves are almost linear implying that there is a little activation loss related to the high catalytic activity of PBSC. Since the conductivity of both anode and cathode materials is higher than that of electrolyte in the as-prepared cell, it can be deduced that the voltage drop of the cell is mainly attributed to the *IR* loss across the BZCY7 electrolyte.

In order to evaluate the cathodes with lower TECs, the cell performance of proton conducting single cells with layered perovskites partial or full doped with Fe were also investigated. For GBCF cathode, the peak power density reached 482, 360 and 228 mW cm^{-2} at 700, 650 and 600 ^{o}C, respectively. When B site is fully doped, GBFO still showed reasonable power output at the same operation temperatures (417, 286 and 183 mW cm^{-2} at 700, 650 and 600 ^{o}C, respectively). Compared with the performance of PBSC, we can see that the partial doping of Fe didn't decrease the catalytic activity or cathode performance that much in basis of the similar electrolyte thickness and electrode/electrolyte interface, which can be also identified from the impedance spectra.

The impedance spectra of the as-prepared cells with different layered perovskites are obtained under open-circuit conditions at various operating temperatures, as shown in Fig. 4.3. The impedance spectra consisted of two arcs at 600 ^{o}C, which indicate that there are at least two electrode processes during oxygen molecule reduction. The high frequency arc could be attributed to the polarization during charge transfer process. The low frequency arc could be attributed to the oxygen adsorption and desorption on the cathode surface as well as the diffusion of the oxygen ions.[118]

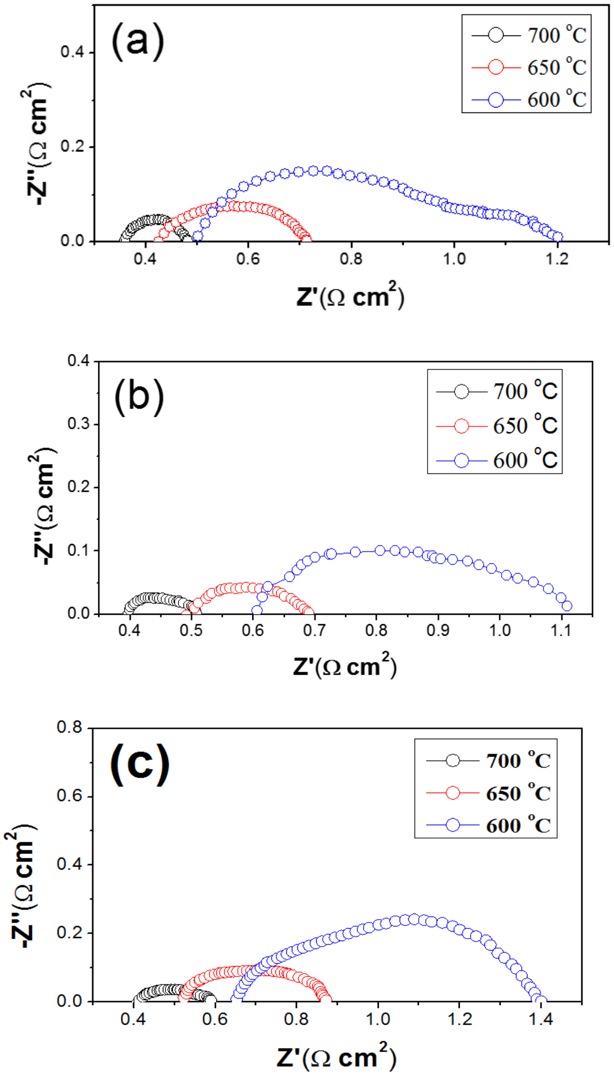

Figure 4. 3 Impedance spectra measured under open-circuit condition for cells with different cathode materials: (a) PBSC; (b) GBCF; and (c) GBFO.

The impedance spectra of the as-prepared cells with different layered perovskites are obtained under open-circuit conditions at various operating temperatures, as shown in Fig. 4.3. The impedance spectra consisted of two arcs at 600 ^{o}C, which indicate that there are at least two electrode processes during oxygen molecule reduction. The high frequency arc could be attributed to the polarization during charge transfer process. The low frequency arc could be attributed to the oxygen adsorption and desorption on the cathode surface as well as the diffusion of the oxygen ions.[118] When operating temperature increases to 650 °C and 700 °C, low frequency arc disappears, implying that the resistance of oxygen diffusion in porous electrode can be neglected at relative high temperatures. Specifically for PBSC cathode, as one can see, increase operating temperature may lead to significant reduction of interfacial polarization resistance R_p, typically from 0.69 Ωcm^2 at 600 °C to 0.12 Ωcm^2 at 700 °C, respectively. Compared with proton-conducting single cells with the same anode and electrolyte but $PrBaCo_2O_{5+\delta}$ cathode, the R_p values of PBSC are lower at the same temperatures (1.2 and 0.14 Ωcm^2 at 600 and 700 °C).[126] With Fe doping at B-site based on $GdBaCo_2O_{5+\delta}$, GBCF also showed reasonable activity in oxygen reduction. It can be seen that increase operating temperatures result in significant reduction of interfacial polarization resistance R_p, typically from 0.5 Ωcm^2 at 600 °C to 0.11 Ωcm^2 at 700 °C, respectively. The results indicated that layered GBCF cathode has considerable catalytic activity for operation at intermediate temperature range. For GBFO with further Fe doping, R_p was 0.75 Ωcm^2 at 600 °C, 0.35 Ωcm^2 at 650 °C and 0.2 Ωcm^2 at 700 °C, respectively. It is worth noting that the R_p values of GBFO are well comparable to cobalt-containing cathodes with the same anode and electrolyte, such as $GdBaCo_2O_{5+\delta}$ (0.16 Ωcm^2 at 700 °C),[127] $PrBaCo_2O_{5+\delta}$ (0.15 Ωcm^2 at 700 °C).[111]

The experimental results of the proton conducting SOFCs with PBSC, GBCF and cobalt-free GBFO cathodes can be understood using the microstructure characteristic of layered perovskite cathode. It is well known that the ionic conductivity is dependent on both the chemical diffusion coefficient D and the surface exchange coefficient K. Due to the ordering A-sites in the layered perovskite oxides, the rate of the oxygen up-taking is much faster than that in simple ABO_3-type perovskite. Similarly it is also much easier to release oxygen from layered oxides. The ordering of the A-site sub-lattice in layered structure significantly enhances the oxygen relaxation rate since oxygen atoms can be partially or even completely removed from the Ln^{3+} planes, generating numerous oxygen vacancies in the crystal lattice.

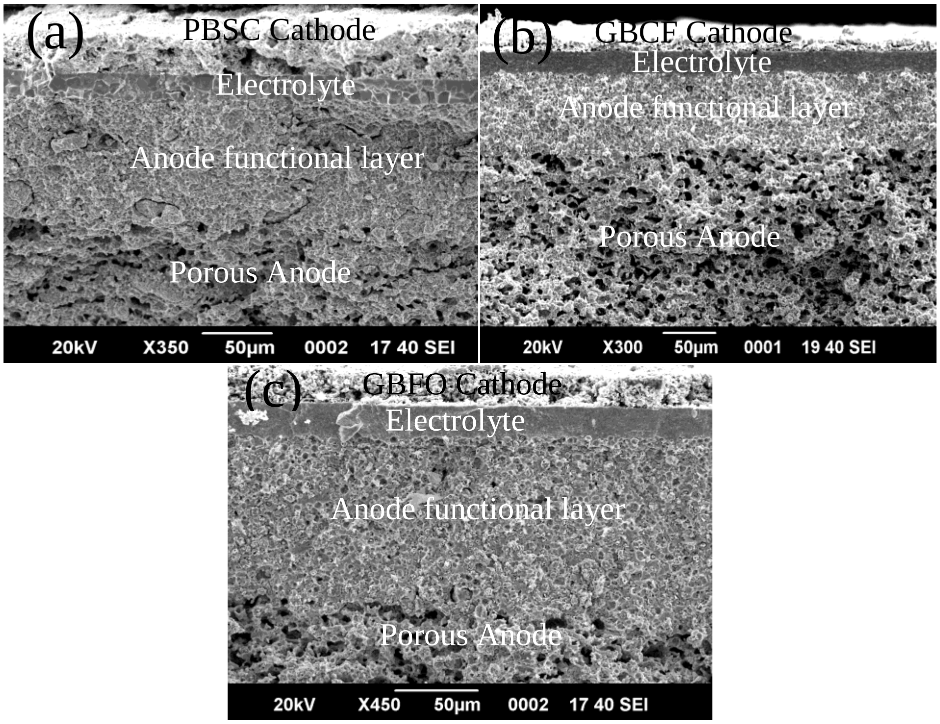

Figure 4. 4 SEM micrographs of cell after testing: the cross-section of tri-layer cell with a 20 μm-thick BZCY7 electrolyte membrane and porous cathode layer: (a) PBSC; (b) GBCF; and (c) GBFO.

One can see from Fig. 4.4 that the BZCY7 electrolyte membrane is completely dense, and there are no pores or cracks. The uniform holes in porous anode layer after completely reduced at H_2 atmosphere is due to the well mixed NiO, BZCY7 and starch. The anode functional layer between anode support layer and electrolyte layer is used to avoid the possible formation of macro-pores at electrode/electrolyte interface; otherwise, the ohmic resistance at the interface will increase. From the cross-section view of tri-layer cell, the thickness of fabricated BZCY7 membrane is only about 20 μm. The electrolyte film adheres to the layers of functional anode and cathode fairly well.

4.3 CONCLUSIONS

The novel PCMFCs are fabricated with thin $BaZr_{0.1}Ce_{0.7}Y_{0.2}O_{3-\delta}$ (BZCY7) as electrolyte and layered perovskite oxides of PBSC, GBCF and GBFO as cathode, respectively. The performance of the lab-scale tri-layer cells are tested and characterized under intermediate temperature range from 600 to 700 ^{o}C. For PBSC cathode, the open-circuit potential of 1.005 V and maximum power density of 520 mW cm^{-2} are achieved at 700 ^{o}C. With temperature increases, the total cell resistance decreases, among which electrolyte resistance becomes increasingly dominant over polarization resistance. The results indicate that PBSC perovskite cathode is a good candidate for intermediate temperature PCMFC development, while the developed Ni-BZCY7|BZCY7|PBSC is a promising functional material system for SOFCs. When the B-site is doped with Fe, the cell performance can still exhibit maximum power density of 482 mW cm^{-2} with polarization resistance of the electrodes of 0.11 Ωcm^{2} at 700 ^{o}C. For cobalt-free cathode of GBFO with full Fe doping, the results show that the open-circuit potential of 1.007 V and maximum power density of 417 mW cm^{-2} are achieved at 700 ^{o}C. The polarization resistance of the electrodes was 0.18 Ωcm^{2} at 700 ^{o}C. Therefore, the layered perovskite oxides are very promising to be employed as cathode materials for PCMFC while the proper doping of Fe at B-site can compromise the cathode activity and TEC to select an optimized candidate for SOFC with long stability.

CHAPTER 5

A CERAMIC-ANODE SUPPORTED LOW TEMPERATURE SOLID OXIDE FUEL CELL

The carbon deposition and sulfur poisoning are two major obstacles for hydrocarbon fueled SOFCs with nickel cermet anode.[11,128] In addition, the nickel based anodes also suffer from the volume instability induced by redox cycling[129] as well as nickel particle agglomerations due to high temperature and long-term operations.[130] To overcome these issues, nickel-free metal oxide anode materials have been investigated, such as $La_{0.75}Sr_{0.25}Cr_{0.5}Mn_{0.5}O_{3-\delta}$ (LSCM),[131] $Sr_2Mg_{1-x}Mn_xMoO_{6-\delta}$ (x=0 to 1),[132] and doped $(La,Sr)(Ti)O_3$.[133,134] Experimental results have demonstrated that such anode materials are effective in inhibiting carbon deposition or sulfur poisoning.[135-137]

So far the cell designs are exclusively electrolyte-supported when metal oxide anodes are employed. This design requires relatively thick electrolyte of 300~500 μm to support the entire cell, leading to significant ohmic resistance. Accordingly, high temperatures (800-900 ^{o}C) are needed to reduce the ohmic loss for high power outputs. The high operating temperatures in turn could lead to a variety of degradations. Anode-supported designs may effectively reduce the ohmic loss with thin electrolyte membrane while lowering the operating temperatures, which have been well demonstrated with nickel cermet anode. However, the anode-supported designs with metal oxides as anode materials are difficult to fabricate. In general, high sintering temperature is needed to co-fire the anode substrate/electrolyte assembly to densify the thin electrolyte, which in turn may induce the densification of the porous anode substrate, resulting in anode porosity loss. Another issue is that the existing oxide anode materials cannot provide adequate conductivity for current collection in thick anode substrate.

Here we report the development of anode-supported intermediate temperature (550-700°C) SOFC with metal oxide LSCM as the supporting substrate, SDC as the electrolyte, and PBSC as the cathode. With a slight amount of CuO mixed with LSCM, the anode substrate/electrolyte assembly was co-fired at low temperature of 1250 °C. The dense thin SDC electrolyte (20 μm) was obtained while the sufficient porosity of anode substrate (400 μm) was maintained. The CuO nano-particles were impregnated into the porous substrate to enhance current collecting effect of thick anode. The cell exhibited the volumetric power density of 596 mW cm^{-2} and 381 mW cm^{-2} at 700 °C with wet hydrogen and methane as the fuel respectively, where the silver paste was used as current collector, the highest performance up to date for the cells with metal oxide anodes at this temperature.

5.1 EXPERIMENTAL

The LSCM powders were synthesized by modified Pechini method. Briefly citrate and ethylenediamine tetraacetic acid (EDTA) were employed as parallel complexing agents. La_2O_3 was calcined at 1000 °C for 5 h to remove the humid water, and then dissolved in nitric acid. The stoichiometric amounts of $Sr(NO_3)_2$ (99.99%), $Cr(NO_3)_3 \cdot 9H_2O$ (99.99%) and $Mn(CH_3COO)_2 \cdot 4H_2O$ (99.99%) were dissolved in EDTA-NH_3 aqueous solution. After agitation for a certain period of time, a proper amount of citric acid was introduced, the molar ratio of EDTA : citric acid : total of metal cations was controlled around 1:1.5:1. After converted into viscous gel under heating and stirring conditions, the solution was ignited to flame and result in ash. The resulting ash-like material was afterwards calcined in air at 1200 ^{o}C for 5 h to obtain LSCM powders. The SDC and PBSC powders were synthesized using the same method.

Rectangular bar specimens (50mm×5mm×1.8mm) of SDC-LSCM were uniaxially pressed at 360MPa and sintered at 1250 ^{o}C for 5 h in air. The obtained porous bar was infiltrated by copper nitrate solution and fired at 600 ^{o}C for 30 min with heating and cooling rate of 10 ^{o}C min^{-1} to decompose nitrate. The electrical conductivities of SDC-LSCM with and without Cu infiltration were studied from 400 ^{o}C to 800 ^{o}C in 5%H_2/95%Ar by a standard DC four-probe technique on a multimeter (Agilent, 34401A). The LSCM-SDC/SDC bi-layer cells (Φ=15 mm) were prepared by dry-pressing/co-firing method. The mixture of CuO + LSCM + SDC + starch, with the ratio of CuO:LSCM:SDC:starch=1:12:8:6 in weight, was pre-pressed at 200 MPa to form an anode substrate. Then loose SDC powder was uniformly distributed onto the anode substrate, co-pressed at 250 MPa and sintered subsequently at 1250 ^{o}C for 6 h to densify the SDC membrane. The cell Cu-SDC/SDC was fabricated by the same method and sintered at 1100 ^{o}C for 2 h. The Cu was then infiltrated into the porous anode substrate. Briefly, the nitrate solution was prepared by dissolving $Cu(NO_3)_2 \cdot 2.5H_2O$ in distilled water. The solution was dropped onto the substrate surface and infiltrated into the porous anode. After drying, the samples were fired at 600 ^{o}C for 30 min with heating and cooling rate of 10 ^{o}C min^{-1} to decompose nitrate. The final CuO loading was about 20.3 wt% of total anode substrate after 4 infiltration-heating cycles. The cathode slurry was prepared by mixing PBSC powders with a 6 wt% ethylcellulose-terpineol binder. The slurry was then painted on SDC electrolyte, and sintered at 1000 ^{o}C for 3 h in air to form single cells of Cu-LSCM-SDC/SDC/PBSC. The silver paste was then painted on the anode and cathode respectively and dried as current collector.

The cells with Cu-SDC-LSCM and Cu-SDC anodes were tested from 550 to 700 ^{o}C with humidified hydrogen and methane (~3% H_2O) as fuels respectively and the static air as the oxidant. The flow rate of the fuel was controlled at 40 ml/min by a mass flow meter (APEX). The voltage-current curves were recorded by Scribner 890ZV at a scanning rate of 50 mV s^{-1}. The EIS were obtained using a Solatron 1260 frequency response analyzer in combination with a Solartron 1287 potentiostat over the frequency range from 0.1 Hz to 10^5 Hz under open-circuit conditions. A scanning electron microscope (SEM, Zeiss Plus) was used to observe the microstructure of the cells. The porosity of anode was measured using mercury porosimeter (AutoPore IV).

5.2 RESULTS AND DISCUSSION

Figure 5.1 shows the SEM images of the fabricated LSCM-anode supported single cell. Apparently SDC electrolyte was dense while keeping sufficient porosity of substrate (35.05%). And the average grain size of SDC electrolyte was about 10 μm, far bigger than those of NiO-SDC/SDC cells co-sintered at 1400 ^{o}C.[26,138,139] It is anticipated that the large grain size may reduce the resistance induced by grain boundaries and improve the conductivity of the electrolyte. The CuO plays an important role in lower temperature (1250 ^{o}C) co-firing while achieving high quality sintering results.[140] As a comparison, the substrate/electrolyte assembly without addition of CuO was also co-sintered at the same temperature of 1250 ^{o}C. The corresponding SEM is shown in Figure

5.1(b). Obviously, the electrolyte membrane was not dense and a large portion of porosity exists. The growth of SDC grains was also severely inhibited.

The thick anode substrate of oxide LSCM may lead to inadequate conductivity particularly at lower operating temperature conditions, therefore metal Cu was introduced into porous anode substrate by ion-impregnation method to improve the current collecting effect. Figure 5.1 (c) and (d) show porous anode substrate impregnated with Cu, where the nano-sized fine copper particles form a highly interconnected network structure, providing continuous electron-conducting paths.

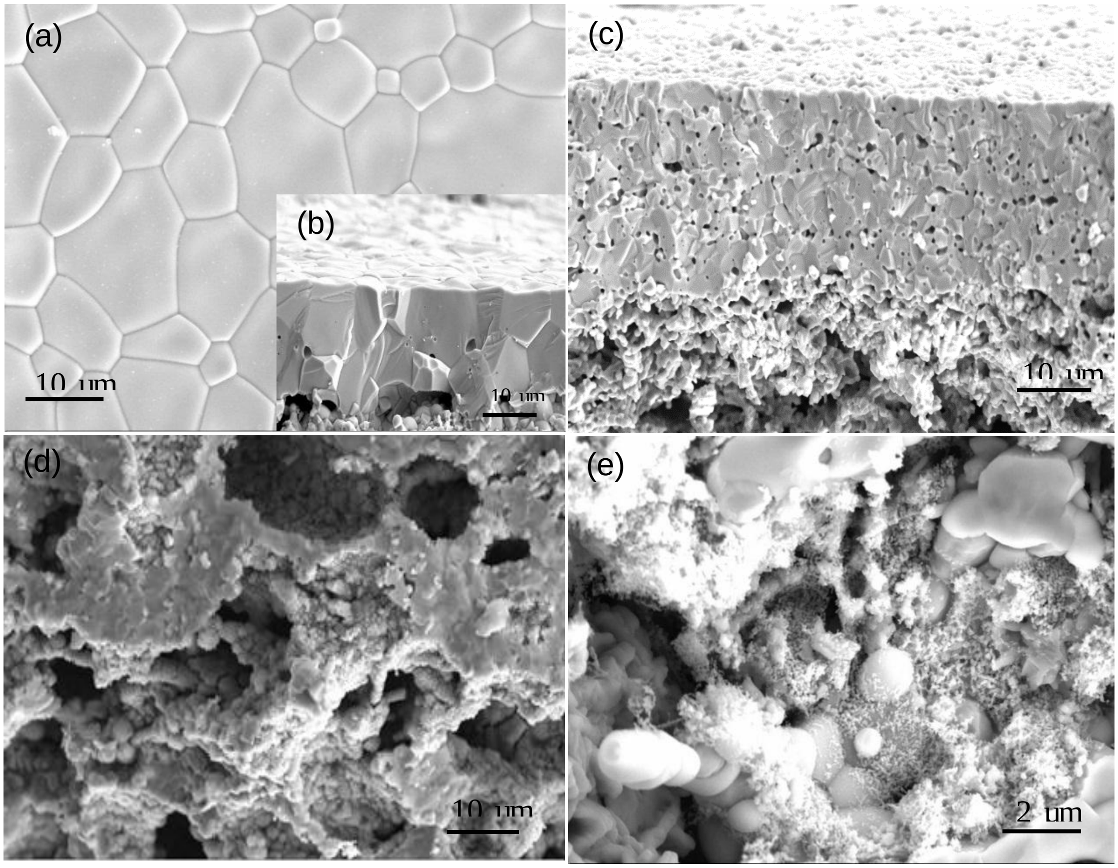

Figure 5. 1 SEM images of cell after sintering: (a) the surface of electrolyte; (b) the cross-section of cell with a 20 μm thick SDC membrane; (c) the cross-section of cell without CuO sintering additive; (d) the porous anode morphology after ion-impregnation; (e) the Cu nanoparticles coating on LSCM-SDC surfaces.

Figure 5.2 shows the polarization and power density curves of the cell with infiltrated anode at the temperatures of 550-700 °C. The humidified hydrogen (~3% H_2O) and ambient air were used as the fuel and the oxidant respectively. The OCV at 550, 600, 650 and 700 °C was 0.9, 0.88, 0.86 and 0.85 V respectively, indicating that the electrolyte is sufficient dense. Due to the partial reduction of Ce^{4+} to Ce^{3+} in SDC when exposed to a low oxygen partial pressure (1×10^{-19} atm) and temperature (>600 °C), a slight electronic current leakage might exist.[141] However, the OCVs observed from this experiment are slightly higher than those reported in literature[119] and are in good agreement with microstructure images in Figure 5.1.

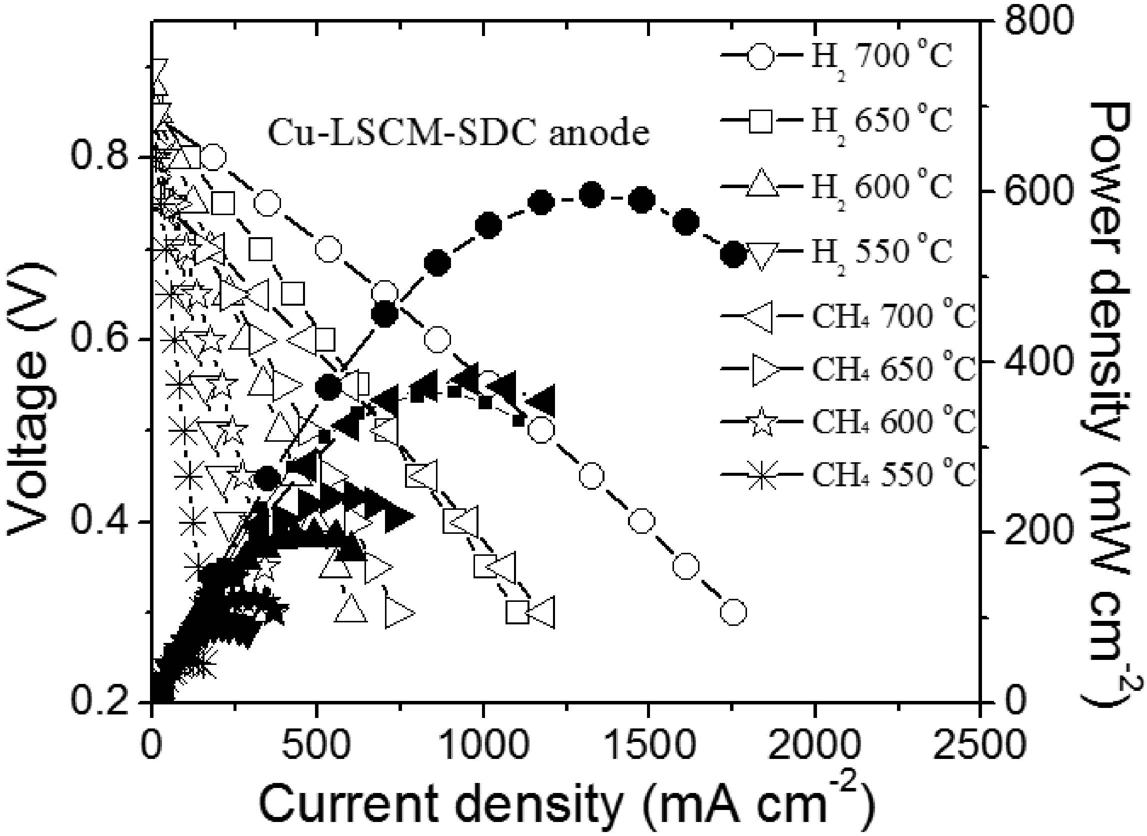

Figure 5. 2 Cell voltage and power density as a function of current density for the cell Cu-LSCM-SDC/SDC/PBSC. and (b) Cu-SDC/SDC/PBSC with H_2 and CH_4 as fuel, respectively; (c) The conductivities of LSCM-SDC and Cu infiltrated LSCM-SDC anode in 5%H_2/95%Ar.

The maximum power density was 596, 365, 196 and 94 mW cm^{-2} at 700, 650, 600 and 550 °C, respectively. With wet CH_4 as the fuel, the maximum power density reached 381 mW cm^{-2} at 700 °C. In the 300 μm-thick YSZ electrolyte-supported cell with pure LSCM as the anode,[131] the cell exhibited the peak power densities of 470 mW cm^{-2} in wet H_2 and 200 mW cm^{-2} in CH_4 at 900 °C, respectively. In a recent study, a 300 μm-thick $La_{0.8}Sr_{0.2}Ga_{0.83}Mg_{0.17}O_3$ (LSGM) electrolyte-supported cell with double perovskite Sr_2MgMoO_6 anode showed the peak power density of 438 mW cm^{-2} at 800 °C in CH_4.[132] The cell performance reported in this study is very encouraging because the cell obtained high performance in relatively low temperatures.

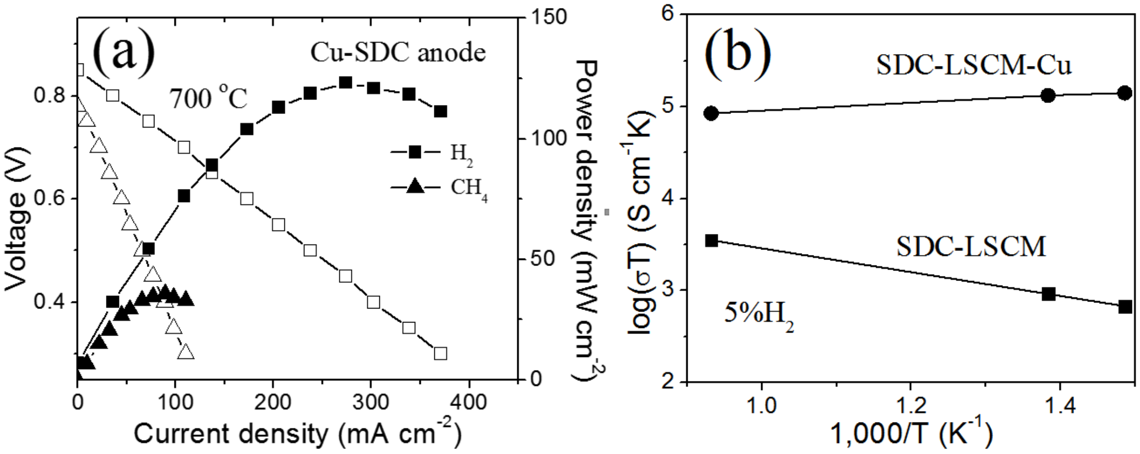

Figure 5. 3 (a) Cell voltage and power density as a function of current density for the cell Cu-SDC/SDC/PBSC with H_2 and CH_4 as fuel, respectively; (b) the conductivities of LSCM-SDC and Cu infiltrated LSCM-SDC anode in 5%H_2/95%Ar.

Figure 5.3(a) shows the performance of cell Cu-SDC/SDC without LSCM. At 700 °C, the maximum power density was 123 mW cm^{-2} in H_2 and 36 mW cm^{-2} in CH_4 which was much lower than that of the cell with LSCM. The results indicate Cu has poor catalytic ability and LSCM with mixed conductivity play an important role in catalysis after decorated by infiltrating Cu at LSCM surfaces. The conductivities of LSCM-SDC with and without Cu infiltration in 5%H_2/95%Ar were shown in Figure 3(b). As we can see, LSCM-SDC exhibited only 1 S/cm at 400 ^oC and 3.28 S/cm at 800 ^oC. After infiltration, conductivity of Cu-LSCM-SDC was improved to 210 S/cm at 400 ^oC and 79 S/cm at 800 ^oC.

To evaluate the performance of the thin electrolyte and Cu-impregnated anode in the whole fuel cell, the impedance spectra of the as-prepared cell were measured under open-circuit conditions with wet hydrogen and CH_4 as fuels at different temperatures. The results are shown in Figure 5.4 and 5.5.

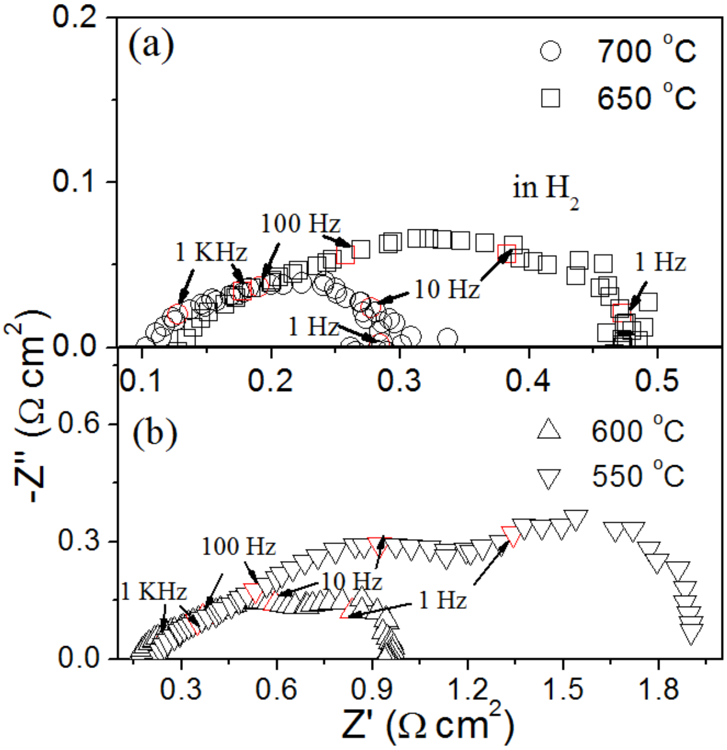

Figure 5. 4 Impedance spectra measured under open-circuit conditions at different temperatures with H_2 as fuel.

In these spectra, the low frequency intercept represents total resistance(R_t) of the cell; the high frequency intercept is total ohmic resistance (R_o) contributed mainly by the electrolyte; the difference between R_t and R_o corresponds to electrode polarization resistance (R_p), including the contributions from both the anode and cathode.[29]

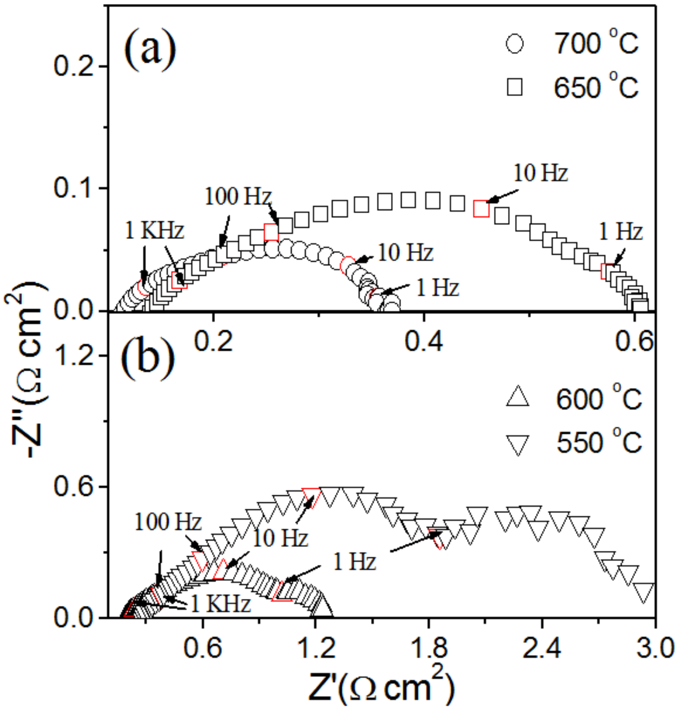

Figure 5. 5 Impedance spectra measured under open-circuit conditions at different temperatures with CH_4 as fuel.

As shown in Figure 5.4, the electrolyte resistance was only 0.23, 0.16, 0.12 and 0.1 Ω cm^2 at 550, 600, 650 and 700 °C, respectively. By contrast, the LSGM electrolyte-supported cell (~300 μm in thickness) showed the ohmic resistance of 0.78 Ω cm^2 at 700 °C.[142] The cell ohmic resistance didn't show apparent changes when the fuel was switched to the methane (Figure 5.5). Obviously the application of thin film electrolyte in anode-supported cells resulted in a significant reduction of ohmic resistance. With H_2 as the fuel, the total polarization resistance R_p was 1.67, 0.79, 0.37 and 0.2 Ω cm^2 at 550, 600, 650 and 700 °C, respectively. With CH_4 as the fuel, the R_p value increased to 0.28 Ω cm^2 at 700 °C. As a comparison, the polarization resistance of anode with pure LSCM was 0.26 Ω cm^2 in wet H_2 and 0.87 Ω cm^2 in wet CH_4 at 900 °C, respectively.[131] It is worth mentioning that the anode polarization resistance was measured using a three-electrode configuration in the latter case. Considering that the polarization resistance contributed from the cathode was also included in our measurement results, the actual polarization resistance of the anode will be even lower than those values mentioned above. These results indicate that the LSCM anode impregnated with Cu may effectively improve the anode polarization performance even though the thick LSCM substrate was used.

5.3 SUMMARY

In this study, we first examined the feasibility of ceramic LSCM anode supported SOFC fabrication. With a slight amount of CuO addition to the substrate, the dense electrolyte SDC and anode substrate LSCM with sufficient porosity were obtained by co-sintering LSCM/SDC assembly at low temperature1250 °C. Second, by infiltrating CuO nano-particle into porous substrate, current collection was improved for the ceramic anode LSCM. As a result, we can fabricate anode-LSCM-supported SOFCs at low sintering temperature with high volumetric power density of 596 mW cm^{-2} and 381 mW cm^{-2} at 700 °C with wet hydrogen and methane as the fuel respectively, the highest performance up to date for the cells with metal oxide anodes at this temperature.

CHAPTER 6

A PLATINUM NANOWIRE NETWORK AS HIGHLY EFFICIENT CURRENT COLLECTOR FOR INTERMEDIATE TEMPERATURE SOLID OXIDE FUEL CELLS

To improve the durability and reduce the cost of solid oxide fuel cells (SOFCs), significant efforts have been put into lowering the operating temperature of SOFCs to intermediate range of (400–600 °C).[8,12,21,22,132,143,144] However, the high ohmic resistance loss in the electrolyte and high polarization resistance loss in the cathode are two key obstacles toward the development of high performance intermediate temperature SOFCs.[27,30,38] The high ohmic resistance can be overcome through the development of thin film electrolyte built upon the anode-supported SOFC designs.[145-147] The high polarization resistance loss in the cathode can be reduced by developing high performance cathode materials. $La_{1-x}Sr_xMnO_3$ (LSM) has been widely used as the cathode material at early stages in the development of SOFCs.[78,106,148] Since the LSM is an electronic conductor, the composite cathodes formed by mixing the LSM with electrolyte materials such as yttria-stabilized zirconia (YSZ) then are developed to improve the ionic conductivity and ORR sites of the cathodes.[74] Later on, the MIEC cathode materials such as $La_{0.6}Sr_{0.4}Co_{0.2}Fe_{0.8}O_{3-\delta}$ (LSCF)[123, 149] and $Ba_{0.5}Sr_{0.5}Co_{0.8}Fe_{0.2}O_{3-\delta}$ (BSCF)[52] are developed so that the same material can conduct both electrons and ions simultaneously. As a result, the ORR sites can be extended to the entire surface of porous cathode. In recent years, the layered perovskites such as PBCO are investigated as the promising intermediate temperature cathode materials.[99,100,111] The high performance cathode may also be achieved with microstructure innovations via infiltration techniques.[103,150]

Although many cathode materials mentioned above have been extensively studied, the conductivity of these materials is usually on the order of 10^2 S/cm, which is low in conducting electrons between the ORR sites and external circuit. To compensate for the low conductivities of cathode oxides, the current collector is typically employed in SOFCs.[151] Consequently the electrons needed by ORR can be transported from the external circuit to the reaction sites with minimum ohmic loss. Despite of the significant importance, the designs of current collectors do not receive too much attention in open literatures. Usually the platinum ink or platinum paste is simply painted on the cathode surface. After sintering, the organic substance is burn out while the platinum is attached to the cathode surface.[152] In order to reduce the polarization resistance, the cathode should have high conductivity and catalytic activity as well as be porous enough to allow oxygen readily to diffuse to the ORR sites.[153] If too much platinum is painted on the cathode surface, it might block the surface open pores, increasing the resistance of oxygen diffusion. Conversely the current collector with less platinum may avoid blocking the surface open pores of cathode porous structure; it can only connect less ORR sites to the external circuit. In this situation, the ORR sites, not directly connected to the current collector, have to conduct electrons through the cathode oxide. Accordingly the ohmic resistance increases. The ideal current collector should directly connect the ORR sites while leaving the open pores unblocked as much as it can. Obviously these two objectives are competing or conflicting with each other. It is difficult for traditional preparation methods of current collectors to achieve these two goals simultaneously.

Herein we report the fabrication and evaluation of a nano-scale current collector for intermediate temperature SOFC cathodes. A spray process is employed to coat the ink of carbon-black supported platinum nanoparticles on the cathode surface. After firing, the platinum nanowire-network is formed on the surface of the cathode, which can connect the ORR sites at the nano-scale to the external circuit while being able to substantially avoid blocking the open pores of the cathode. The experimental results have successfully demonstrated that such a platinum current collector is able to significantly reduce the cathode polarization resistance and improve SOFC performance. The stability of the current collector is also examined under large current discharge conditions for 400 hours. The developed method can be readily scaled up for mass productions.

6.1 EXPERIMENTAL

Charaterizations of platinum coated carbon black: The initial combustion temperature, the weight loss regime and exothermic behavior of the commercial platinum loaded carbon black powders (Alfa Aesar) were examined using thermo-gravimetric analysis /differential scanning calorimetry (TGA-DSC, NETZSCH STA) in air between room temperature and 1030 ^{o}C with a heating rate of 10 ^{o}C min^{-1}. The micro-morphology and microstructure of the carbon black supported platinum powders, button cells, and current collectors were observed using transmission electron microscope (TEM, Hitachi H-8000) and field-emission scanning electron microscope (FESEM, Zeiss ultra plus), respectively.

Preparation and polarization measurement of symmetric cells: The citrate and ethylenediaminetetraacetic acid (EDTA) combustion method was used to synthesize the PBCO cathode and SDC electrolyte powders. The details were described in the separate paper.[10] The SDC pellets formed by the dry-pressing method were sintered at 1400 ^{o}C for 5 h to form dense SDC electrolyte with the thickness of 240 μm and the diameter of 12 mm. The pellets were then polished with sand paper. The fine PBCO powders were mixed thoroughly with a 6 wt% ethylcellulose-terpineol binder to form the slurry. The slurry was painted on both sides of the SDC pellets, which were subsequently sintered at 1000 ^{o}C in air for 3 h.The platinum coated carbon black powders were dispersed into the ethanol solvent, which was then ultrasonically vibrated for 2 h to form the well-dispersed ink. The platinum coated carbon black ink was sprayed on the cathode surface with an ejecting gun to form symmetric cells. The ink load was controlled by the spraying time. The EIS in air at different temperatures were measured using a Solatron 1260 frequency response analyzer in combination with a Solartron 1287 potentiostat over the frequency range from 0.01 Hz to 10^{5} Hz.

Fuel cell fabrication and test: The anode-supported anode-electrolyte assembly was prepared by a simple dry-pressing/co-firing method. The powder mixture of NiO + SDC + starch (60%:40%:20% in weight) was first pre-pressed at 200 MPa as an anodesubstrate. Then the loose SDC powder was uniformly distributed onto the anode substrate, co-pressed at 250 MPa and sintered subsequently at 1350 ^{o}C for 5 h to densify the SDC membrane (~ 8 μm).The cathode slurry was then painted on SDC electrolyte film and sintered at 950 ^{o}C for 3 h in air to form the single cell of NiO-SDC/SDC/PBCO. The corresponding thicknesses of the resulting anode/electrolyte/cathode assembly are ~760 μm/~8 μm/~20 μm respectively. The platinum coated carbon black ink was sprayed on the cathode surface as the current collector. As a comparison, the conventional current collector was also prepared by painting the Pt paste on the cathode surface and sintered at

1000^{o}C for 1 hour to burn out the organic solvent. Further the two most widely used perovskite cathode materials $Ba_{0.5}Sr_{0.5}Co_{0.2}Fe_{0.8}O_{3-\delta}$ (BSCF) and $La_{0.6}Sr_{0.4}Co_{0.2}Fe_{0.8}O_{3-\delta}$ (LSCF) were also employed to fabricate the anode-supported cells NiO-SDC/SDC/BSCF and NiO-SDC/SDC/LSCF. The platinum nanowire current collectors and conventional Pt paste collectors were also applied for the cells respectively. The button cells were tested under the temperatures of 500-650 ^{o}C. The humid hydrogen (~3% H_2O) was used as the fuel while the static air was used as the oxidant. The flow rate of the fuel was controlled at 30 ml min^{-1} using a precision flow meter (APEX). The current-voltage curves were recorded by Scribner 890ZV at the scanning rate of 30 mV s^{-1} and the EIS were measured in open-circuit condition over the frequency range of 0.01 Hz to 10^5 Hz.

6.2 RESULTS AND DISCUSSION

The transmission electron microscopy (TEM) image of Fig. 6.1a shows that the platinum nanoparticles are uniformly coated on the surface of the carbon black. The thermo gravimetric analysis (TGA) shows a significant weight loss of the platinum coated carbon black powders between 330 ^{o}C and 550 ^{o}C (Fig. 6.2), indicating that the carbon black was oxidized and became into carbon dioxide gas. The differential scanning calorimetry (DSC) indicates significant heat release because of carbon black oxidation. It is reasonable to believe that the platinum coated carbon black sprayed on the cathode should have the similar behavior during the heating up process in the furnace. The release of heat from the test furnace together with local exothermicity from the carbon black oxidation promoted the platinum nano-particles to agglomerate and connect with one another, forming the tree-branch-like nano-wire network as observed from field-emission scanning electron microscopy (FESEM) in Fig. 1b. The diameter of the nano-wires ranges from about 100 nm to 400 nm (Fig. 1c and 1d). Obviously such a nanowire network current collector is able to directly connect the ORR sites to the external circuit using its network branches.

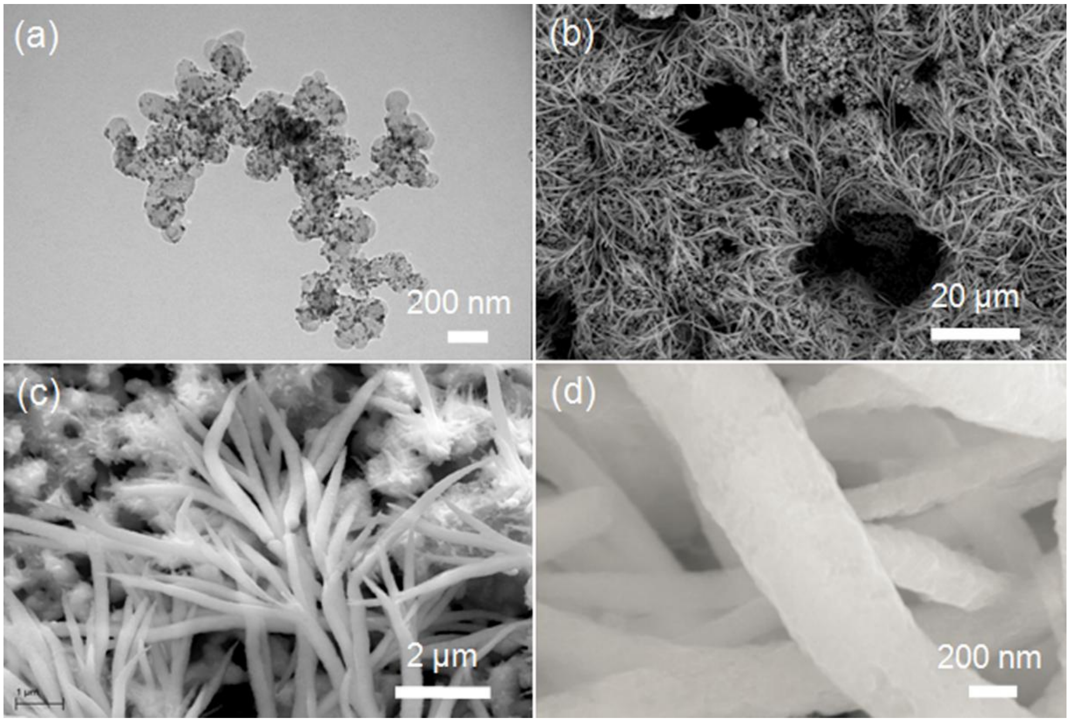

Figure 6. 1(a) TEM image of carbon black supported platinum nanoparticles; (b) the FESEM image of cathode surface view with novel platinum nanowire network structured current collector; (c) Magnification of cathode surface with platinum nanowire network; (d) single platinum nanowire.

The magnified FESEM image (Fig. 6.3a) shows that the platinum nano-network is composed of many small trees connected with one another through their branches. Meanwhile, the nano-network can effectively avoid blocking the surface open pores of the cathode. This can be seen from Fig. 6.3b, where the large open pores on cathode surface were still present uniformly.

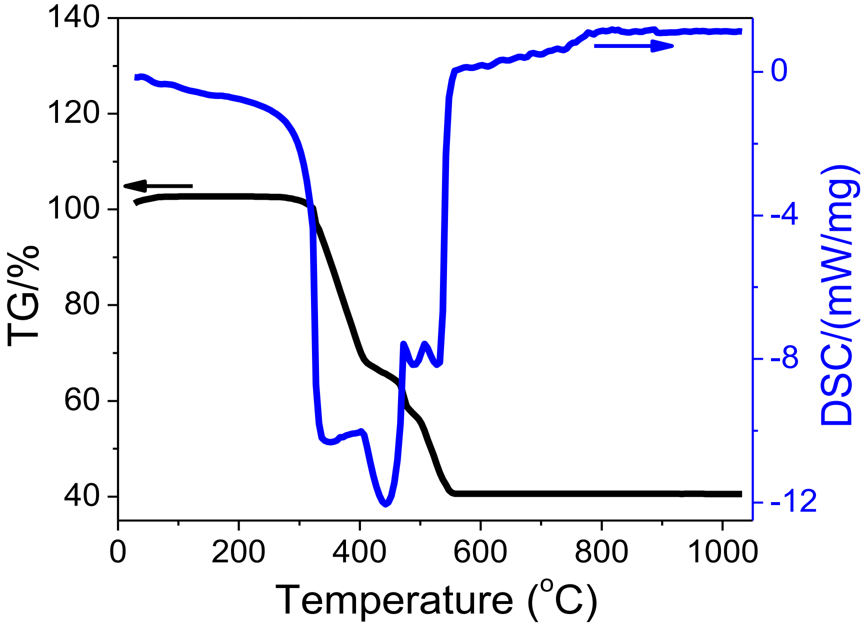

Figure 6. 2 The TGA and DSC curves of platinum coated carbon black powders from room temperature to 1030 °C with heating rate of 10 °C min^{-1}.

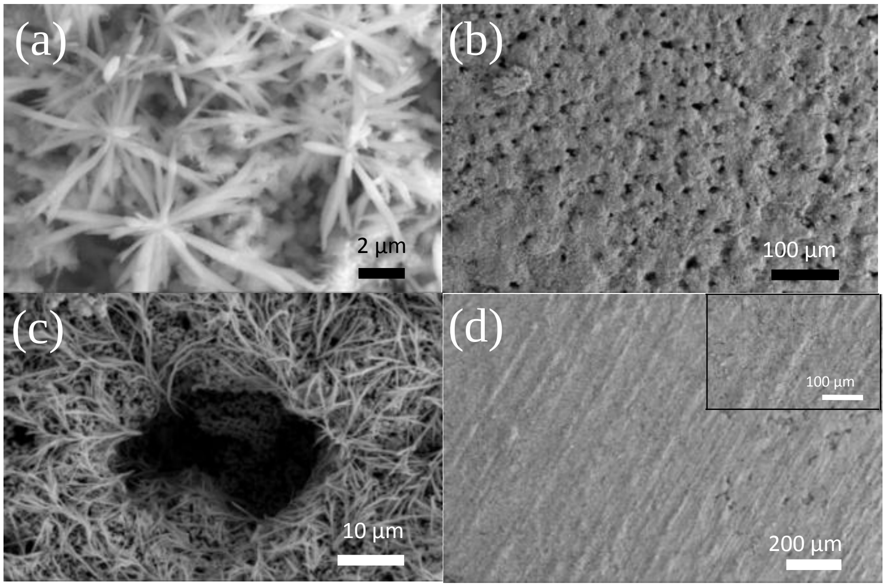

Figure 6. 3 Morphology of current collector surface: (a) Tree-branch like platinum nanowire network covered on the cathode surface; (b) The open pores uniformly distributed on the cathode surface with the platinum nanowire network current collector; (c) The cathode surface with platinumnano-wire network reaching the internal surface of open pores; (d) The cathode surface view of conventional platinum current collector fabricated by painting the Pt paste (the magnified FESEM is inserted).

The platinum nano-network even reached the internal surface of the open pores (Fig. 6.3c). Therefore current collector with nano-wire network can achieve facile oxygen diffusion. By contrast, the current collector fabricated by painting the Pt paste shows a relatively thick layer covered on the cathode surface (Fig. 6.3d), which could block the surface open pores of the cathode particularly the small open pores, significantly increasing the resistance of oxygen diffusion.

The performance of the platinum nanowire network as current collectors was evaluated by measuring the EIS of the symmetric cells of PBCO/SDC electrolyte/PBCO, where the either side of the symmetrical cell was covered with the nanowire current collector. The Pt nanowire loading was controlled by the spraying/ejecting time length of the platinum nanoparticle coated carbon black ink. Here the spraying time of 20 seconds was used as an example.

Fig. 6.4 shows EIS curves of the symmetrical cell measured in ambient air at 650 ^{o}C. The high-frequency intercept with the real-axis is primarily due to the electrolyte ohmic resistance (R_o) while the difference between the low frequency and high frequency intercept represents the overall electrode polarization resistance (R_p). From Fig. 6.4a, we can see that the R_p was only 0.1 Ω cm^2 with the nanowire network current collector. With the conventional Pt paste as the current collector, the R_p reached about 0.15 Ω cm^2. Therefore, it is reasonable to believe that the nanowire network current collector plays an important role in reducing the electrode polarization resistance. Accordingly the loading of platinum nanowire on the electrodes of the symmetric cells was varied by systematically changing the spraying time length of platinum coated carbon black ink.

The corresponding polarization resistance (R_p) was measured using EIS technique in ambient air at 650 °C. As shown in Fig. 6.4b, with the spraying time length of 5 seconds, the R_p was as high as 0.37 Ω cm^2.

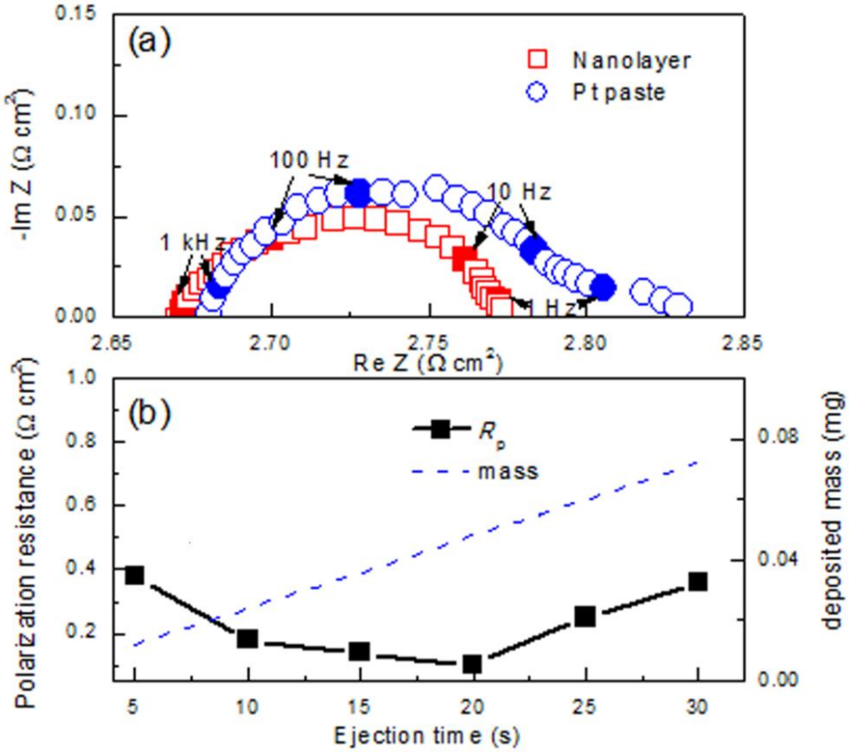

Figure 6. 4 (a) The Nyquist plots of symmetric cells with composition of PBCO/SDC/PBCO with different types of current collectors at 650 °C; (b) R_p vs. ejection time (sprayed platinum nanoparticle mass) at 650 °C.

Increasing the spraying time length to 10 seconds, the R_p was significantly reduced to 0.18 Ω cm^2. When the spraying time was increased to 15 seconds and 20 seconds, the R_p was reduced to 0.14 Ω cm^2 and 0.1 Ω cm^2 respectively. Further increasing the spraying time to 25 seconds and 30 seconds, however, the R_p was in turn increased to 0.22 Ω cm^2 and 0.32 Ω cm^2 respectively. The optimal spraying time is about 20 seconds.

The SOFCs require that the porous electrodes have not only high charge conductivity for electrons and ions but also low resistance for gas diffusion. Due to the confined space in the electrodes, these two factors are usually competing or conflicting.[154] For example, to obtain facial gas diffusion, the larger porosity is desired for the electrodes, which can in turn reduce the effective conductivity of the electrode. Conversely, relatively smaller porosity is beneficial for improving the effective conductivity of the electrode; it will inevitably increase the resistance for gas diffusion. The ideal electrodes should have sufficient material backbone for charge transport while having enough open pores for facial gas diffusion.

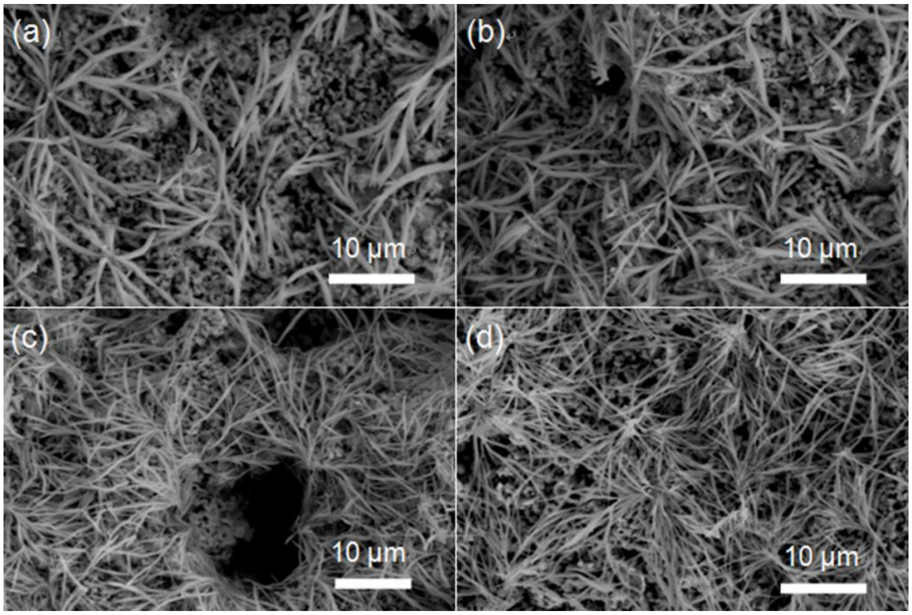

Figure 6. 5 The spraying time length and the resulting density distribution of platinum nanowire network on the cathode surface. (a) 5s; (b) 15s; (c) 20 s; (d) 30 s.

With relatively short spraying time of 5 seconds, the formed nanowire network can only partially cover the electrode surface (Fig. 6.5a). Since some of the ORR sites could not directly connect to the external circuit through the nanowire network in this case, the polarization resistance was relatively high (0.37 Ω cm^2). With the spraying time of 15 seconds, the electrode surface covered by the nanowire network was obviously increased (Fig. 6.5b). Accordingly the polarization resistance was reduced (0.14 Ω cm^2).

Further increasing the spraying time to 20 seconds, the covered electrode surface was further improved (Fig. 6.5c), making the polarization resistance further decrease (0.1 Ω cm^2). With the longer spraying time of 30 seconds, the covered electrode surface with nanowire network was further improved (Fig. 6.5d), however, too many nanowires could block the small open pores, resulting in the increase of the gas diffusion resistance and the overall polarization resistance (0.32 Ω cm^2).

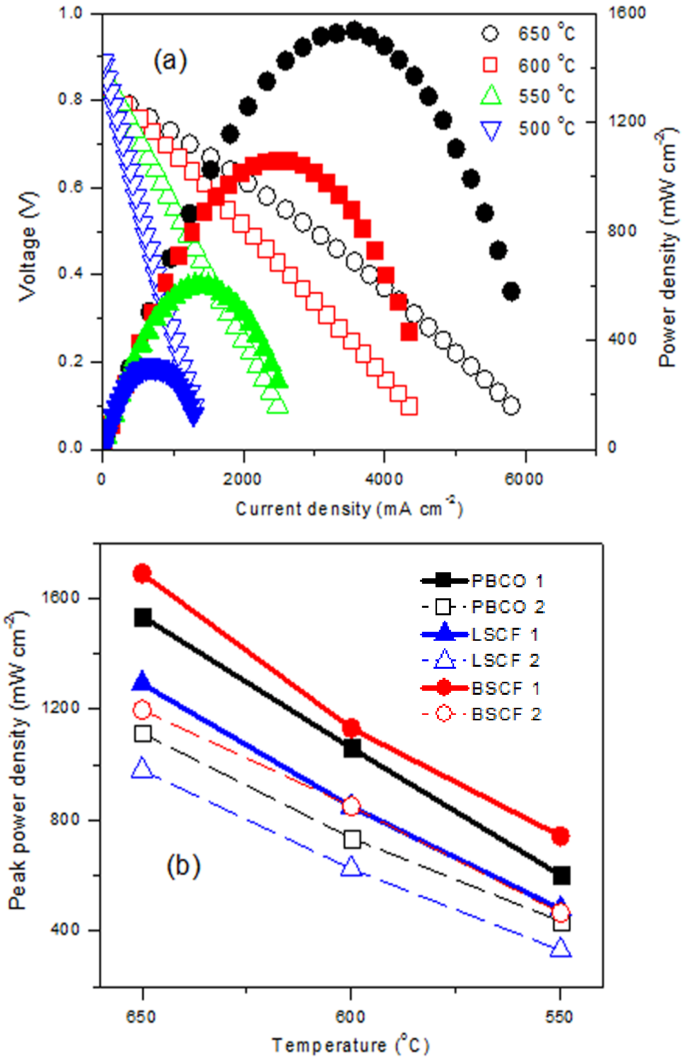

Figure 6. 6(a) Performance of the anode-supported fuel cell NiO-SDC/SDC/PBCO with platinumnanowire network as the current collector; (b) The comparisons of peak power densities of anode-supported fuel cells with different cathode materials, e.g., LSCF, BSCF, PBCO, and with different current collectors: platinum nanowire network current

collector (solid line), conventional Pt paste current collector (dashed line).

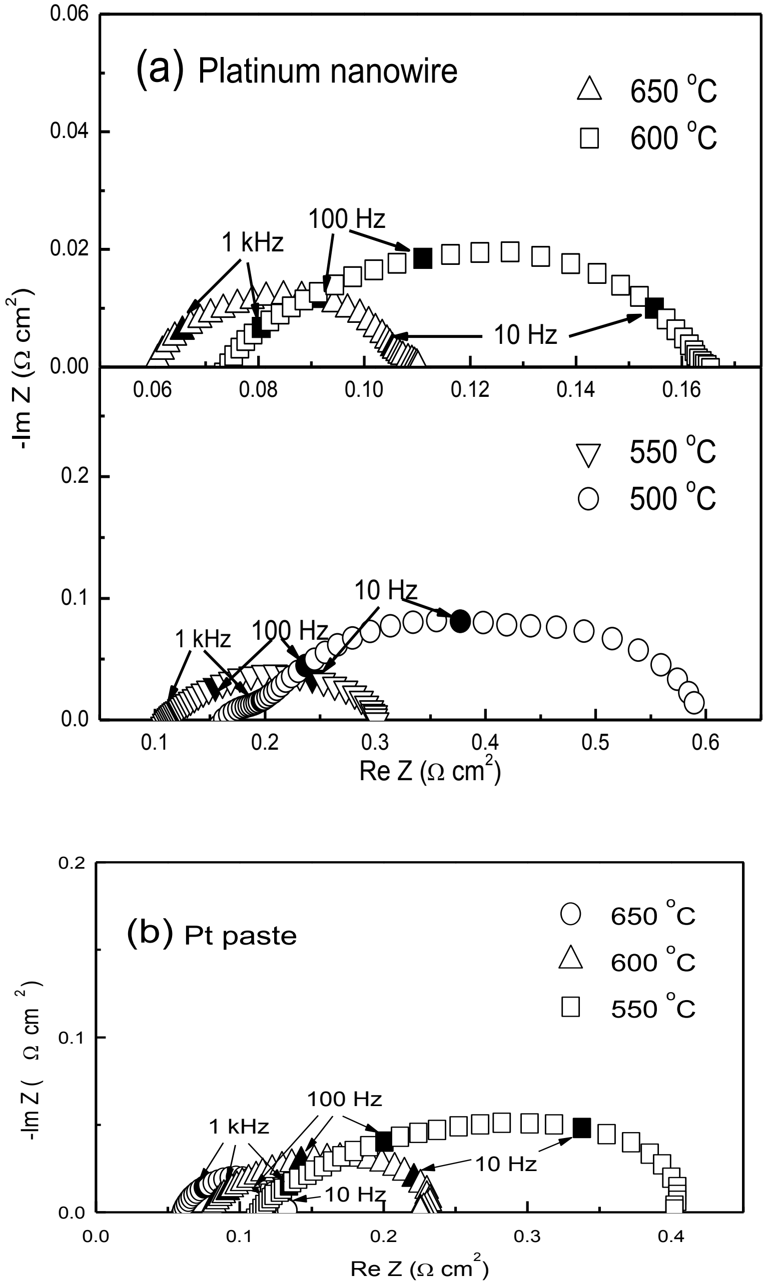

Figure 6. 7 Impedance spectra measured under open-circuit conditions with different current collectors: (a) platinum nanowire network; (b) conventional Pt paste.

The electrochemical performance of the anode-supported cell NiO-SDC/SDC/PBCO was evaluated, in which the cathode current collector was fabricated by spraying the platinum nanoparticle coated carbon black ink for 20 seconds. The ambient air was used as the oxidant while the humidified H_2 (~ 3% H_2O) was supplied to the anode chamber as the fuel. As shown in Fig. 6.6a, the peak power density of the cell reached 1535 mW cm^{-2} at 650 ^{o}C, 1060 mW cm^{-2} at 600 ^{o}C, 601 mW cm^{-2} at 550 ^{o}C and 305 mW cm^{-2} at 500 ^{o}C, respectively. For the same cell with the conventional platinum paste current collector, the power density only reached 1114 mW cm^{-2} at 650 ^{o}C, 735 mW cm^{-2} at 600 ^{o}C and 435 mW cm^{-2} at 550 ^{o}C, respectively (Fig. 6.6b).

This simple comparison showed that, with the nanowire network current collector, the power density of the cell was improved by 37.8% at 650 ^{o}C, 44.2% at 600 ^{o}C and 38.2 % at 550 ^{o}C respectively. The corresponding EIS of the cell with the nanowire current collector under open circuit conditions are shown in Fig. 6.7a. The total polarization resistance, including both the cathode and anode polarizations, was 0.43, 0.19, 0.09 and 0.05 Ω cm^2 at 500, 550, 600 and 650 ^{o}C, respectively. For the same cell with conventional Pt paste current collector, the total polarization resistance was 0.285 Ω cm^2 at 550 ^{o}C, 0.15 Ω cm^2 at 600 ^{o}C and 0.07 Ω cm^2 at 650 ^{o}C respectively (Fig. 6.7b). Since the cathode current collector is the only difference between these two cells, it is reasonable to believe that the platinum nanowire network current collector significantly reduced the cathode polarization resistance.

To demonstrate the generality and effectiveness of the nanowire network current collectors, the PBCO cathode was replaced by the widely used cathode materials of LSCF[19] and BSCF[20] respectively. As shown in Fig. 6.6b, with the conventional platinum paste as the cathode current collector, the power density of the anode supported cell Ni-SDC/SDC/LSCF reached 980 mW cm^{-2} at 650 ^{o}C, 624 mW cm^{-2} at 600 ^{o}C and 330 mW cm^{-2} at 550 ^{o}C respectively. With the platinum nanowire current collector, the power density reached 1292 mW cm^{-2} at 650 ^{o}C, 849 mW cm^{-2} at600 ^{o}C and 479 mW cm^{-2} at 550 ^{o}C, respectively. Accordingly the cell performance showed the improvement of 31.8% at 650 ^{o}C, 36.1% at 600 ^{o}C and 45.2% at 550 ^{o}C respectively. For the BSCF cathode, the cell Ni-SDC/SDC/BSCF also showed significant improvement of electrochemical performance. Specifically with conventional Pt paste current collector, the power density reached 1197 mW cm^{-2} at 650 ^{o}C, 850 mW cm^{-2} at 600 ^{o}C and 465 mW cm^{-2} at 550 ^{o}C, respectively. With platinum nanowire network current collector, the power density reached 1690 mW cm^{-2} at 650 ^{o}C, 1131mW cm^{-2} at 600 ^{o}C and 742 mW cm^{-2} at 550 ^{o}C respectively, an improvement of 41.2% at 650 ^{o}C, 33.1% at 600 ^{o}C and 59.6% at 550 ^{o}C, respectively.

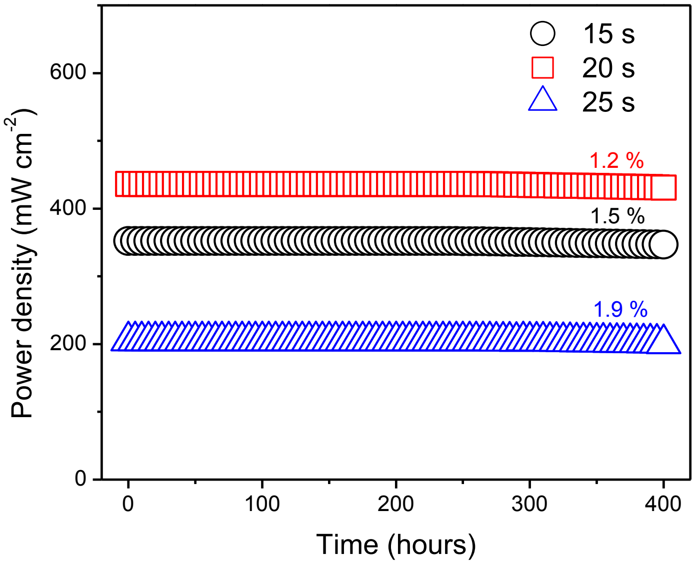

Figure 6. 8 The long-term stability of the button cell Ni-SDC/SDC/PBCO with different loadings of platinum nanowire network as the cathode current collectors at 600 ^{o}C for 400 h.

To examine the stability of the micro-morphology of nanowire current collector and the durability of the associated cell, the long-term electrochemical test was performed for 400 hours. We considered three anode supported cells Ni-SDC/SDC/PBCO with different loadings of platinum current collectors. The loading time of platinum ink was controlled at 15 s, 20 s and 25 s, respectively. The history of corresponding peak power density was shown in Fig. 6.8. The performance degradation exhibited only 1.5%, 1.2% and 1.9% respectively. The degradation could be attributed to every single component and interface in the cell, which is beyond the scope of this paper. However, the FESEM images of the current collectors after the long term test (100 h and 400 h) did not show too much difference from those before the long term test (Fig. 6.9 and Fig. 6.1b), indicating that the platinum nanowire network current collector is feasible to improve the cell performance while achieving certain durability for intermediate temperature SOFCs.

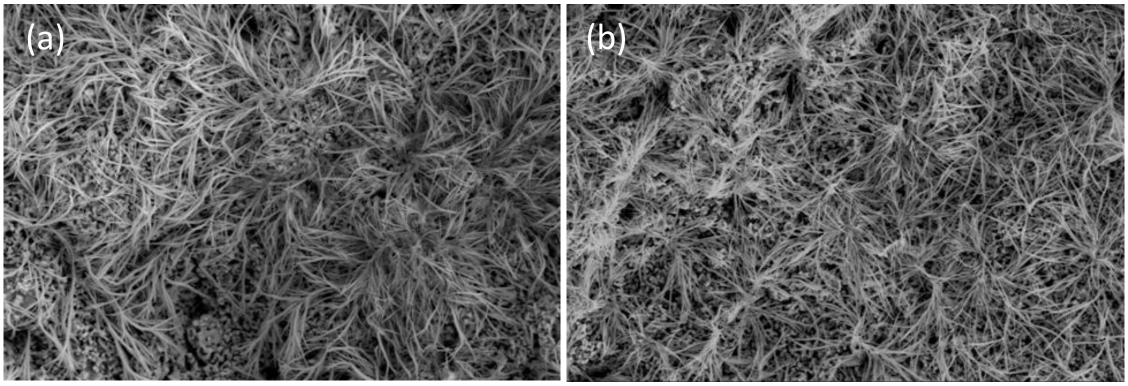

Figure 6. 9 The surface morphology of platinum nanowire network current collector in post-test cells: (a) 100 h; (b) 400 h.

6.3 SUMMARY

In conclusion, a platinum nanowire network was successfully developed as an ultrathin electrochemically efficient current collector for intermediate temperature SOFCs. The unique platinum network on cathode surface can connect the ORR sites at the nano-scale to the external circuit while being able to substantially avoid blocking the open pores of the cathode. The superior electrochemical performance was exhibited, including the highly reduced electrode polarization resistance of 0.1 Ω cm^2, improved power density of 1535 mW cm^{-2} at 650 ^oC in hydrogen and good thermal-cycle stability. Furthermore, this novel nano-scale platinum current collector can be extensively applied to other cathode materials and cell structures while showing the capability of being scaled up for mass productions due to the easily operated spraying process.

REFERENCES

1. B. C. H. Steele and A. Heinzel, “Materials for fuel-cell technologies” *Nature* **2001**, *414*, 345-352.

2. U. Stimming, S. C. Singhal, H. Tagawa and W. Lehnert, *Solid Oxide Fuel Cell V*, p1349.

3. A. Arsalis, “Thermoeconomic modeling and parametric study of hybrid SOFC–gas turbine–steam turbine power plants ranging from 1.5 to 10MWe” *J. Power Sources* **2008**, *181*, 313-326.

4. S. M. Haile, “Fuel cell materials and components” *Acta Mater.* **2003**, *51*, 5981-6000.

5. E. Antolini and E. R. Gonzalez, “Alkaline direct alcohol fuel cells” *J. Power Sources* **2010**, *195*, 3431-3450.

6. R. Lan, X. X. Xu, S. W. Tao and J. T. S. Irvine, “A fuel cell operating between room temperature and 250 degrees C based on a new phosphoric acid based composite electrolyte” *J. Power Sources* **2010**, *195*, 6983-6987.

7. M. A. Hickner, H. Ghassemi, Y. S. Kim, B. R. Einsla and J. E. McGrath, “Alternative polymer systems for proton exchange membranes (PEMs)” *Chem. Rev.* **2004**, *104*, 4587-4611.

8. N. Q. Minh, “Ceramic Fuel-Cells” *J. Am. Ceram. Soc.* **1993**, *76*, 563-588.

9. S. D. Park, J. M. Vohs and R. J. Gorte, “Direct oxidation of hydrocarbons in a solid-oxide fuel cell” *Nature* **2000**, *404*, 265-267.

10. S. C. Singhal, “Advances in solid oxide fuel cell technology” *Solid State Ionics* **2000**, *135*, 305-313.

11. S. McIntosh and R. J. Gorte, “Direct hydrocarbon solid oxide fuel cells” *Chem. Rev.* **2004**, *104*, 4845-4865.

12. A. Atkinson, S. Barnett, R. J. Gorte, J. T. S. Irvine, A. J. Mcevoy, M. Mogensen, S. C. Singhal and J. Vohs, “Advanced anodes for high-temperature fuel cells” *Nat. Mater.* **2004**, *3*, 17-27.

13. B. A. Boukamp, “Fuel cells: The amazing perovskite anode” *Nature Mater.* **2003**, *2*,

294-296.

14. O. Yamamoto, “Solid oxide fuel cells: fundamental aspects and prospects” *Electrochim. Acta* **2000**, *45*, 2423-2435.

15. S. C. Singhal and K. Kendall, “High-temperature solid oxide fuel cells: fundamentals, design, and applications” *Elsevier*, 2003.

16. R. T. Leah, N. P. Brandon and P. Aguiar, “Modelling of cells, stacks and systems based around metal-supported planar IT-SOFC cells with CGO electrolytes operating at 500–600 ^{o}C” *J. Power Sources* **2005**, *145,* 336-352.

17. E. S. Greene, W. K. S. Chiu and M. G. Medeiros, “Mass transfer in graded microstructure solid oxide fuel cell electrodes” *J. Power Sources* **2006**, *161*, 225-231.

18. C. D. Zuo, S. W. Zha, M. L. Liu, M. Hatano and M. Uchiyama, “$Ba(Zr_{0.1}Ce_{0.7}Y_{0.2})O_{3-\delta}$ as an electrolyte for low-temperature solid-oxide fuel cells” *Adv. Mater.* **2006**, *18*, 3318-3320.

19. A. V. Virkar, J. Chen, C. W. Tanner and J. W. Kim, “The role of electrode microstructure on activation and concentration polarizations in solid oxide fuel cells” *Solid State Ionics* **2000**, *131*, 189-198.

20. T. Suzuki, Z. Hasan, Y. Funahashi, T. Yamaguchi, Y. Fujishiro and M. Awano, “Impact of anode microstructure on solid oxide fuel cells” *Science* **2009**, *325,* 852-855.

21. D. J. L. Brett, A. Atkinson, N. P. Brandon and S. J. Skinner, “Intermediate temperature solid oxide fuel cells” *Chem. Soc. Rev.* **2008**, *37,* 1568-1578.

22. E. D. Wachsman and K. T. Lee, “Lowering the temperature of solid oxide fuel cells” *Science* **2011**, *334*, 935-939.

23. M. Ni, M. K. H. Leung and D. Y. C. Leung, “Micro-scale modelling of a functionally graded Ni-YSZ anode” *Chem. Eng. Technol.* **2007**, *30,* 587-592.

24. D. H. Dong, J. F. Gao, X. Q. Liu and G. Y. Meng, “Fabrication of tubular NiO/YSZ anode-support of solid oxide fuel cell by gelcasting” *J. Power Sources* **2007**, *165*, 217-223.

25. G. Y. Meng, G. L. Ma, Q. L. Ma, R. R. Peng and X. Q. Liu, “Ceramic membrane fuel cells based on solid proton electrolytes” *Solid State Ionics* **2007**, *178,* 697-703.

26. C. R. Xia and M. L. Liu, “Low-temperature SOFCs based on $Gd_{0.1}Ce_{0.9}O_{1.95}$ fabricated by dry pressing” *Solid State Ionics* **2001**, *144,* 249-255.

27. Z. P. Shao and S. M. Haile, “A high-performance cathode for the next generation of

solid-oxide fuel cells" *Nature* **2004**, *431*, 170-173.

28. E. P. Murray, T. Tsai and S. A. Barnett, "Oxygen transfer processes in (La,Sr)MnO_3/Y_2O_3-stabilized ZrO_2 cathodes: an impedance spectroscopy study" *Solid State Ionics* **1998**, *110*, 235-243.

29. H. P. Ding, B. Lin, X. Q. Liu and G. Y. Meng, "High performance protonic ceramic membrane fuel cells (PCMFCs) with $Ba_{0.5}Sr_{0.5}Zn_{0.2}Fe_{0.8}O_{3-\delta}$ perovskite cathode" *Electrochem. Commun.* **2008**, *10*, 1388-1391.

30. R. R. Peng, T. Z. Wu, W. Liu, X. Q. Liu and G. Y. Meng, "Cathode processes and materials for solid oxide fuel cells with proton conductors as electrolytes" *J. Mater. Chem.* **2010**, *20*, 6218-6225.

31. R. M. Ormerod, "Solid oxide fuel cells" *Chem. Soc. Rev.* **2003**, *32*, 17-28.

32. Z. P. Shao, W. Zhou and Z. H. Zhu, "Advanced synthesis of materials for intermediate-temperature solid oxide fuel cells" *Prog. Mater. Sci.* **2012**, *57*, 804-874.

33. S. P. Jiang, "A review of wet impregnation—An alternative method for the fabrication of high performance and nano-structured electrodes of solid oxide fuel cells" *Mat. Sci. Eng. R. A* **2006**, *418*, 199-210.

34. J. Fleig, "Solid oxide fuel cell cathodes: polarization mechanisms and modeling of the electrochemical performance" *Annu. Rev. Mater. Res.* **2003**, *33*, 361-382.

35. A. J. Jacobson, "Materials for solid oxide fuel cells" *Chem. Mater.* **2010**, *22*, 660-674.

36. W. G. Wang and M. Mogensen, "High-performance lanthanum-ferrite-based cathode for SOFC" *Solid State Ionics* **2005**, *176*, 457-462.

37. Y. Lin, R. Ran and Z. P. Shao, "Silver-modified $Ba_{0.5}Sr_{0.5}Co_{0.8}Fe_{0.2}O_{3\text{-delta}}$ as cathodes for a proton conducting solid-oxide fuel cell" *Int. J. Hydrogen Energy* **2010**, *35*, 8281-8288.

38. C. R. Xia, W. Rauch, F. L. Chen, and M. L. Liu, "$Sm_{0.5}Sr_{0.5}CoO_3$ cathodes for low-temperature SOFCs" *Solid State Ionics*, **2002**, *149*, 11-19.

39. F. Zhao, Z. Y. Wang, M. F. Liu, L. Zhang, C. R. Xia and F. L. Chen, "Novel nano-network cathodes for solid oxide fuel cells" *J. Power Sources* **2008**, *185*, 13-18.

40. A. Tarancón, S. J. Skinner, R. J. Chater, F. Hernández-Ramírez and J. A. Kilner, "Layered perovskites as promising cathodes for intermediate temperature solid oxide fuel cells" *J. Mater. Chem.* **2007**, *17*, 3175-3181.

41. G. Kim, S. Wang, A. J. Jacobson, L. Reimus, P. Brodersen, and C. A. Mims, "Rapid oxygen ion diffusion and surface exchange kinetics in $PrBaCo_2O_{5+x}$ with a perovskite related structure and ordered A cations" *J. Mater. Chem.* **2007**, *17*, 2500-2505.

42. A. Maignan, C. Martin, D. Pelloquin, N. Nguyen and B. Raveau, "Structural and magnetic studies of ordered oxygen-deficient perovskites $\mathit{Ln}BaCo_2O_{5+\delta}$, closely related to the "112" structure" *J. Solid State Chem.* **1999**, *142*, 247-260.

43. J. Peña-Martínez, A. Tarancón, D. Marrero-López, J. C. Ruiz-Morales and P. Núñez, "Evaluation of $GdBaCo_2O_{5+\delta}$ as cathode material for doped lanthanum gallate electrolyte IT-SOFCs" *Fuel Cells* **2008**, *5*, 351-359.

44. C. Frontera, J. L. García-Muñoz, A. Llobet, L. Mañosa and M. A. G. Aranda, "Selective spin-state and metal–insulator transitions in $GdBaCo_2O_{5.5}$" *J. Solid State Chem.* **2003**, *171*, 349-352.

45. M. Respaud, C. Frontera, J. L. García-Muñoz, M. Á. G. Aranda, B. Raquet, J. M. Broto, H. Rakoto, M. Goiran, A. Llobet and J. Rodríguez-Carvajal, "Magnetic and magnetotransport properties of $GdBaCo_2O_{5+\delta}$: A high magnetic-field study" *Phys. Rev. B* **2001**, *64*, 214401.

46. B. A. Stuart, "Factors governing oxygen reduction in solid oxide fuel cell cathodes" *Chem. Rev.* **2004**, *104*, 4791-4843.

47. N. P. Brandon, S. Skinner and B. C. H. Steele, "Recent advances in materials for fuel cells" *Annu. Rev. Mater. Sci.* **2003**, *33*, 183-213.

48. Y-L. Lee, J. Kleis, J. Rossmeisl, Y. Shao-Horn and D. Morgan, "Prediction of solid oxide fuel cell cathode activity with first-principles descriptors" *Energy Environ. Sci.* **2011**, *4*, 3966-3970.

49. J. Suntivich, H. A. Gasteiger, N. Yabuuchi, H. Nakanishi, J. B. Goodenough and Y. Shao-Horn, "Design principles for oxygen-reduction activity on perovskite oxide catalysts for fuel cells and metal–air batteries" *Nat. Chem.* **2011**, *3*, 546-550.

50. H. Ullmann, N. Trofimenko, A. Naoumidis and D. Stover, "Ionic/electronic mixed conduction relations in perovskite-type oxides by defect structure" *J. Eur. Ceram. Soc.* **1999**, *19*, 791-796.

51. H. Kishimoto, N. Sakai, T. Horita, K. Yamaji, M. E. Brito and H. Yokokawa, "Cation transport behavior in SOFC cathode materials of $La_{0.8}Sr_{0.2}CoO_3$ and $La_{0.8}Sr_{0.2}FeO_3$ with perovskite structure" *Solid State Ionics* **2007**, *178*, 1317-1325.

52. W. Zhou, R. Ran and Z. P. Shao, "Progress in understanding and development of $Ba_{0.5}Sr_{0.5}Co_{0.8}Fe_{0.2}O_{3\text{-delta}}$-based cathodes for intermediate-temperature solid-oxide fuel cells: A review" *J. Power Sources* **2009**, *192*, 231-246.

53. K. Zhang, L. Ge, R. Ran, Z. P. Shao and S. M. Liu, “Synthesis, characterization and evaluation of cation-ordered $LnBaCo_{(2)}O_{(5+delta)}$ as materials of oxygen permeation membranes and cathodes of SOFCs” *Acta Mater.* **2008**, *56*, 4876-4889.
54. Z. P. Shao, “Cathode materials for solid oxide fuel cells towards operating at intermediate-to-Low Temperature Range” *Prog. Chem.* **2011**, *23*, 418-429.

55. C. Gaudillere, L. Olivier, P. Vernoux, C. M. Zhang, Z. P. Shao and D. Farrusseng, “Alternative perovskite materials as a cathode component for intermediate temperature single-chamber solid oxide fuel cell” *J. Power Sources* **2010**, *195*, 4758-4764.

56. J. Richter, P. Holtappels, T. Graule, T. Nakamura and L. J. Gauckler, “Materials design for perovskite SOFC cathodes” *Monatsh Chem.* **2009**, *140*, 985-999.

57. C. W. Sun, R. Hui and J. Roller, “Cathode materials for solid oxide fuel cells: a review” *J. Solid State Electrochem.* **2010**, *14*, 1125-1144.

58. S. Svarcova, K. Wiik, J. Tolchard, H. J. M. Bouwmeester and T. Grande, “Structural instability of cubic perovskite $Ba_xSr_xSr_{1-x}Co_{1-y}Fe_yO_{3-delta}$” *Solid State Ionics* **2008**, *178*, 1787-1791.

59. O. Muller and R. Roy, “The major ternary structural families” *Springer*, Heidelberg, 1974.

60. J. P. Attfield, “A' cation control of perovskite properties” *Cryst. Eng.* **2002**, *3-4*, 427-438.

61. R. D. Shannon, “Revised effective ionic radii and systematic studies of interatomie distances in halides and chaleogenides” *Acta Cryst.* **1976**, *A32*, 751-767.

62. J. W. Stevenson, T. R. Armstrong, R. D. Carneim, L. R. Pederson and W. J. Weber, “Electrochemical properties of mixed conducting perovskites $La_{1-x}M_xCo_{1-y}Fe_yO_{3-\delta}$ (M = Sr, Ba, Ca)” *J. Electrochem. Soc.* **1996**, *143*, 2722–2729.

63. M. Petitjean, G. Caboche, E. Siebert, L. Dessemond and L.-C. Dufour, “$(La_{0.8}Sr_{0.2})(Mn_{1-y}Fe_y)O_{3\pm\delta}$ oxides for ITSOFC cathode materials?: Electrical and ionic transport properties” *J. Eur. Ceram. Soc.* **2005**, *25*, 2651-2654.

64. X. Q. Huang, L. Pei, Z. G. Liu, Z. Lu, Y. Sui, Z. N. Qian and W. H. Su, “A study on $PrMnO_3$-based perovskite oxides used in SOFC cathodes” *J. Alloy Compd.* **2002**, *345*, 265-270.

65. S. L. Wang, B. Lin, K. Xie, Y. C. Dong, X. Q. Liu and G. Y. Meng, “ Low temperature sintering ability and electrical conductivity of SOFC interconnect material “ $La_{0.7}Ca_{0.3}Cr_{0.97}O_3$” *J. Alloy Compd.* **2009**, *468*, 499-504.

66. G. C. Kostogloudis, N. Vasilakos and Ch. Ftikos, “Preparation and characterization of

$Pr_{1-x}Sr_xMnO_{3\pm\delta}$ (x = 0, 0.15, 0.3, 0.4, 0.5) as a potential SOFC cathode material operating at intermediate temperatures (500-700 ℃)" *J. Eur. Ceram. Soc.* **1997**, *17*, 1513-1521.

67. W. Khan, A. H. Naqvi, M. Gupta, S. Husain and R. Kumar, "Small polaron hopping conduction mechanism in Fe doped $LaMnO_3$" *J. Chem. Phys.* **2011**, *135*, 054501.

68. K. Q. Huang and J. B. Goodenough, "A solid oxide fuel cell based on Sr- and Mg-doped $LaGaO_3$ electrolyte: the role of a rare-earth oxide buffer" *J. Alloy Compd.* **2000**, *303*, 454-464.

69. K. Q. Huang, R. Tichy and J. B. Goodenough, "Superior perovskite oxide-ion conductor; strontium- and magnesium-doped $LaGaO_3$: III, Performance tests of single ceramic fuel cells" *J. Am. Ceram. Soc.* **1998**, *81*, 2581-2585.

70. M. S. Islam, M. Cherry and C. R. A. Catlow, "Oxygen diffusion in $LaMnO_3$ and $LaCoO_3$ perovskite-type oxides: a molecular dynamics study" *J. Solid State Chem.* **1996**, *124*, 230-237.

71. J. A. Kilner, "A study of oxygen ion conductivity in doped non-stoichiometric oxides" *Solid State Ionics* **1982**, *6*, 237-252.

72. O. Fukunaga and T. Fujita, "The relation between ionic radii and cell volumes in the perovskite compounds" *J. Solid State Chem.* **1973**, 8, 331-338.

73. M. Mogensen, D. Lybye, N. Bonanos, P. V. Hendriksen and F. W. Poulsen, "Factors controlling the oxide ion conductivity of fluorite and perovskite structured oxides" *Solid State Ionics* **2004**, *174*, 279-286.

74. M. J. Jorgensen and M. Mogensen, "Impedance of solid oxide fuel cell LSM/YSZ composite cathodes" *J. Electrochem. Soc.* **2001**, *148*, A433-A442.

75. J. D. Kim, G. D. Kim, J. W. Moon, Y. I. Park, W. H. Lee, K. Kobayashi, M. Nagai and C. E. Kim, "Characterization of LSM-YSZ composite electrode by ac impedance spectroscopy" *Solid State Ionics* **2001**, *143*, 379-389.

76. J. Geck, P. Wochner, S. Kiele, R. Klingeler, A. Revcolevschi, M. V. Zimmermann, B. Büchner and P. Reutler, "Orbital order induced ferromagnetic insulating properties" *New J. Phys.* **2001**, *143*, 379-389.

77. S. P. Jiang, "Development of lanthanum strontium manganite perovskite cathode materials of solid oxide fuel cells: a review" *J. Mater. Sci.* **2008**, *43*, 6799-6833.

78. S. P. Jiang, "A comparison of O_2 reduction reactions on porous $(La,Sr)MnO_3$ and $(La,Sr)(Co,Fe)O_3$ electrodes" *Solid State Ionics* **2002**, *146*, 1-22.

79. A. M. Glazer, "Simple ways of determining perovskite structures" *Acta Crystallogr.*

1975, *A31*, 756-762.

80. P. M. Woodward, "Octahedral Tilting in Perovskites. I. Geometrical Considerations" *Acta Crystallogr.* **1997**, *B53*, 32-43.

81. P. M. Woodward, "Octahedral Tilting in Perovskites. II. Structure Stabilizing Forces" *Acta Crystallogr.* **1997**, *B53*, 44-66.

82. J. Mizusaki, Y. Yonemura, H. Kamata, K. Ohyama, N. Mori, H. Takai, H. Tagawa, M. Dokiya, K. Naraya, T. Sasamoto, H. Inaba and T. Hashimoto, "Electronic conductivity, Seebeck coefficient, defect and electronic structure of nonstoichiometric $La_{1-x}Sr_xMnO_3$" *Solid State Ionics* **2000**, *132*, 167-180.

83. T. Z. Sholklapper, C. Lu, C. P. Jacobson, S. J. Visco and L. C. De Jonghe, "LSM-Infiltrated Solid Oxide Fuel Cell Cathodes" *Electrochem. Solid State Lett.* **2006**, *9*, A376-A378.

84. A. Mai, V. A. C. Haanappel, S. Uhlenbruck, F. Tietz and D. Stover, "Ferrite-based perovskites as cathode materials for anode-supported solid oxide fuel cells Part I. Variation of composition" *Solid State Ionics* **2005**, *176*, 1341-1350.

85. V. Dusastre and J. A. Kilner, "Optimisation of composite cathodes for intermediate temperature SOFC applications" *Solid State Ionics* **1999**, *126*, 163-174.

86. M. F. Liu, D. Ding, K. Blinn, X. X. Li, L. F. Nie and M. L. Liu, "Enhanced performance of LSCF cathode through surface modification" *Int. J. Hydrogen Energy* **2012**, *37*, 8613-8620.

87. B. Wei, Z. Lü, X. Q. Huang, J. P. Miao, X. Q. Sha, X. S. Xin and S. H. Su, "Crystal structure, thermal expansion and electrical conductivity of perovskite oxides $Ba_xSr_{1-x}Co_{0.8}Fe_{0.2}O_{3-\delta}$ $(0.3\leq x\leq 0.7)$" *J. Eur. Ceram. Soc.* **2006**, *26*, 2827-2832.

88. C. Martin, A. Maignan, D. Pelloquin, N. Nguyen and B. Raveau, "Magnetoresistance in the oxygen deficient $LnBaCo_2O_{5.4}$ (Ln=Eu, Gd) phases" *Appl. Phys. Lett.* **1997**, *71*, 1421-1423.

89. Y. Moritomo, M. Takeo, X. J. Liu, T. Akimoto and A. Nakamura, "Metal-insulator transition due to charge ordering in $R_{1/2}Ba_{1/2}CoO_3$" *Phys. Rev. B* **1998**, *58*, R13334-R13337.

90. T. Vogt, P. M. Woodward, P. Karen, B. A. Hunter, P. Henning and A. R. Moodenbaugh, "Low to high spin-state transition induced by charge ordering in antiferromagnetic $YBaCo_2O_5$" *Phys. Rev. Lett.* **2000**, *84*, 2969-2972.

91. J. C. Burley, J. F. Mitchell, S. Short, D. Miller and Y. Tang, "Structural and magnetic chemistry of $NdBaCo_2O_{5+\delta}$" *J. Solid State Chem.* **2003**, *170*, 339-350.

92. V. Caignaert, I. Mirebeau, F. Bouree, N. Nguyen, A. Ducouret, J.-M. Greneche and B. Raveau, “Crystal and magnetic structure of $YBaCuFeO_5$” *J. Solid State Chem.* **1995**, *114*, 24-35.

93. A. Taskin, A. Lavrov and Y. Ando, “Transport and magnetic properties of $GdBaCo_2O_{5+x}$ single crystals: A cobalt oxide with square-lattice CoO_2 planes over a wide range of electron and hole doping” *Phys. Rev. B* **2005**, *71*, 134414-134441.

94. C. Frontera, A. Caneiro, A. E. Carrillo, J. Oró-Solé and J. L. García-Mun˜oz, “Tailoring oxygen content on $PrBaCo_2O_{5+\delta}$ layered cobaltites” *Chem. Mater.* **2005**, *17*, 5439-5445.

95. L. Mogni, F. Prado, C. Jiménez and A. Caneiro, “Oxygen order-disorder phase transition in layered $GdBaCo_2O_{5+\delta}$ perovskite: Thermodynamic and transport properties” *Solid State Ionics* **2013**, *240*, 19-28.

96. Y. Moritomo, T. Akimoto, M. Takeo, A. Machida, E. Nishibori, M. Takata, M. Sakata, K. Ohoyama and A. Nakamura, “Metal-insulator transition induced by a spin-state transition in $TbBaCo_2O_{5+\delta}$ (δ=0.5)” *Phys. Rev. B* **2000**, *61*, R13325-R13328.

97. A. Tarancón, A. Morata, G. Dezanneau, S. J. Skinner, J. A. Kilner, S. Estradé, F. H.-Ramírez, R. Peiró and J. R. Morante, “$GdBaCo_2O_{5+x}$ layered perovskite as an intermediate temperature solid oxide fuel cell cathode” *J. Power Sources* **2007**, *174*, 255-263.

98. Y. Lee, D. Y. Kim and G. M. Choi, “$GdBaCo_2O_{5+x}$ cathode for anode-supported ceria SOFCs” *Solid State Ionics* **2011**, *192*, 527-530.

99. G. Kim, S. Wang, A. J. Jacobson, Z. Yuan, W. Donner, C. L. Chen, L. Reimus, P. Brodersen and C. A. Mins, “Oxygen exchange kinetics of epitaxial $PrBaCo_2O_{5+\delta}$ thin films” *Appl. Phys. Lett.* **2006**, *88*, 024103.

100. A. Tarancón, M. Burriel, J. Santiso, S. J. Skinner and J. A. Kilner, “Advances in layered oxide cathodes for intermediate temperature solid oxide fuel cells” *J. Mater. Chem.* **2010**, *20*, 3799-3813.

101. A. M. Chang, S. J. Skinner and J. A. Kilner, “Electrical properties of $GdBaCo_2O_{5+x}$ for ITSOFC applications” *Solid State Ionics* **2006**, *177*, 2009-2011.

102. C. J. Zhu, X. M. Liu, C. S. Yi, D. T. Yan and W. H. Su, “Electrochemical performance of $PrBaCo_2O_{5+\delta}$ layered perovskite as an intermediate-temperature solid oxide fuel cell cathode” *J. Power Sources* **2008**, *185*, 193-196.

103. J. M. Vohs and R. J. Gorte, “High-performance SOFC cathodes prepared by infiltration” *Adv. Mater.* **2009**, *21*, 943-956.

104. Z. Y. Jiang, C. R. Xia and F. L. Chen, “Nano-structured composite cathodes for intermediate-temperature solid oxide fuel cells via an infiltration/impregnation technique” *Electrochim. Acta* **2010**, *55*, 3595-3605.
105.T. Z. Sholklapper, H. Kurokawa, C. P. Jacobson, S. J. Visco and L. C. D. Jonghe, “Nanostructured solid oxide fuel cell electrodes” *Nano Lett.* **2007**, *7*, 2136-2141.

106. T. J. Armstrong, A. V. Virkar, “Performance of solid oxide fuel cells with LSGM-LSM composite cathodes” *J. Electrochem. Soc.* **2002**, *149*, A1565-A1567.

107. Z. L. Zhan, D. M. Bierschenk, J. S. Cronin and S. A. Barnett, “A reduced temperature solid oxide fuel cell with nanostructured anodes” *Energy Environ. Sci.* **2011**, *4*, 3951-3954.

108. T. Wei, Y. H. Huang, R. Zeng, L. X. Yuan, X. L. Hu, W. X. Zhang, L. Jiang, J. Y. Yang and Z. L. Zhang, “Evaluation of $Ca_3Co_2O_6$ as cathode material for high-performance solid-oxide fuel cell” *Sci. Rep.* **2013**, *3*, 1125.

109. A. A. Taskin, A. N. Lavrov, and Y. Ando, “Achieving fast oxygen diffusion in perovskites by cation ordering” *Appl. Phys. Lett.* **2005**, *86*, 091910.

110. G. Kim, S. Wang, A. J. Jacobson, L. Reimus, P. Brodersen and C. A. Mims, “Rapid oxygen ion diffusion and surface exchange kinetics in $PrBaCo_2O_{5+x}$ with a perovskite related structure and ordered A cations” *J. Mater. Chem.* 2007, 17, 2500-2505.

111. L. Zhao, B. B. He, B. Lin, H. P. Ding, S. L. Wang, Y. H. Ling, R. R. Peng, G. Y. Meng and X. Q. Liu, “High performance of proton-conducting solid oxide fuel cell with a layered $PrBaCo_2O_{5+\delta}$ cathode” *J. Power Sources* **2009**, *194*, 835-837.

112. C. J. Zhu, X. M. Liu, C. S. Yi, L. Pei, D. J. Wang, D. T. Yan, K. G. Yao, T. Q. Lü and W. H. Su, “High-performance $PrBaCo_2O_{5+\delta}$-$Ce_{0.8}Sm_{0.2}O_{1.9}$ composite cathodes for intermediate temperature solid oxide fuel cell” *J. Power Sources* **2010**, *195*, 3504-3507.

113. Z. B. Wang, R. R. Peng, W. H. Zhang, X. J. Wu, C. R. Xia and Y. L. Lu, “Oxygen reduction and transport on the $La_{1-x}Sr_xCo_{1-y}Fe_yO_{3-\delta}$ cathode in solid oxide fuel cells: a first-principles study” *J. Mater. Chem. A* **2013**, *1*, 12932-12940.

114. B. Wei, Z. Lü, X. Q. Huang, Z. G. Liu, J. P. Miao, N. Li and W. H. Su, “$Ba_{0.5}Sr_{0.5}Zn_{0.2}Fe_{0.8}O_{3-\delta}$ perovskite oxide as a novel cathode for intermediate-temperature solid-oxide fuel cells” *J. Am. Ceram. Soc.* **2007**, *90*, 3364-3366.

115. J. H. Kim, M. Cassidy, J. T. S. Irvine and J. Bae, “Advanced Electrochemical Properties of $LnBa_{0.5}Sr_{0.5}Co_2O_{5+\delta}$ (Ln = Pr , Sm, and Gd) as Cathode Materials for IT-SOFC” *J. Electrochem. Soc.* **2009**, *156*, B682-B689.

116. J. M. Ralph, A. C. Schoeler and M. Krumpelt, “Materials for low temperature solid oxide fuel cells” *J. Mater. Sci.* **2001**, *36*, 1161-1172.

117. K. Eguchi, T. Setoguchi, T. Inoue and H. Arai, “Electrical properties of ceria-based oxides and their application to solid oxide fuel cells” *Solid State Ionics* **1992**, *52*, 165-172.

118. S. Y. Li, Z. Lü, X. Q. Huang, B. Wei and W. H. Su, “Thermal, electrical, and electrochemical properties of lanthanum-doped $Ba_{0.5}Sr_{0.5}Co_{0.8}Fe_{0.2}O_{3-\delta}$” *J. Phys. Chem. Solids* 2007, 68, 1707-1712.

119. N. Ai, Z. Lü, K. F. Chen, X. Q. Huang, B. Wei, Y. H. Zhang, S. Y. Li, X. S. Xin, X. Q. Sha and W. H. Su, “Low temperature solid oxide fuel cells based on $Sm_{0.2}Ce_{0.8}O_{1.9}$ films fabricated by slurry spin coating” *J. Power Sources* **2006**, *159*, 637-640.

120. F. Wang, Q. J. Zhou, T. M. He, G. D. Li and H. Ding, “Novel $SrCo_{1-y}Nb_yO_{3-\delta}$ cathodes for intermediate-temperature solid oxide fuel cells” *J. Power Sources* **2010**, *195*, 3772-3778.

121. C. J. Fu, K. N. Sun, N. Q. Zhang, X. B. Chen and D. R. Zhou, “Electrochemical characteristics of LSCF – SDC composite cathode for intermediate temperature SOFC” *Electrochim. Acta* **2007**, *52*, 4589-4594.

122. Q. J. Zhou, T. M. He, Q. He and Y. Ji, “Electrochemical performances of $LaBaCuFeO_{5+x}$ and $LaBaCuCoO_{5+x}$ as potential cathode materials for intermediate-temperature solid oxide fuel cells” *Electrochem. Commun.* **2009**, *11*, 80-83.

123. E. P. Murray, M. J. Sever, and S. A. Barnett, Solid State Ionics, 148 (2002) 27.

124. A. F. Sammells, R. L. Cook, J. H. White, J. J. Osborne and R. C. MacDuff, “Rational selection of advanced solid electrolytes for intermediate temperature fuel cells” *Solid State Ionics* **1992**, *52*, 111-123.

125. A. K. Demin, P. E. Tsiakaras, V. A. Sobyanin and S. Y. Hramova, “Thermodynamic analysis of a methane fed SOFC system based on a protonic conductor” *Solid State Ionics* **2002**, *152-153*, 555-560.

126. H. P. Ding, B. Lin, Y. Z. Jiang, S. L. Wang, D. R. Fang, Y. C. Dong, S. W. Tao, R. R. Peng, X. Q. Liu and G. Y. Meng, “Low-temperature protonic ceramic membrane fuel cells (PCMFCs) with $SrCo_{0.9}Sb_{0.1}O_{3-\delta}$ cubic perovskite cathode” *J. Power Sources* **2008**, *185*, 937-940.

127. B. Lin, S. Q. Zhang, L. C. Zhang, L. Bi, H. P. Ding, X. Q. Liu, J. F. Gao and G. Y. Meng *J. Power Sources* 2008, *177*, 330-333.

128. J. T. S. Irvine, “Perovskite oxides anodes for solid oxide fuel cells” *Springer* New York, **2009**, p. 167.

129. Q. X. Fu, F. Tietz and D. Stöver, “$La_{0.4}Sr_{0.6}Ti_{1-x}Mn_xO_{3-\delta}$ perovskites as anode

materials for solid oxide fuel cells" *J. Electrochem. Soc.* **2006**, *153*, D74-D83.

130. R. Vassen, D. Simwonis and D. Stoever, "Modelling of the agglomeration of Ni-particles in anodes of solid oxide fuel cells" *J. Mater. Sci.* **2001**, *36*, 147-151.

131. S. W. Tao and J. T. S. Irvine, "A redox-stable efficient anode for solid-oxide fuel cells" *Nat. Mater.* **2003**, *2*, 320-323.

132. Y. H. Huang, R. I. Dass, Z. L. Xing and J. B. Goodenough, "Double perovskites as anode materials for solid-oxide fuel cells" *Science* **2006**, *312*, 254-257.

133. J. C. Ruiz-Morales, J. Canales-Vázquez, C. Savaniu, D. Marrero-López, W. Z. Zhou and J. T. S. Irvine, "Disruption of extended defects in solid oxide fuel cell anodes for methane oxidation" *Nature* **2006**, *439*, 568-571.

134. O. A. Marina, N. L. Canfield and J. W. Stevenson, "Thermal, electrical, and electrocatalytical properties of lanthanum-doped strontium titanate" *Solid State Ionics* **2002**, *149*, 21-28.

135. J. B. Goodenough and Y. H. Huang, "Alternative anode materials for solid oxide fuel cells" *J. Power Sources* **2007**, *173*, 1-10.

136. R. J. Gorte, J. M. Vohs and S. McIntosh, "Recent developments on anodes for direct fuel utilization in SOFC" *Solid State Ionics* **2004**, *175*, 1-6.

137. Y. H. Huang, G. Liang, M. Croft, M. Lehtimäki, M. Karppinen and J. B. Goodenough, "Double-perovskite anode materials Sr_2MMoO_6 (M = Co, Ni) for solid oxide fuel cells" *Chem. Mater.* **2009**, *21*, 2319-2326.

138 M. Chen, B. H. Kim, Q. Xu, B. G. Ahn and D. P. Huang, "Fabrication and performance of anode-supported solid oxide fuel cells via slurry spin coating" *J. Membrane Sci.* **2010**, *360*, 461-468.

139. N. Ai, Z. Lü, K. F. Chen, X. Q. Huang, Y. W. Liu, R. F. Wang and W. H. Su, "Preparation of $Sm_{0.2}Ce_{0.8}O_{1.9}$ membranes on porous substrates by a slurry spin coating method and its application in IT-SOFC" *J. Membrane Sci.* **2006**, *286*, 255-259.

140. J. D. Nicholas and L. C. D. jonghe, "Prediction and evaluation of sintering aids for Cerium Gadolinium Oxide" *Solid State Ionics* **2007**, *178*, 1187-1194.

141. M. H. D. Othman, N. Droushiotis, Z. T. Wu, G. Kelsall and K. Li, "High-performance, anode-supported, microtubular SOFC prepared from single-step-fabricated, dual-layer hollow fibers" *Adv. Mater.* **2011**, *23*, 2480-2483.

142. G. L. Xiao, Q. Liu, X. H. Dong, K. Huang, F. L. Chen, "$Sr_2Fe_{4/3}Mo_{2/3}O_6$ as anodes for solid oxide fuel cells" *J. Power Sources* **2010**, *195*, 8071-8074.

143. S. C. Singhal, “Solid oxide fuel cells for stationary, mobile, and military applications” *Solid State Ionics* **2002**, *152–153*, 405-410.

144. M. G. Bellino, J. G. Sacanell, D. G. Lamas, A. G. Leyva and N. E. W. D. Reca, “High-performance solid-oxide fuel cell cathodes based on cobaltite nanotubes” *J. Am. Chem. Soc.* **2007**, *129*, 3066-3067.

145. H. Huang, M. Nakamura, P. C. Su, R. Fasching, Y. J. Saito and F. B. Prinz, “High-performance ultrathin solid oxide fuel cells for low-temperature operation” *J. Electrochem. Soc.* **2007**, *154*, B20-B24.

146. P. C. Su, C.-C. Chao, J. H. Shim, R. Fasching and F. B. Prinz, “Solid oxide fuel cell with corrugated thin film electrolyte” *Nano Letter* **2008**, *8*, 2289-2292.

147. E.-O. Oh, C.-M. Whang, Y.-R. Lee, S.-Y. Park, D. H. Prasad, K. J. Yoon, J.-W. Son, J.-H. Lee and H.-W. Lee,“Extremely thin bilayer electrolyte for solid oxide fuel cells (SOFCs) fabricated by chemical solution deposition (CSD)” *Adv. Mater.* **2012**, *24*, 3373-3377.

148. M. Mamak, G. S. Métraux, S. Petrov, N. Coombs, G. A. Ozin and M. A. Green,“ Lanthanum strontium manganite/yttria-stabilized zirconia nanocomposites derived from a surfactant assisted Co-assembled mesoporous phase” *J. Am. Chem. Soc.* **2003**, *125*, 5161-5175.

149. E. Fabbri, L. Bi, D. Pergolesi and E. Traversa, “High-performance composite cathodes with tailored mixed conductivity for intermediate temperature solid oxide fuel cells using proton conducting electrolytes” *Energy Environ. Sci.* **2011**, *4*, 4984-4993.

150. S. P. Jiang, “Nanoscale and nano-structured electrodes of solid oxide fuel cells by infiltration: Advances and challenges” *Int. J. Hydrogen Energy* **2012**, *37*, 449-470.

151. H. P. Ding, Y. Y. Xie and X. J. Xue, “Electrochemical performance of $BaZr_{0.1}Ce_{0.7}Y_{0.1}Yb_{0.1}O_{3-\delta}$ electrolyte based proton-conducting SOFC solid oxide fuel cell with layered perovskite $PrBaCo_2O_{5+\delta}$ cathode” *J. Power Sources* **2011**, ***196***, 2602-2607.

152. M. Guillodo, P. Vernoux and J. Fourletier, “Electrochemical properties of Ni–YSZ cermet in solid oxide fuel cells: Effect of current collecting” *Solid State Ionics* **2000**, *127*, 99-107.

153. J. W. Kim, A. V. Virkar, K. Z. Fung, K. Mehta and S. C. Singhal, “Polarization effects in intermediate temperature, anode-supported solid oxide fuel cells” *J. Electrochem. Soc.* **1999**, *146*, 69-78.

154. J. X. Shi, X. J. Xue, “Optimization design of electrodes for anode-supported solid oxide fuel cells via genetic algorithm” *J. Electrochem. Soc.* **2011**, *158*, B143-B151.